


November 2017

# Design and Simulation of a Miniature Cylindrical Mirror Auger Electron Energy Analyzer with Secondary Electron Noise Suppression

Jay A. Bieber

University of South Florida, [bieber@usf.edu](mailto:bieber@usf.edu)

Follow this and additional works at: <https://scholarcommons.usf.edu/etd>

 Part of the [Electromagnetics and Photonics Commons](#), [Elementary Particles and Fields and String Theory Commons](#), and the [Nanoscience and Nanotechnology Commons](#)

## Scholar Commons Citation

Bieber, Jay A., "Design and Simulation of a Miniature Cylindrical Mirror Auger Electron Energy Analyzer with Secondary Electron Noise Suppression" (2017). *Graduate Theses and Dissertations*.  
<https://scholarcommons.usf.edu/etd/7393>

This Dissertation is brought to you for free and open access by the Graduate School at Scholar Commons. It has been accepted for inclusion in Graduate Theses and Dissertations by an authorized administrator of Scholar Commons. For more information, please contact [scholarcommons@usf.edu](mailto:scholarcommons@usf.edu).

Design and Simulation of a Miniature Cylindrical Mirror Auger Electron Energy Analyzer with  
Secondary Electron Noise Suppression

by

Jay A. Bieber

A dissertation submitted in partial fulfillment  
of the requirements for the degree of  
Doctor of Philosophy  
Department of Electrical Engineering  
College of Engineering  
University of South Florida

Major Professor: Wilfrido A. Moreno, Ph.D.  
Sanjukta Bhanja, Ph.D.  
Fernando Falquez, Ph.D.  
John Kuhn, Ph.D.  
Eduardo Rojas-Nastucci, Ph.D.  
Paris Wiley, Ph.D.

Date of Approval:  
November 15, 2017

Keywords: Finite Element Modeling, Scanning Auger Microscopy, Non-Destructive Evaluation, Electron Optics, Laser Beam Machining, Secondary Electron Emission

Copyright © 2017, Jay A. Bieber

## DEDICATION

To my parents, Arthur and Carol Bieber and family.

To my grandparents, Arthur and Hilda Martzolf Bieber, of Jamestown N.D.

To my Professor Wilfrido Moreno.

## ACKNOWLEDGMENTS

Above all, I appreciate my late father Arthur Jacob Bieber for choosing to get an education in electronics and cathode ray tube television repair from a small school in Wahpeton N. D. Without his education and schools like the North Dakota State College of Science in Wahpeton, I would have chosen a different path. My father was a big influence on me, and this work honors him directly since it is on the design of a specialized cathode ray tube in the form of an electron spectrometer, which is used for chemical analysis of thin films. I still have the old broken multimeter he gave me as a very young boy. My father was always there to help me, which allowed great success in all the amazing science projects I performed in elementary school and high school.

I would like to thank the College of Engineering at the University of South Florida and my major Professor Wilfrido Moreno for pushing me to continue my education. Dr. Moreno was extremely patient and provided continual encouragement as I completed this work while working full time at USF. I had the privilege to be educated in mathematics and numerical methods for electromagnetics from Professor Emeritus Dr. Arthur David Snider. His course in Numerical Techniques in Electromagnetics at USF introduced me to the power of mathematics, which was a gift of infinite value. I thank Dr. Snider for being a true teacher and for helping me to understand problems using Finite Element Modeling software. I also would like to thank Dr. James Leffew, Dr. Eduardo Rojas and Dr. Fernando Falquez for their valuable contributions.

I would also like to thank RBD Instruments Inc., in Bend Oregon. Specifically, the owner Randy Dellwo and his design engineer Ron Chase. These gentlemen spent many hours of valuable time teaching me the details of electron spectroscopy and the design of the microCMA electron spectrometer, which is

currently available as a commercial instrument from RBD. I do not know a person with more integrity than Randy who pays close attention to every detail. Randy has dedicated his life to keeping electrons flying in vacuum systems around the world, and I am honored to have been at the right place at the right time to help design the microCMA using FEM.

I would also like to thank Professor Steven A. Benson at the University of North Dakota, (UND), and President of Microbeam Technologies Inc. in Grand Forks N.D.. I attended Dr. Benson's graduate course in electron microscopy at UND using a JEOL JSM 35CF SEM. In 1993 Steve jump started my career when he made me responsible for a \$1.3 million dollar PHI 595 Auger-ESCA-SIMS system at UND while I was pursuing my undergraduate degree in Physics. It was exciting to be the one in charge of such an advanced instrument for several years and helping to solve real world problems related to coal fired power plants. Operating such an advanced scientific instrument turned out to be a lifelong experience. At the time, it felt like being the helmsman at the navigational controls of a starship with a crew tasked to solve real problems in energy production.

At the University of South Florida, (USF), Nanotechnology Research and Education Center, (NREC), I am grateful to the staff and the thousands of undergraduate and graduate student assistants who, over the years, have challenged me while taking my course in electron microscopy. Specifically, I am grateful to the student assistants who helped me with the daily operation of the laboratory. Their help provided me the time I needed to complete my Master. and Doctoral degrees while working full time at the NREC. Special thanks to the NREC staff, Robert Tufts, Richard Everly, Yusef Emirov, our office manager Sclafani Louis-Jeune, and my current assistants Richard Curtis, Kaylee Able, and Hung Bui.

Over the past Year Randy Dellwo from RBD helped me to secure a donation to NREC of a PHI 660 Scanning Auger Spectrometer, (SAM), with an attached Secondary Ion Mass Spectrometer, (SIMS), and a separate X-ray photoelectron spectrometer PHI LS-XPS which are now in operation at the NREC. Taking this donation was a challenge, to say the least, as the internal parts of both systems were ticking with

radioactive tritium from past, Department of Defense, (DOD), experiments. Robert Tufts and I managed to dodge the slow moving tritium 5.7 keV beta emission while scuttling the radioactive parts. My assistants helped with a complete rebuild of these systems, and in the process, they have become electron and ion beam “pilots” themselves.

The National Science Foundation, (NSF), played a big role in enabling this research. Three major research instruments were used in this research, which were acquired with funds awarded to USF. Specifically, the SU-70 SEM, the Quanta 200 3D FIB, and the nScript 3D printer were used in this work. Two electron spectrometer instruments were donated to USF from Constellation Technologies, Largo Florida, by Dr. David Schwartz.

Finally, I would like to thank the late John C. Moulder for being my first mentor. I had the honor of working with John to develop the scanning Pulsed Eddy Current, (PEC), system which John pioneered at the Center for Non-Destructive Evaluation, (CNDE), at Iowa State University. At the time, both John and I had a Bachelor of Science degree in Physics. As I write this acknowledgment, it is still vivid in my mind that John insisted that I continue my education and pursue a Doctoral degree; John, Thank You.

## TABLE OF CONTENTS

LIST OF TABLES .....	iii
LIST OF FIGURES.....	iv
ABSTRACT .....	vi
CHAPTER 1: INTRODUCTION .....	1
1.1. Motivation .....	1
1.2. Contributions .....	2
1.3. Dissertation Outline .....	3
CHAPTER 2: BACKGROUND AND LITERATURE REVIEW .....	5
2.1. Introduction.....	5
2.1.1. The Auger Process.....	6
2.1.2. The Cylindrical Mirror Electron Spectrometer .....	10
2.2. Comparison of AES with STEM and EDS .....	13
2.3. Comparison of Electron Sources .....	18
2.4. Electron Beam Induced Deposition of Field Emission Electron Source.....	21
2.5. EBID Mechanics.....	23
CHAPTER 3: FINITE ELEMENT MODELING OF THE CMA DESIGN .....	26
3.1. Introduction.....	26
3.2. Spectrometer Design and FEM Modeling Process.....	28
3.3. FEM Model of Electron Source with Einzel Lens.....	32
CHAPTER 4: SUPPRESSION OF SECONDARY ELECTRONS IN CMA .....	34
4.1. Introduction.....	34
4.2. Electron Spectrometer Background Noise .....	35
4.3. Secondary Electron Suppression .....	39
4.4. Electron Beam Deposition of Thin Films.....	40
4.4.1. Laser Beam Machining .....	41
4.5. Conclusion.....	47
CHAPTER 5: SEM MEASUREMENTS OF SE SUPPRESSION ON LBM OFHC FC ARRAY .....	48
5.1. Introduction.....	48
5.2. Scanning Electron Microscopy and SE Measurement on OFHC .....	49
5.2.1. Absorbed Current and Secondary Electron Detector .....	49
CHAPTER 6: CONCLUSIONS, FUTURE WORK AND FINAL INSPIRATION .....	53
6.1. Conclusions .....	53

6.2. Future Work.....	55
6.3. Final Inspiration.....	56
REFERENCES.....	57
APPENDIX A: COPYRIGHT PERMISSIONS.....	60
APPENDIX B: COMSOL SOLUTION HTML OUTPUT.....	72
B.1. Double Pass CMA.....	72
ABOUT THE AUTHOR.....	END PAGE



## LIST OF TABLES

Table 2-1: Comparison of different types of electron sources.....	20
Table 3-1: Constants and variables input into FEM for solution for double pass CMA .....	31
Table 4-1: Peak to background ratios measured from Auger spectra on Au and Cu.....	39
Table 4-2: SEM EDS quantitative elemental analysis area of LBM FC array .....	46

## LIST OF FIGURES

Figure 1-1: A vintage full size commercial electron spectroscopy system, [Authors photograph] .....	2
Figure 2-1: Photographs of Lise Meitner and Pierre Auger .....	6
Figure 2-2: Bohr model of the Auger process .....	6
Figure 2-3: X-ray fluorescence and Auger electron yield .....	7
Figure 2-4: Auger electron energy level diagram for silicon .....	8
Figure 2-5: Auger electron spectroscopy lines for the periodic table of elements .....	9
Figure 2-6: AES experiment with Cylindrical Mirror Analyzer, (CMA), and ion source .....	11
Figure 2-7: Electrons pass through the coaxial arrangement of an inner cylinder and outer cylinder in the CMA .....	11
Figure 2-8: Example Auger spectrum from completed spectrometer design.....	13
Figure 2-9: Electron beam sample interaction.....	14
Figure 2-10: Nanoscale sampling depth of Auger electrons .....	15
Figure 2-11: Particle defect from VLSI process showing typical auger spectra .....	16
Figure 2-12: Elemental Scanning Auger Microprobe, (SAM), image .....	17
Figure 2-13: EBID deposit array formation proposed for Field Emission Array, (FEA), electron source .....	22
Figure 2-14: A finely focused electron beam is used to decompose precursor gases adsorbed on the surface of a substrate in a vacuum system .....	23
Figure 3-1: COMSOL FEM solution for a parallel plate capacitor .....	27
Figure 3-2: COMSOL CAD FEM model for proposed double pass electron spectrometer .....	28
Figure 3-3: Photo comparison of outer cylinders from miniature and commercial CMA.....	29
Figure 3-4: COMSOL CAD FEM solution for proposed double pass electron spectrometer.....	32

Figure 3-5: COMSOL CAD FEM solution example of electron source with Einzel lens .....	33
Figure 3-6: FEM solution for electron source with Einzel lens .....	33
Figure 4-1: Detection limit of copper in a film one atom thick .....	35
Figure 4-2: Possible sources of secondary electron noise in the CMA [26] [27] .....	36
Figure 4-3: Complete normalized energy distribution of electrons emitted from a target .....	38
Figure 4-4: Energy distribution of electrons emitted from a target with Auger peaks .....	38
Figure 4-5: Mechanically machined saw-tooth grooves for SE suppression .....	39
Figure 4-6: Geometry of 270 degree electron beam deposition source.....	40
Figure 4-7: Nd:Vanadate, (Nd:YVO <sub>4</sub> ), Laser Beam Machining, (LBM), of Faraday Cup, (FC), array .....	42
Figure 4-8: Was ist das für ein dunkler fleck? (What is that dark patch?) .....	43
Figure 4-9: Nd:Vanadate, (Nd:YVO <sub>4</sub> ), laser machining of Faraday Cup array .....	44
Figure 4-10: SEM image of laser machined Faraday Cup array .....	45
Figure 4-11: SEM EDS spectrum and analysis area of LBM FC array .....	46
Figure 5-1: Sample holder with built in Faraday Cup for beam current measurements .....	49
Figure 5-2: Photo comparison of outer cylinders from miniature and commercial CMA.....	49
Figure 5-3: Secondary electron image and SE emission waveform overlay on laser milled OFHC.....	50
Figure 5-4: Secondary electron image and SE emission waveform overlay on laser milled OFHC.....	52
Figure 6-1: Commercial microCMA from RBD Instruments Inc.....	55

## ABSTRACT

In the nanoscale metrology industry, there is a need for low-cost instruments, which have the ability to probe the structure and elemental composition of thin films. This dissertation, describes the research performed to design and simulate a miniature Cylindrical Mirror Analyzer, (CMA), and Auger Electron Spectrometer, (AES). The CMA includes an integrated coaxial thermionic electron source. Electron optics simulations were performed using the Finite Element Method, (FEM), software COMSOL. To address the large Secondary Electron, (SE), noise, inherent in AES spectra, this research also included experiments to create structures in materials, which were intended to suppress SE background noise in the CMA. Laser Beam Machining, (LBM), of copper substrates was used to create copper pillars with very high surface areas, which were designed to suppress SE's. The LBM was performed with a Lumera SUPER RAPID-HE model Neodymium Vanadate laser. The laser has a peak output power of 30 megawatts, has a 5x lens and a spot size of 16  $\mu\text{m}$ . The laser wavelength is in the infrared at 1064 nm, a pulse width of 15 picoseconds, and pulse repetition rate up to 100 kHz. The spectrometer used in this research is intended for use when performing chemical analysis of the surface of bulk materials and thin films. It is applicable for metrology of thin films, as low as 0.4 nm in thickness, without the need to perform destructive sample thinning, which is required in Scanning Transmission Electron Microscopy, (STEM).

The spectrometer design is based on the well known and widely used coaxial cylinder capacitor design known as the Cylindrical Mirror Analyzer, (CMA). The coaxial tube arrangement of the CMA allows for placing an electron source, which is mounted in the center of the inner cylinder of the spectrometer. Simulation of the electron source with an Einzel Lens was also performed. In addition, experiments with thin film coatings and Laser Beam Machining to suppress Secondary Electron emission noise within the Auger electron spectrum were completed.

Design geometry for the miniature CMA were modeled using Computer Aided Design, (CAD). Fixed Boundary Conditions, (BC), were applied and the geometry was then meshed for FEM. The electrostatic potential was then solved using the Poisson equation at each point. Having found the solution to the electrostatic potentials, electron flight simulations were performed and compared with the analytical solution. From several commercially available FEM modeling packages, COMSOL Multiphysics was chosen as the research platform for modeling of the spectrometer design. The CMA in this design was reduced in size by a factor of 4 to 5. This enabled mounting the CMA on a 2 ¾ in flange compared to the commercial PHI model 660 CMA which mounts onto a 10 in flange. Results from the Scanning Electron Microscopy measurements of the Secondary Electron emission characteristics of the LBM electron suppressor will also be presented.

## CHAPTER 1: INTRODUCTION

### 1.1. Motivation

At the beginning of the 21<sup>st</sup> century, the field of Nanotechnology was coming of age. Almost all branches of science and engineering were being impacted by new nanostructured materials and Micro-electro-Mechanical devices, (MEMs). The semiconductor industry had also entered the nanoscale realm. As of 2017, commercial devices are now being manufactured with microprocessor feature sizes as low as 10 nanometers, (nm). The drive continues in industry to develop technology, which will enable fabrication of smaller and more compact devices. Along with this trend come great challenges and opportunities to develop metrology methods, which will enable device miniaturization to continue. Two widely used tools in semiconductor metrology are Scanning Transmission Electron Microscopy, (STEM), and Auger Electron Spectroscopy, (AES). STEM and AES are two of the few methods, which have resolution capability to probe the composition and the chemical environment of structures, both laterally and in depth, below 30 nm [1].

Surface analysis by electron spectroscopy has become increasingly important as a materials characterization instrument for devices based on thin film processes. As the trend to decrease feature size continues, challenges arise due to limitations of metrology instruments. The thin films found in common consumer devices such as cell phones, LCD displays, computer memory, and hard disks must be tested for quality control. Figure 1-1 shows a full size electron spectroscopy system. The vacuum system and spectrometer are shown on the left and the controls console on the right. Due to the cost and large footprint of conventional commercial surface analysis instruments, several instrument manufacturers have sought to produce a commercially viable miniaturized spectrometer, which can be used standalone, or as an attachment to an existing vacuum chamber for thin film metrology.

Following the trend for making devices smaller and less expensive, it is intended in this dissertation to model and develop an optimized design for a miniature electron spectrometer. The spectrometer in this study is intended to be used to perform chemical analysis of the surface of bulk materials, nanometer thick thin films, and nanostructures by AES. However, the spectrometer can also be used for general purposes in any application that requires collection and analysis of the kinetic energy of electrons, such as X-ray Photoelectron Spectroscopy, (XPS). A review of electron spectroscopy and Auger spectroscopy, in particular, will follow as well as a review of the interaction of electrons with matter. In addition, a review of electron optics associated with the formation of electron beams and the effect of a partial vacuum in electron beam microscopy will be presented.



*Figure 1-1: A vintage full size commercial electron spectroscopy system, [Authors photograph].*

## **1.2. Contributions**

The contributions of this research are summarized below:

- a) Development of an integrated innovative research platform for design and simulation of electron optical components using Computer Aided Design, (CAD), and Finite Element Method, (FEM) analysis. The CAD FEM software packages were used in this research to

- specifically solve for the electrostatic fields inside a double pass CMA with a coaxial mounted thermionic electron source, which is used as a source to excite electrons in the AES.
- b) Innovative processes designed to allow for the fabrication of nano-structures and micro-structures using Electron Beam Lithography, (EBL), Electron Beam Induced Deposition, (EBID), Focused Ion Beam, (FIB), Electron Beam Physical Vapor Deposition, (EBPVD), and Laser Beam Machining, (LBM).
  - c) Modified a method used by M. Postek at NIST to measure SE emission using a defocused beam of electrons to simulate diffusion of electrons inside the CMA. Using a defocused beam reduces the possible beam damage to the LBM structure. It also reduces SE noise in the waveform from imperfections in the substrate such as scratches. In addition, the modified method acts to homogenize the measurements from anisotropy in the substrate.
  - d) The novel CMA design using COMSOL FEM was successfully implemented and validated in a commercial miniaturized Auger Electron Spectroscopy system [2].
  - e) A novel LBM structure was invented, which acts to amplify, or to suppress emission of electrons, which may also act to absorb EM radiation. SE emission may be tuned by modification of the LBM structures to obtain electron emission amplification or suppression [3].

### 1.3. Dissertation Outline

This dissertation contains six chapters, including the current chapter, which covers the Introduction. The remaining five chapters are outlined below.

- a) Chapter 2 includes a literature review on the general theory of Auger spectroscopy and on the CMA design including the different types of electron sources, which are used. In addition, it includes an example of the design efforts associated with the fabrication of an electron source for the CMA.



- b) Chapter 3 describes the finite element modeling using COMSOL for the design and geometry refinement of the CMA, and a thermionic electron source, with Einzel lens, using COMSOL's particle tracking module.
- c) Chapter 4 describes the secondary electron noise sources in the CMA, and the respective suppression mechanisms. A process to fabricate SE suppression Faraday Cup, (FC), arrays by Laser Beam Machining is also presented.
- d) Chapter 5 contains the procedure used to measure the relative secondary electron emission, and the absorbed current in the SE electron substrates fabricated by Laser Beam Machining, (LBM). It also includes the development of a technique for measuring secondary electron emission using the video output level of the secondary electron detector in an SEM.
- e) Chapter 6 presents the conclusion and a summary of the dissertation, highlights the research contributions, and offer recommendations for future research.

## CHAPTER 2: BACKGROUND AND LITERATURE REVIEW

### 2.1. Introduction

In 1922, Physicist Lise Meitner, Figure 2-1 (a), discovered a unique type of electron with a 'signature energy' that is sometimes emitted from an ionized atom. Meitner found that atoms with at least three electrons after being ionized sometimes became doubly ionized, by spontaneously emitting a second electron of a specific energy in what is now known as the Auger electron. It is pronounced phonetically similar to the "O-shjey effect" and as such should not to be confused with the helical mechanical tool with the same spelling, the auger. The Auger process is shown in Figure 2-2.

The discovery was made and reported by Meitner in 1923 in the journal *Zeitschrift für Physik*, two years before Pierre Auger, pictured in Figure 2-1 (b), discovered the effect. The English speaking scientific community came to attach Auger's name to it, likely due to the fact that it was directly related to the main topic of his Ph.D. research [4]. Until the early 1950s Auger transitions were considered nuisance effects by spectroscopists, not containing much relevant new material information, but studied so as to explain anomalies in x-ray spectroscopy data. Since 1953, Auger transitions started to be used as practical techniques for surface analysis, and it is now a commonly used analytical technique in materials science. Auger electrons are essentially photo-electrons generated in an atom by internal absorption of a florescent x-ray, and are emitted at discrete energies for each element in the periodic table, which provides identification of their respective atom of origin. The first step in the Auger process is the ionization of an atom to create a vacancy. The initial vacancy can be produced by any form of ionizing radiation with an energy larger than the binding energy, which holds the electrons in the atom. In this research, a primary beam of thermionic emitted electrons were used as the ionization source. The source typically has an

adjustable energy of 3 to 10 keV, and adjustable beam current. Electron source types are summarized in Table 2-1.

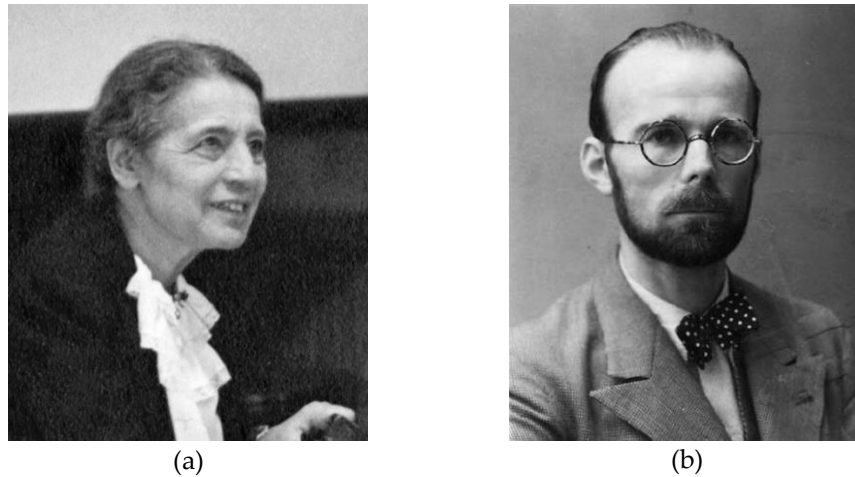


Figure 2-1: Photographs of Lise Meitner and Pierre Auger. (a) Lise Meitner, (b) Pierre Auger Comparative contributions to the Auger effect [4].

### 2.1.1. The Auger Process

As depicted in Figure 2-2, an electron from the L shell with binding energy  $E_L$ , may then drop to fill the vacancy left by the initial ionization. During this transition, an x ray is emitted with energy equal to the difference in energy,  $(E_K - E_L)$ , between the K and the L shells.

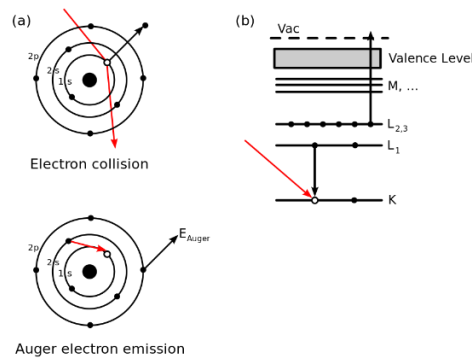


Figure 2-2: Bohr model of the Auger process.

(a). An incident electron from a focused beam creates a core hole in the 1s level. An electron from the 2s level fills in the 1s hole and the transition energy is imparted to a 2p electron, which is emitted as an Auger electron with energy equal to the difference in binding energy between the 1s and 2p levels. (b) In spectroscopic notation it is the K-L energy difference yielding a KLL Auger electron, representing the 3 electrons involved. The final atomic state has two holes, one in the 2s orbital and the other in the 2p orbital, [Public Domain] [5].

As seen in Figure 2-3, in elements of low atomic number, X-rays have high probability of greater than 50% chance of being absorbed by another electron as it exits the atom in what is known as a radiation-less transition. If the x ray has enough energy it will be absorbed, and knock this electron out of the atom. This electron will then carry away the excess energy it absorbs from the x-ray to become what is referred to as a KLL Auger electron with kinetic energy  $E_a$ . KLL is the notation used, which indicates initial ionization in the K shell, followed by the radiation-less transition from the L shell, a coincident Auger emission from the L shell.

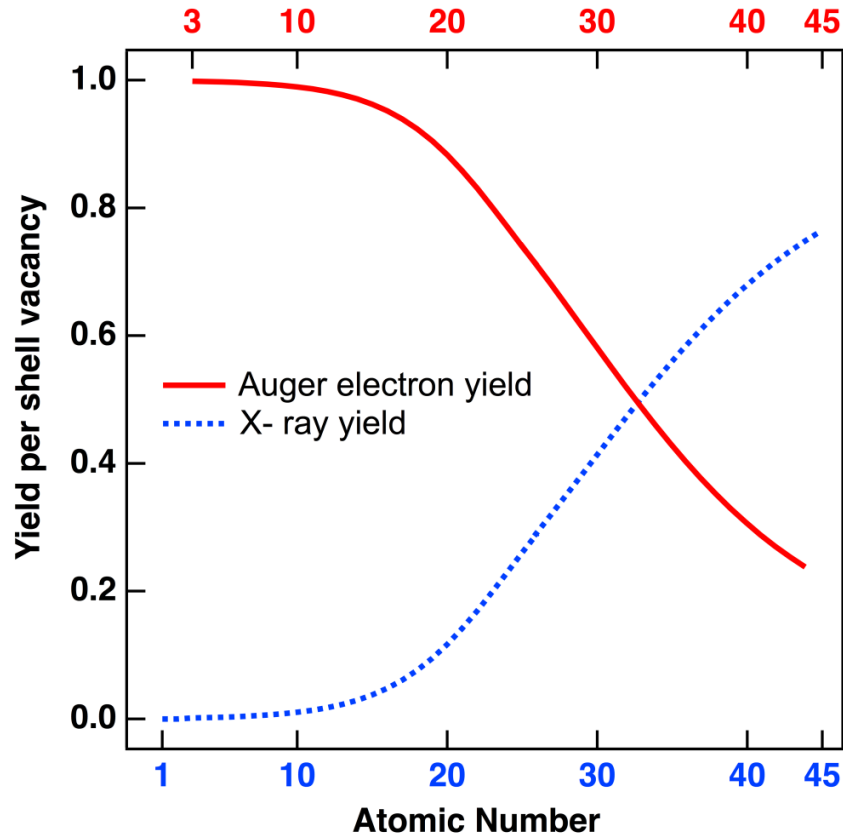


Figure 2-3: X-ray fluorescence and Auger electron yield. Yield is plotted as a function of atomic number for K shell vacancies. Auger transitions, (red curve), are more probable for lighter elements, while X-ray yield, (dotted blue curve), becomes dominant at higher atomic numbers. Similar plots can be obtained for L and M shell transitions. Coster – Kronig, (i.e. intra-shell), transitions are ignored in this analysis [6].

Figure 2-4 is a schematic of the electron energy levels for the element silicon, which contains 2, 8, and 4 electrons, respectively in the K, L, and M shells. Auger transitions are notated with subscripts to differentiate transitions, which originate from the sub shells, as it is shown for the two different LMM transitions in silicon. The initial ionization occurs in sub shell L3 of the L shell in both cases, but the radiation-less transition occurs in a different M sub-shell in each case as indicated by the subscripts. The innermost electron or K shell in a silicon atom is bound to the nucleus with energy  $E_k$ .

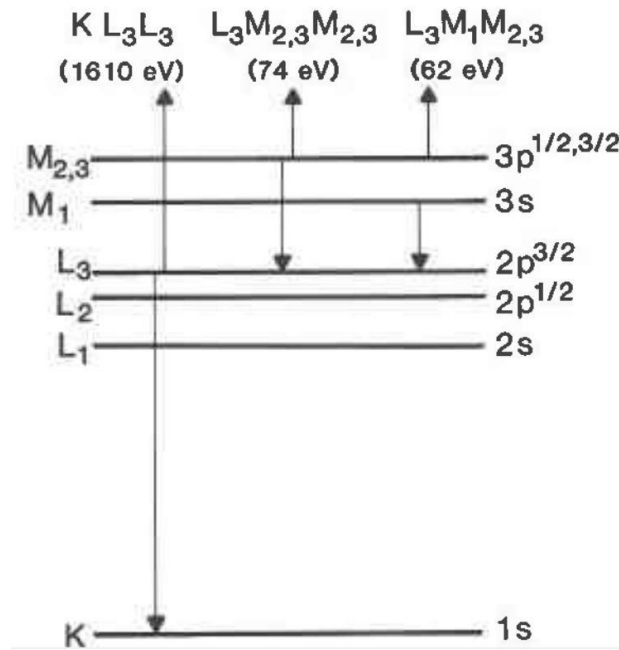


Figure 2-4: Auger electron energy level diagram for silicon  
The three most intense Auger spectral lines are shown. One KLL, and two different LMM Auger transitions are shown. The energies shown are from a quartz specimen [7].

To generate the Auger electron, the X-ray energy,  $E_k - E_L$ , must be greater than  $E_o$ , where  $E_o$  is the binding energy of the electron to which it couples. The energy of the Auger electron is;

$$E_a = (E_k - E_L) - E_o' \quad (2.1)$$

the  $E_o'$  is the energy, which takes into account the slight change in the unionized electron binding energy. Energy,  $E_o$ , occurs when the atom is ionized. Figure 2-5 shows the range of the Auger spectral peak energy typically used for detection of elements in the periodic table from lithium to uranium.

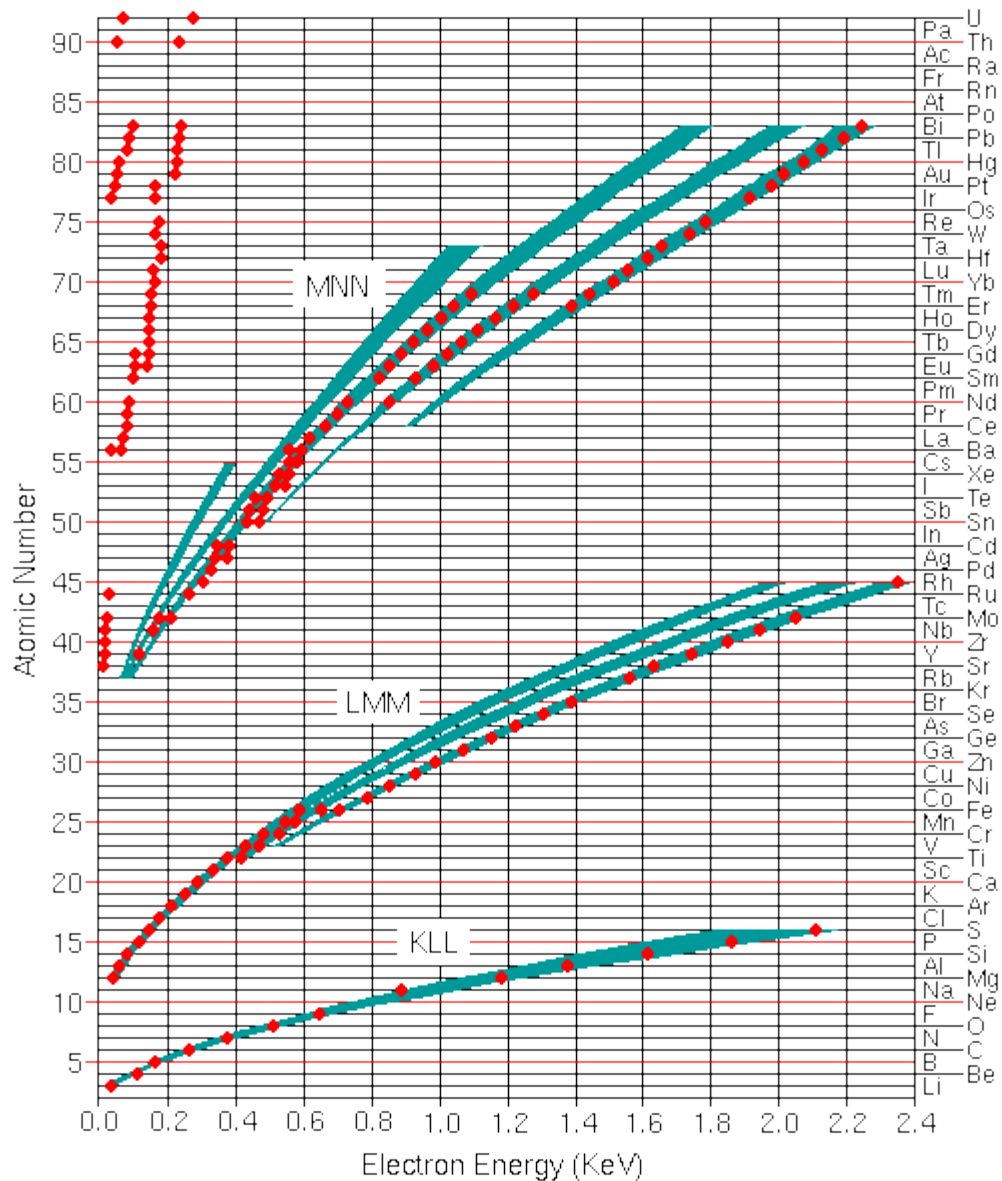


Figure 2-5: Auger electron spectroscopy lines for the periodic table of elements.

Qualitative analysis by Auger electron spectroscopy depends on identification of the elements responsible for the various peaks in the spectrum. The Auger electron energies are widely tabulated for all elements in the periodic table. The figure shows the most useful Auger peaks in the KLL, LMM, and MNN parts of the spectrum as well as higher transitions for elements above cesium. The red dots indicate the strongest and most characteristic peaks and the green bands indicate the rough structure of less intense peaks [8].

The electrons emitted, which are characteristic of the Auger process, are able to escape from only a very thin depth of the specimen surface. Due to their low energy, the mean free path of Auger electrons is only a few nanometers. Therefore, they escape with their signature energy from the first few atomic

layers of the sample surface. The escape depth does not increase with the primary electron probe energy as it does in energy dispersive x-ray micro-analysis, (EDS). The escape depth of the Auger electrons depends only on the specific energy level of the atom from which it was emitted. This physically limits AES sampling depth as low as the sub-nanometer range.

### 2.1.2. The Cylindrical Mirror Electron Spectrometer

The Cylindrical Mirror Analyzer, (CMA), is the most commonly used spectrometer for commercial AES systems. The CMA is the essential physics component, and it consists of a cylindrical capacitor made of two concentric metal cylinders. A schematic of a typical AES CMA instrument is shown in Figure 2-6. An electron gun mounted on the inner cylinder directs a focused primary electron beam onto the sample to be analyzed. A separate gas ion source, such as  $+Ar$ , is also used to mill the sample surface to clean contamination and determine the elemental composition as a function of depth. The inner cylinder is held at ground potential while a power supply ramps the voltage on the outer cylinder to allow tuning of the spectrometer. The spectrometer is designed to allow electrons to pass in the annulus between the tubes where they are subjected to an electric field and then pass through a series of apertures, which sorts them according to their velocity. With the outer cylinder held at a specific voltage the electrons are forced to follow a curved parabolic trajectory. Only electrons within a narrow energy range are allowed to pass. Electrons outside this range are either too slow or too fast and are physically blocked by circular apertures in the inner cylinder.

Figure 2-7 shows a more detailed schematic of the CMA with the outer cylinder fixed at -2000 volts. At this voltage only Auger electrons of a fixed energy which obey the equation of motion in an electrostatic field will travel the correct parabolic path and be counted by the detector. The CMA is a band pass filter and the electron throughput increases with the aperture size. As with other types of spectroscopy, narrow pass energy gives the best spectral resolution. However, the sensitivity is less due to a smaller throughput resulting in few electrons reaching the detector. To allow for the Electron Multiplier, (EM), and end caps

to be attached, the inner cylinder is usually extended, and circular slots are cut into it in order to allow for electrons to pass through the spectrometer, as shown in Figure 2-7.

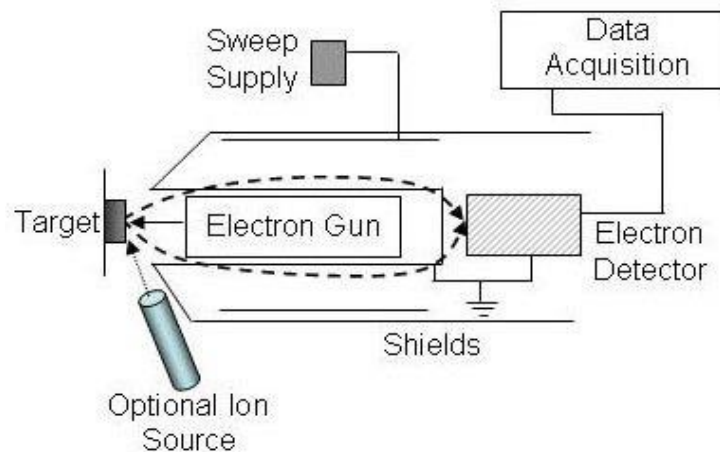


Figure 2-6: AES experiment with Cylindrical Mirror Analyzer, (CMA), and ion source.

An electron mounted inside the inner cylinder is focused onto a specimen and emitted electrons are deflected around the electron gun and pass through an aperture towards the back of the CMA. These electrons are then directed into an electron multiplier detector, (EM), for analysis. With the inner cylinder at ground potential, the sweep supply ramps a voltage on the outer cylinder to allow tuning the spectrometer. An optional ion gun can be integrated for depth profiling experiments [9].

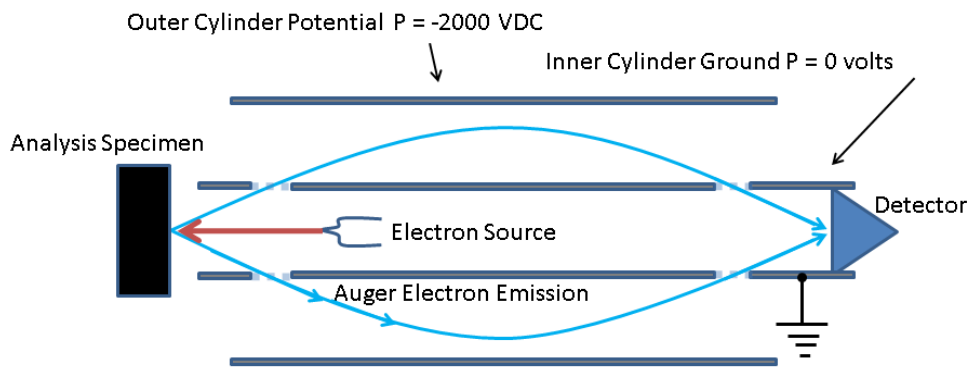


Figure 2-7: Electrons pass through the coaxial arrangement of an inner cylinder and outer cylinder in the CMA. As illustrated, a beam of primary electrons originating from the electron source are focused on the specimen to be analyzed. Auger electrons emanating from the specimen pass through an electron transparent mesh on the inner cylinder on their way to an encounter with the negative electric potential of -2000 volts, on the outer cylinder. In 3D the electrons form a football shape, or oblate spheroid, as they pass left to right through the spectrometer and land on the electron multiplier detector on the right.



A good review of the history of the development of the electron spectrometer is given by Roy and Trembley [10]. The CMA geometry offers the advantage of allowing many electrons to be processed simultaneously through the annular space formed between the inner and the outer cylinders. Electrons emitted from a point source located at a Working Distance, (WD), away from the entrance of the spectrometer will enter this annular space at some velocity. As in the case of a parallel plate device, the electrons are repelled by a negative potential on the outer cylinder. The electrons travel through the spectrometer in the shape of an oblate spheroid shell, which is like an American football skin, and they come to focus at a point, again at the same distance WD, after emerging from the opposite end of the CMA. Only electrons of a specific velocity will make it through the potential gradient and arrive at the point WD along the axis of the spectrometer. The voltage on the outer cylinder is swept in order to allow for a range of electron velocities to pass through the spectrometer and be counted by the detector. Figure 2-8 shows typical Auger spectra taken on the microCMA currently being manufactured at RBD Instruments Inc. in Bend Oregon. Shown in (a) and (b) are plots of raw Auger data on pure Cu and Ag respectively, which show the elemental peaks on top of a large background signal. As the voltage on the outer cylinder sweeps, the electrons arriving at the detector are counted and plotted on the vertical axis. The horizontal axis shows the kinetic energy in electron volts, eV. Each element detected may have several peaks in the spectrum as presented in these plots. This data is smoothed and differentiated using a Savitzky–Golay digital smoothing filter and differentiation algorithms [11]. Figure 2-8 (c) and (d) show the Cu and Ag spectra respectively, after the raw data has been smoothed and differentiated. The resultant peak to peak magnitudes are then used to quantify the elements present in the sample, by comparison with the magnitude of peaks on pure elements under the same experimental conditions.

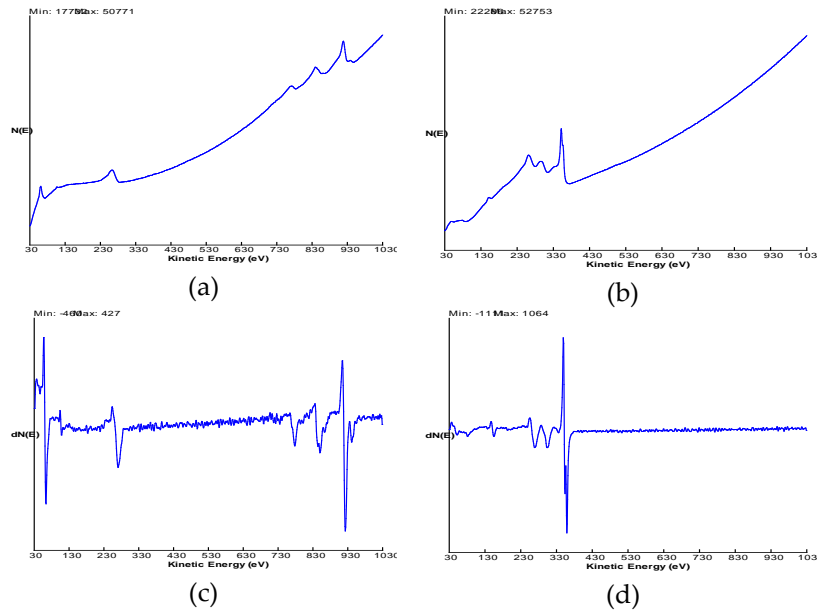


Figure 2-8: Example Auger spectrum from completed spectrometer design.

Shown in (a) is a plot of the raw Auger spectrum data for copper as collected from the RBD Instruments Inc. microCMA spectrometer on a pure copper sample. (c) shows the raw data differentiated to obtain the peak to peak height of the Cu peak. The plot in (b) shows the raw spectrum data for silver, which is again differentiated as shown in (d). The primary electron beam energy was set at 3 KeV with beam current of 300 nA. [2] [11].

## 2.2. Comparison of AES with STEM and EDS

Figure 2-9 shows a beam of primary electrons converging on the sample along with the relative escape depth of the various types of radiation, which are commonly collected to perform elemental analysis. As shown in more detail in Figure 2-10, the self-limiting size of the Auger analysis volume allows for elemental composition to be determined without interference from the substrate material. The Auger escape range varied from about 0.4 to 5 nm across the periodic table. An Auger electron generated greater than 5 nm below the surface will lose its discrete energy due to inelastic collisions, and so its atom of origin cannot be detected. Instead it will become part of the large background of secondary electron noise, which is concomitant in the process. The electrons emitted from the sample, both Auger and secondary, are counted and energy analyzed by the electron spectrometer. The most common electron spectrometer separates the electrons by their kinetic energy in an electrostatic field. Using an electron multiplier, the number of electrons emitted at each kinetic energy is typically binned in increments of 0.05 to 1.0 eV. The

data is converted from analog to digital and the resultant spectrum is displayed as a plot of the number of electrons vs. energy.

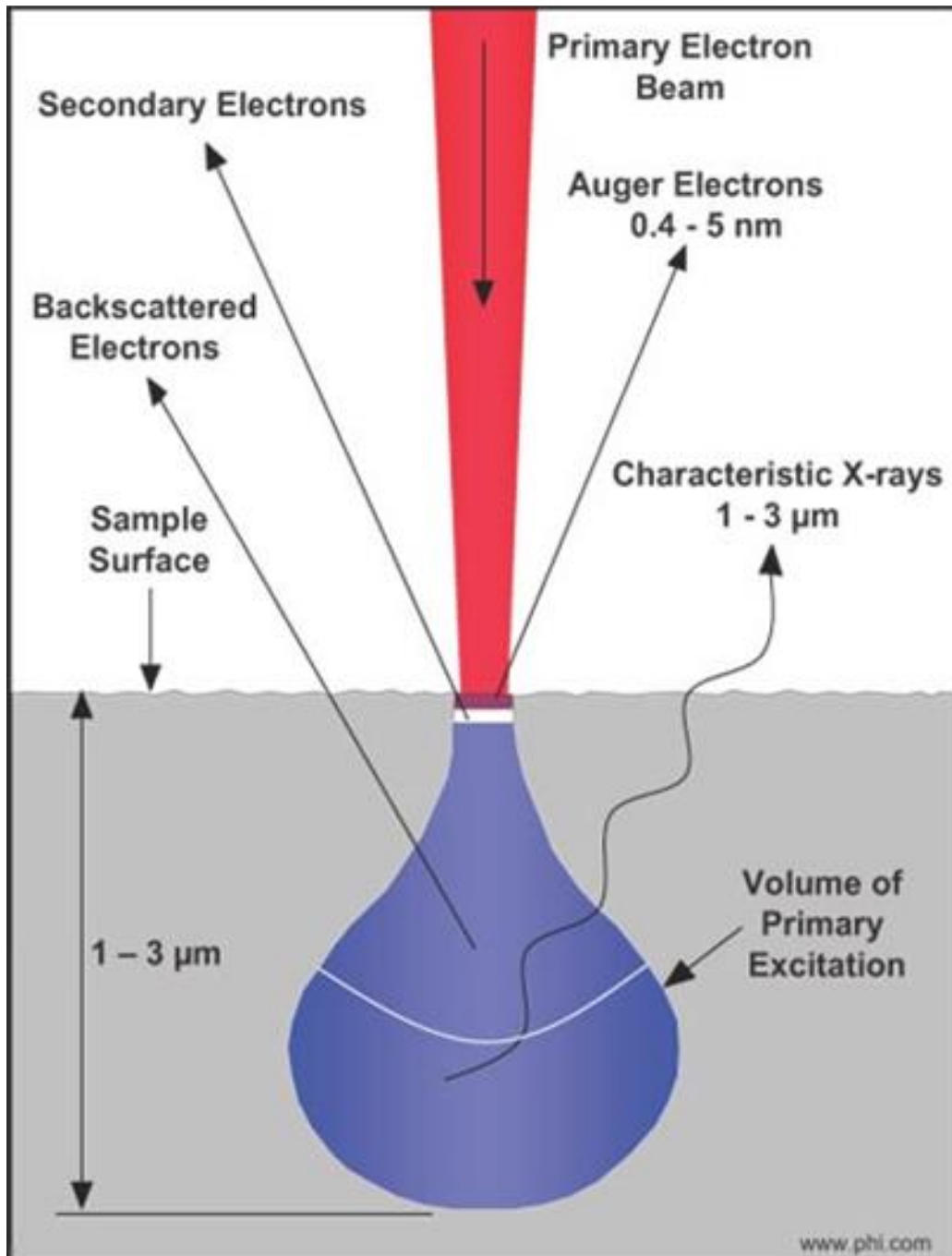


Figure 2-9: Electron beam sample interaction.

This drawing shows the relative escape depth of characteristic x-rays, and several types of electrons. In energy dispersive x-ray micro-analysis EDS, the escape depth is 1-3 microns and increases with beam energy. Auger escape is independent of beam energy, and only depends on its atom of origin, i.e. its energy [12].

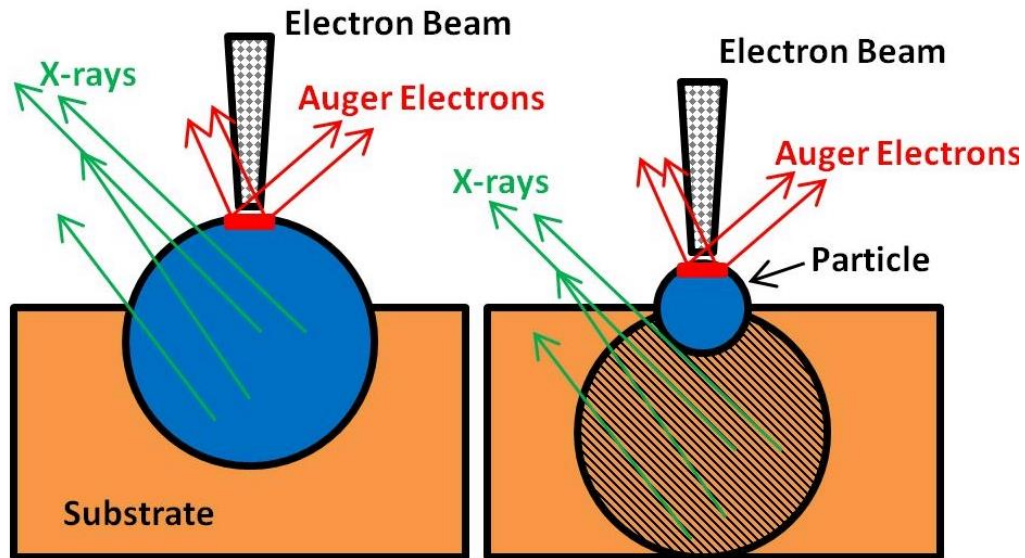


Figure 2-10: Nanoscale sampling depth of Auger electrons.

Auger electrons enable analysis of either particle above including a nanoscale, ( $<0.1$  micron), particle with no interference from the substrate as illustrated on the right. Auger electrons leave only from the particle and not the substrate. X-ray EDS can only be done on larger, ( $>0.1$  micron particles), here on the left, without substrate interference Adapted from [13].

The Auger effect has profound implications in that it is one of only a few techniques, which can perform defect analysis at the scale necessary for modern VLSI circuits and other nanoscale devices. Figure 2-11 shows typical differentiated Auger spectrum from analysis of a particle defect in a VLSI process. Because the Auger signal is very small with a large secondary electron background, the spectrum is usually differentiated to enhance peak detection. Here, a secondary electron SEM image of a large 500 nm defect that was detected on a wafer in a tungsten, (W), etch process is presented. The W etch uses a Sulfur Hexafluoride, ( $\text{SF}_6$ ), plasma to remove the W, which is deposited on the wafer on top of a titanium nitride, (TiN), adhesion layer [14]. The differentiated Auger spectra, red and green, reveal that the particle is a composite of aluminum and titanium. The point analysis spectra taken on different spots on the particle in Figure 2-11 indicate the particle may be composed of physically segregated areas of Al and Ti. An Auger electron map was then performed, which illuminates the elemental distribution on the particle. In Figure

2-12, the top image, the same particle again imaged with standard secondary electron (SE) detector can be seen. The bottom image shows the same particle imaged using the Auger spectrometer as the electron detector. The electron beam is scanned over the sample just as in the SE image, but the spectrometer is set to only allow for Al or Ti Auger electrons to pass. Two separate images were scanned, one set for Al (green), and the second set for Ti (red). The Auger peaks were then superimposed to produce the composite shown. The brighter green and red, show where the larger Al and Ti Auger peaks appear, thus showing a map of the elemental concentrations. It was concluded from the Auger elemental map that the aluminum particle originated from the interaction between an etch by-product of the TiN adhesion layer and the aluminum vacuum deposition chamber.

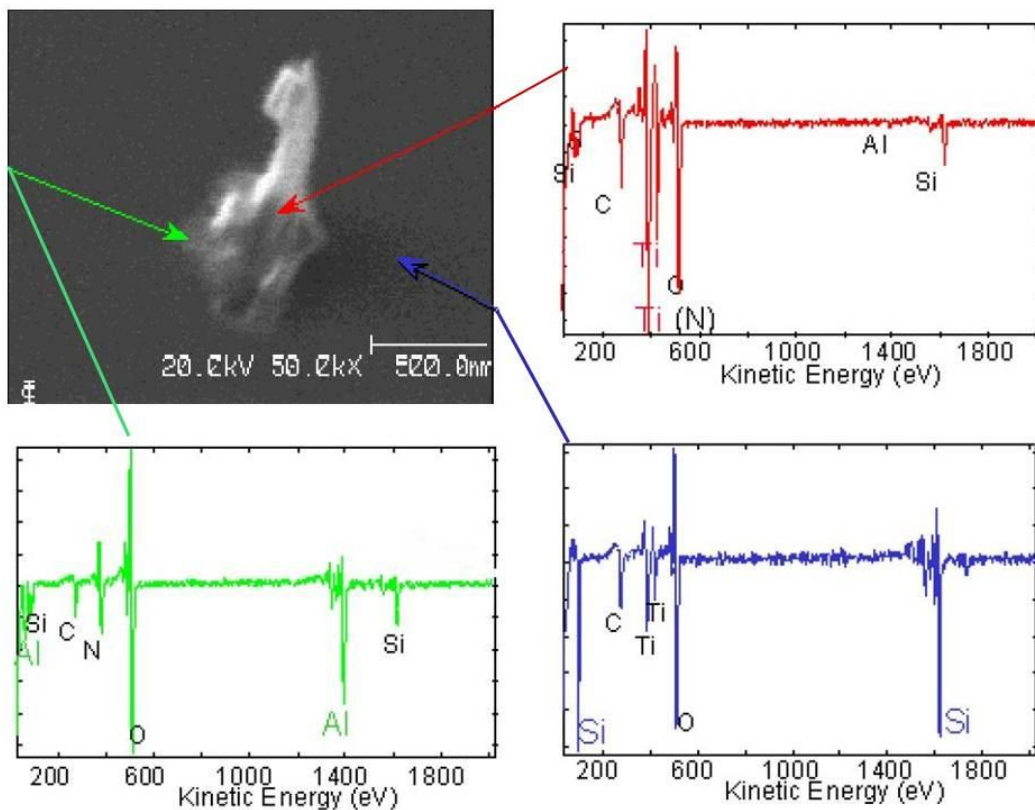


Figure 2-11: Particle defect from VLSI process showing typical Auger spectra. Spot analysis was performed at 3 different points on a nanoscale defect in a VLSI tungsten etch process. This is a good demonstration of the ability of Auger spectroscopy with SEM to perform nanoscale analysis without interference from adjacent structures [14].

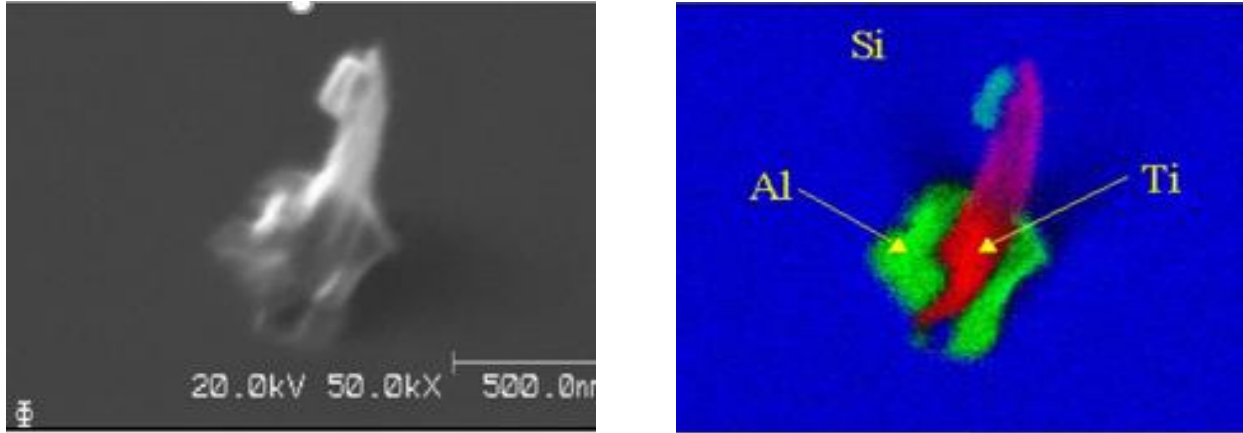


Figure 2-12: Elemental Scanning Auger Microprobe, (SAM), image.

The left image is a Scanning Electron Microscopy, (SEM), image showing a nanoscale defect with a 500 nm scale bar. The right image shows the scanning auger electron elemental map performed on the same defect. Shown is the distribution of Al and Ti demonstrating the high spatial resolution of Auger spectroscopy [14].

This is a striking example of the ability of Auger spectroscopy to perform Non-Destructive Evaluation, (NDE), analysis on particles with very small analytical volume, and separate the elemental composition. This level of detail is not possible using other analysis techniques such as EDS or STEM where destructive analysis of the sample is required.

Before Thomsons discovery of the electron, and since the development of the cathode ray vacuum tubes, improvements in vacuum technology have been the key to unlocking the secrets hidden within matter. Experiments with electrons under high vacuum are beginning to reveal their true nature, and have lead us to the current understanding of the quantum nature of matter. The cathode ray tube remained the basis for the display of video on consumer electronics until the recent development of thin film based flat panel displays. While cathode ray vacuum tubes are no longer used as main stream displays, they are still widely used in the form of SEM instruments capable of probing the structure of matter down to the atomic scale. Early on in the use of the SEM and other scanning beam instruments such as the Scanning Auger Microscope, (SAM), it was noticed that the electron beam deposits contamination on any surface it contacts, which is the residual of gas in the vacuum system in the form of Volatile Organic Compound, (VOC), which

are ubiquitous in nature. In fact before taking data, the “adventitious hydrocarbons” were actually used to calibrate the spectrometer, which was then referred to as an ESCA or electron spectroscopy for chemical analysis, [15].

STEM, AES and SAM are expensive to purchase and maintain. However, they are members of the few methods, which elemental composition at the nanoscale without interference from surrounding structures can be probed. With STEM, the specimen must be mechanically cross sectioned and thinned to about 50 nm to allow for the electron probe to pass through it attenuated, but not absorbed. STEM sample preparation can be a very laborious process, and can sometimes introduce defects, which can then hinder the analysis. However, AES requires no sample preparation. The less the specimen is altered by handling, the better it is for AES. AES analysis can be performed on bulk unaltered materials, and no mechanical thinning is required to get small sampling volumes of a few cubic nanometers.

### 2.3. Comparison of Electron Sources

Part of the design process in any charged particle optical system starts with choosing a suitable particle source. The diameter of the beam can vary over a wide range, which is usually between 1 nm and 100 microns, and depends on the type of electron source and the design requirements of the system. The size of the area from which the electrons are emitted is referred to as source size. The source size and physical constraints, such as the available length of the electron beam travel, play a role in the final beam spot size on the sample. As seen in Section 2-2, the beam spot diameter along with the escape depth of Auger electrons forms the volume of the analysis disk on a flat sample.

The standard thermionic electron source uses Joule heating of a V shaped tungsten wire 5-100  $\mu\text{m}$  in radius heated to  $\sim 2500$  to  $3000$  K. Lanthanum hexaboride, ( $\text{LaB}_6$ ), is desirable due to its long life and high brightness. It is typically a rod of sintered powder about 1 mm in diameter with a tip machined to a few microns in radius. It has a very low work function and its high brightness is obtained by operating it at a temperature of  $\sim 1900\text{K}$ . However, it requires a vacuum of  $10^{-8}$  Torr, which is usually achieved by the

addition of an ion pump to the SEM system. The emission current density,  $J_c$ , delivered by thermionic sources depends on the temperature,  $T$ , and is expressed by the Richardson law;

$$J_c = A_c T^2 \exp(-E_w/kT) \text{ A/cm}^2 \quad (2.2)$$

where  $A_c$  is a constant of the material, which is referred to as the Richardson constant, and  $E_w$  is the work function. Higher temperatures deliver greater beam current, but the tradeoff is an exponentially decreasing lifetime due to thermal evaporation of the cathode material.

Field emission sources typically consist of a tungsten rod sharpened to a point, which is typically 5-100 nm in radius. The sharp tip helps provide the very high electric fields needed to pull electrons out of the metal. Single crystal tungsten is typically used because it is a mechanically strong material. In order to get the desired brightness in electron current, the electron extraction potential is held as high as possible. In fact, the fields are held so high that the tungsten tip is at the threshold of self-destruction due to mechanical stress, which is induced by the electric field. The emission current density,  $J_c$ , delivered by Field Emission, (FE), depends on the electric field,  $E$ , and follows the Fowler-Nordheim equation [16];

$$J_c = BE^2 \exp(-6.8 \times 10^7 \phi^{3/2}/E) \quad (2.3)$$

where  $B$  is a field-independent constant of dimensions ( $A/V^2$ ) and  $E$  is the applied field ( $V/cm$ ). Cold field emission sources have become the source of choice in electron microscopes to achieve the highest resolution. However, they have seen little use in Auger spectrometers due to their instability in output, which becomes an issue when quantitative elemental analysis is needed. The instability is caused by atoms that are adsorbed onto the surface of the tip [17]. This changes the work function, which results in large changes in the emission current. To minimize the current fluctuations, the electron source must be operated with ion pumps in an extreme Ultra High Vacuum, (UHV), environment,  $10^{-10}$  Torr, or better, which comes with a significant increase in cost.

The latest development in electron sources is the thermal field emission source. It is now the most commonly available in many commercial Auger spectroscopy systems and electron microscopes. This



source combines the tungsten tip of the field emission source and the heating of the thermal source. The tip is operated at a temperature of  $\sim 1000$  to  $1800$  K, which makes it less sensitive to gas adsorption. Although the "Schottky source" or Field Emission Gun, (FEG), are commonly used names, it is more properly called a "thermionic assisted field emitter" since the electrons escape over the work function barrier by both thermal excitation and field emission. Its brightness is almost as high as a cold field emission source, with a slightly larger tip size of  $20$  nm and an intermediate energy spread. The tungsten is usually coated with zirconium oxide to reduce the work function. It requires a vacuum in the range of  $10^{-9}$  Torr, which means a more expensive pump than is required for a thermal emitter source.

In the early stages of this research, it was proposed to use nanofabrication techniques to fabricate a field emission source. Several attempts were made to fabricate this source from an array of needles each of which would act as an electron source to average out the current emission instability of cold field emission electron sources. This process is presented in section 2.4 on Electron Beam Induced Deposition, (EBID). After several unsuccessful attempts, this work was abandoned in order to use a more conventional tungsten thermionic electron source. Thus a thermionic electron emission source was finally chosen for the CMA design and simulations. Table 2-1 shows a comparison of the most commonly used electron sources used in an AES CMA [18].

Table 2-1: Comparison of different types of electron sources. Adapted from [18]

Source type	Temp.(K)	Brightness (A/cm <sup>2</sup> /sr)	Source size (nm)	Energy spread (eV)	Vacuum requirement (Torr)	Work function(eV)
Tungsten thermionic	2700	$\sim 10^5$	25000	2-3	$10^{-6}$	4.5
LaB <sub>6</sub>	1900	$\sim 10^6$	10000	2-3	$10^{-8}$	2.4

Table 2-1 (Continued)

Source type	Temp.(K)	Brightness (A/cm <sup>2</sup> /sr)	Source size (nm)	Energy spread (eV)	Vacuum requirement (Torr)	Work function(eV)
Thermal (Schottky) ZrO field emitter	1800	~10 <sup>8</sup>	20	0.9	10 <sup>-9</sup>	2.7
Tungsten field emitter	273	~10 <sup>9</sup>	5	0.22	10 <sup>-10</sup>	4.5

#### 2.4. Electron Beam Induced Deposition of Field Emission Electron Source

With current technologies it is possible to fabricate devices that have at least one dimension in the nanometer range. When the dimension of these nanostructures approaches the De Broglie wavelength, new properties emerge due to quantum mechanical effects that can be the basis for the development of a new generation of devices and materials [19]. These nanoscale devices can be made with zero, one, or two dimensions, and are known as quantum dots, wires, and wells respectively. One emerging technique to create nanostructures is to use a highly focused beam of electrons as an energy source to deposit materials in a process similar to Chemical Vapor Deposition, (CVD). This technique has become to be known as Electron Beam Induced Deposition, (EBID). EBID was used to attempt to fabricate a field emission array electron source for the CMA analyzer.

Since the earliest use of the electron microscope, the electron beam has been observed to deposit contamination on areas where it irradiated the specimen. As with Auger electrons spectroscopy, it was long thought to be a nuisance, and is still a serious problem when it affects high resolution imaging, and or analysis using Energy Dispersive Spectroscopy, (EDS), or Auger Electron Spectroscopy, (AES). It is assumed that this contamination is due to the interaction of the electron beam with hydrocarbon

contamination present in the vacuum system. The introduction of Ultra High Vacuum, (UHV), systems significantly reduced these problems, but the carbon was still present. The vast reduction in impingement rate of these hydrocarbons in UHV systems should have eliminated this problem. However, these “adventitious hydrocarbons”, as they have come to be called, are observed to be present even without exposure to an electron beam. The mechanism of the deposition of carbon on a specimen when irradiated by an electron beam has been the subject of some debate [20]. It is proposed that hydrocarbons, either already present on the surface as adventitious hydrocarbons, or while impinging the surface from the vacuum are being cracked and deposited similar to Chemical Vapor Deposition, (CVD). In 1976 Broers and his group were working on novel lithography techniques and decided to take advantage of the carbon deposits to do high resolution lithography. Since then research continues along this avenue with the intentional introduction of various gases, called precursors, to deposit other materials such as silicon, tungsten, platinum, iron, gold, and silicon dioxide. When using adventitious hydrocarbon, the technique has become to be known as contamination lithography. When gaseous precursors are intentionally injected, the technique is referred to as Electron Beam Induced Deposition, (EBID). In most cases a modified Scanning Electron Microscope, (SEM), or systems designed to do Electron Beam Lithography, (EBL), are used to perform EBID studies. Figure 2-13 depicts a proposed Field Emission Array, (FEA), electron source preliminary design.

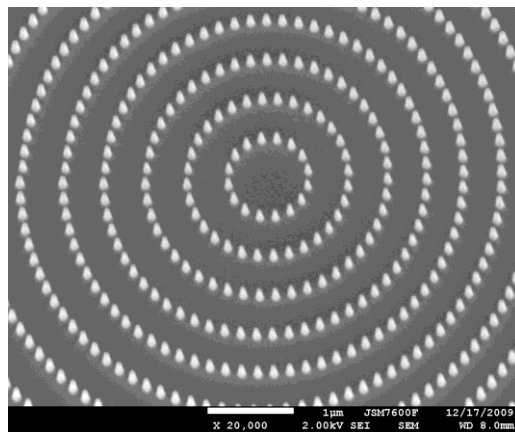


Figure 2-13: EBID deposit array formation proposed for Field Emission Array, (FEA), electron source.

In the past 20 years, commercial instruments have become available, such as the dual beam Focused Ion Beam, (FIB), instrument, which use either an ion beam, electron beam or both to deposit and or etch lithographic patterns. FIB systems are designed to purposely introduce various precursor gases, which are decomposed by the beam to form the deposit.

## 2.5. EBID Mechanics

The typical EBID process is depicted in Figure 2-14. A finely focused electron beam is used to decompose precursor gases adsorbed on the surface of a substrate in a vacuum system. EBID can be done inside the vacuum chamber of any energetic particle beam instrument, such as a Scanning Electron Microscope, (SEM), or a dedicated Electron Beam Lithography, (EBL), system as described previously [21].

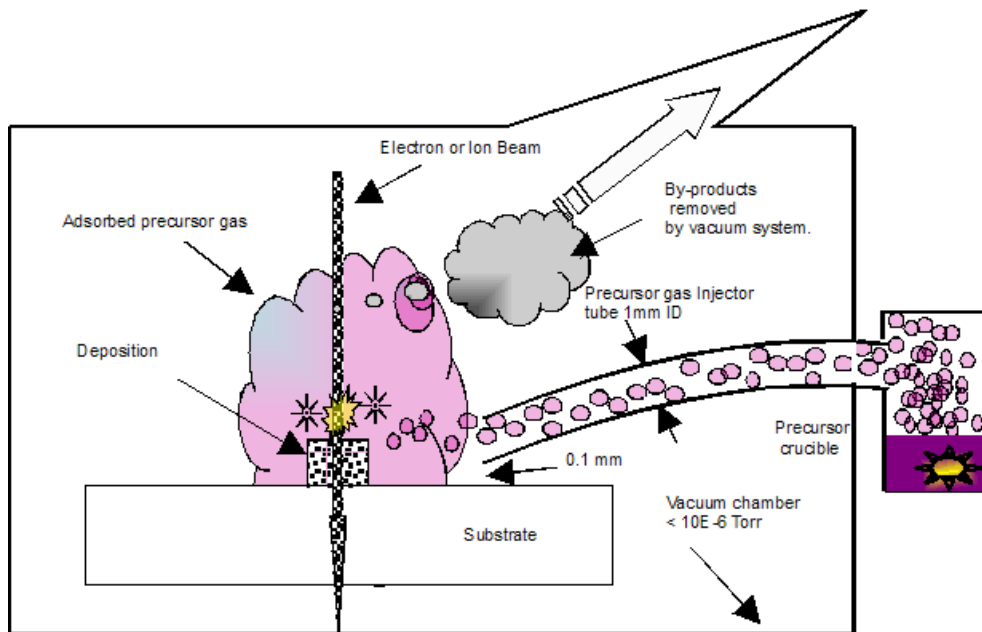


Figure 2-14: A finely focused electron beam is used to decompose precursor gases adsorbed on the surface of a substrate in a vacuum system. Adapted from [19].

In systems other than the FIB, which are not purposely designed to do this, the instrument has to be modified to allow for the introduction of precursor gases. In the typical experiment a precursor gas injection tube is brought near the sample surface, which is typically a few hundred microns from where

the deposition is to take place. Gas flow is precisely controlled to allow the system vacuum pumps to maintain a background pressure less than  $10^{-6}$  Torr. The electron beam is then positioned over the area where the deposition is to be recorded and finally scanned in a pattern to produce a desired result. The electron beam decomposes the gas, which creates a deposition, and proceeds to penetrate into or through the substrate, depending on the beam energy, and the average density of the material. The higher the beam energy and the lower in density the materials, the greater the depth of penetration. Surplus precursor gas, and reaction by-products are then removed by the instruments vacuum system. The adsorption rate of the precursor gas on the substrate is given by [22];

$$dN/dt = \{g F (1 - N/N_0)\} - \{N/t\} - \{q N f\} \quad (2.4)$$

where  $N$ , ( $\#/cm^2$ ), is the density of adsorbed molecules,  $N_0$ , ( $\#/cm^2$ ), is the molecule density in a monolayer,  $g$  is the sticking coefficient,  $F$ , ( $\#/cm^2/sec$ ), is the molecular flux density arriving on the substrate;  $t$  is the mean lifetime of the adsorbed molecule;  $q$ , ( $cm^2$ ), is the cross section for dissociation of the adsorbed molecules under electron bombardment, and  $f$ , ( $\#/cm^2/sec$ ), is the electron flux density. The layer growth rate  $R$ , ( $cm/sec$ ), is:

$$R = vNqf \quad (2.5)$$

where  $v$ , ( $cm^3$ ), is the volume occupied by a dissociated molecule. The first term of the adsorption rate  $dN/dt$  controls the adsorption of the precursor on the substrate. The second term is the loss by thermal desorption to the gas phase with time constant,  $t$ . The third term gives the electron induced dissociation rate of adsorbed molecules. From  $dN/dt$  it is evident that the growth rate depends on the cross section for dissociation of molecules in the path of the electron beam. The accelerating voltage of the electron beam can be adjusted to optimize the deposition efficiency. As a rule, the lower the energy, the higher the electron cross section, which yields a higher probability of electron interaction. At too low of an energy the cross section will drop off, which gives the lower limit. In addition, a lower mean free path, or higher

pressure will increase the EBID efficiency. Higher pressures will also result in an increased probability for electron-molecule collisions. EBID can be performed inside the vacuum chamber of any energetic particle beam instrument, such as a Scanning Electron Microscope, or a dedicated Electron Beam Lithography, (EBL), system. However, it can also be performed in a Scanning Transmission Electron Microscope, (STEM), or FIB.

## CHAPTER 3: FINITE ELEMENT MODELING OF THE CMA DESIGN

### 3.1. Introduction

Several finite element modeling software packages were used to attempt to simulate the CMA design. In the first attempt to simulate the CMA, the program SIMION was used and more recently ANSYS was also used for simple parallel plate capacitor simulations. In early versions of SIMION the smallest dimension allowed was 1 mm. Features in the design of the CMA require sub-millimeter accuracy. In the end, COMSOL was chosen due to its flexible unit system, and the built in ability to do multi-physics applications. COMSOL provides a cross-platform finite element analysis. Its solver and multi-physics simulation package has the ability to solve other types of engineering problems, which may arise in design. It was anticipated that due to the small size of the CMA design, heat radiation, and heat transfer problems could arise. COMSOL possesses modules ready to assist with these problems. It also possesses optics modules for future addition of simulations in the optical region of the EM spectrum. The EM spectrum is where lasers or UV light sources will be applied for future advanced design changes to the spectrometer. Future advanced designs may include Ultraviolet Photoelectron Spectroscopy, (UPS). This inclusion would provide an ultraviolet ionization source, or laser, which would be used for initial ionization instead of the electron source in the AES. The AES was under study in this research.

The simplest type of spectrometer considered in early work on electron spectroscopy was that of a parallel plate capacitor. Geometrically, because the CMA is axially symmetric any planar cross section, which includes the axis of the inner cylinder, becomes a parallel plate capacitor. Figure 3-1 presents a Computer Aided Design finite element simulation of a parallel plate capacitor using COMSOL.

The dimensions are in meters, the bottom plate was set at ground potential while the upper plate was set to minus 2000 volts. An electron is shown entering the gradient from the right at approximately

$3.00 \cdot 10^7$  m/s giving an energy of 2700 eV. The electron is repelled by the top plate, since V is negative with respect to ground, providing the resultant trajectory.

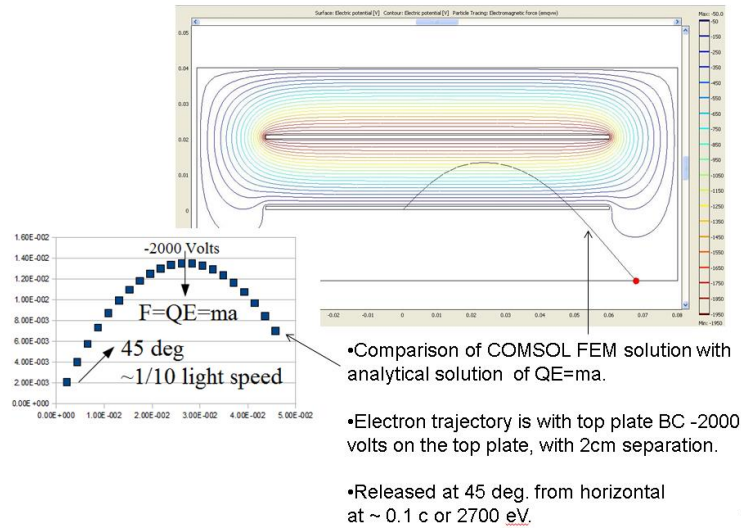


Figure 3-1: COMSOL FEM solution for a parallel plate capacitor.

As seen in this plot the colored lines show the gradient of the electric potential between the plates to simulate the inner and outer cylinder of the CMA. Also shown is the field fringing around the edges, where an electron flight solution is not so easy to solve analytically. The electron trajectory shows an almost exact agreement with the analytical solution with a maximum height of 0.0135 meters. The initial input velocity for the electron is one tenth the speed of light, which is equivalent to an electron energy of 2700 eV. The initial angle of entry through the inner cylinder plate is 45 degrees from horizontal with a gap of 2 cm between the inner and outer cylinder.

If it was assumed that the plates were of infinite dimension, the electric potential would be a uniform gradient of parallel lines, and it would be a simple matter to solve the problem analytically. This can be seen in the center of the parallel plate capacitor model shown in Figure 3-1. Due to the plate edges, the electric potential bends around the discontinuity in the geometry forming what is referred to as fringes. In this case, the finite element method can be used to create an array of mesh of points around the plate edges and solve for the Partial Differential Equations, (PDE), which, in this case, are the Poisson equations at each of the points. The desired accuracy and precision of the problem is simply a function of the number of points, computing power, and the time needed to solve the problem. The COMSOL multi-physics program assists in creating a CAD design of the geometry. It sets up the appropriate boundary conditions, material properties, and creates the mesh, which was used to solve the problem. The program has a variety



of built in post processing capabilities, which provide for graphical interpretation, and visualization of the solutions. It also has a built in particle tracking function, which provides for injection of a particle at a given initial location and velocity. COMSOL then plots the resultant trajectory through the electric potential gradient as shown in Figure 3-1. The parallel plate capacitor is perhaps the simplest device conceived that can be easily constructed and modeled for separation of ballistic electrons of different energies.

### 3.2. Spectrometer Design and FEM Modeling Process

The first step in the FEM simulation is to create a to scale CAD drawing, which is input into COMSOL as the geometry of the problem. Figure 3-2 shows the geometry of the spectrometer used to simulate this double pass CMA design. The CAD design was drawn to scale directly in the COMSOL program.

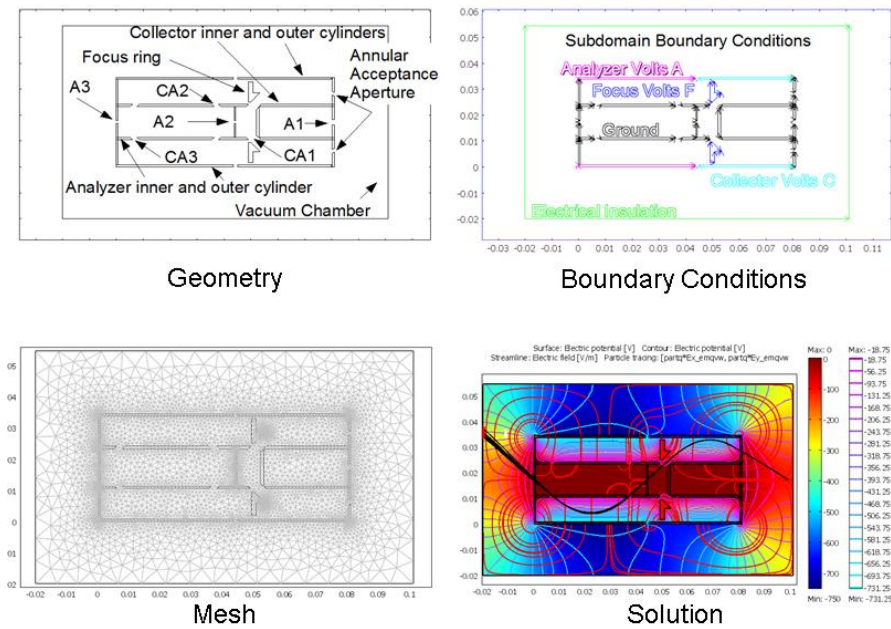


Figure 3-2: COMSOL CAD FEM model for proposed double pass electron spectrometer.

The geometry components labeled CA1-CA3 are circular apertures in the inner cylinder, which are set at ground potential. The beam from the electron source inside the inner cylinder exits from aperture A1. Apertures A1-A3, and the entire inner cylinder are all at ground potential. The collector, analyzer, and focus, were set to -650, -750, and -90 volts respectively. Auger electrons at 1000 eV enter the circular acceptance aperture traveling from right to left as seen in the solution.

Each component of the geometry is assigned a boundary condition, which, is input as a variable into the solver. An additional boundary condition, labeled as electrical insulation, defines a finite outer boundary for the problem. Next, the entire domain is meshed automatically by COMSOL. The mesh may be refined manually where there are edges and discontinuities in the geometry. After the mesh is generated, the problem is then solved and the gradient of the electric potential is plotted. With the electric field known at every point, COMSOL has an option, which allows for electron flight simulation by solving the equation of motion.

Some models of commercial electron spectrometers use two CMAs back to back to form what is known as a double pass CMA. The double pass CMA spectrometer allows for higher resolution of the Auger spectral peaks. It also allows for a larger distance between the nose of the spectrometer where the electrons enter, and the sample. This distance is commonly referred to as the Working Distance, (WD).

The design is a scaled down version of a commercial double pass CMA, which was designed to be mounted on an 8 in diameter UHV conflat flange. A photo of the outer cylinder taken out of a large commercial CMA and the miniature CMA is shown in Figure 3-3 for comparison along with a ruler for scale. The miniature CMA is scaled down to  $\frac{1}{4}$  the size of the 8 in mount CMA to allow for mounting on a  $2\frac{3}{4}$  in conflat flange.

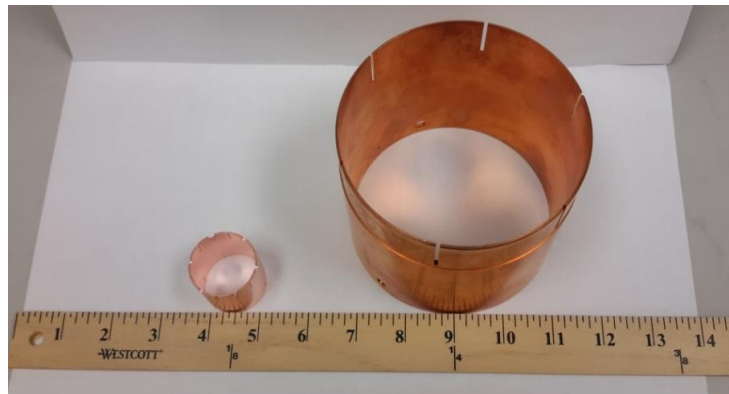


*Figure 3-3: Photo comparison of outer cylinders from miniature and commercial CMA. The small cylinder on the left is the outer cylinder from the miniature CMA, with the large commercial outer cylinder shown on the right. Both cylinders are made from pure oxygen free high temperature copper OFHC.*

Figure 3-2 depicts the geometry of this model, and shows all the apertures and elements, which filter the electrons emitted from the specimen. All the components of the spectrometer, which are included in the simulation are labeled. An electron gun mounted in the center of the spectrometer is used to focus a beam of electrons through aperture A1 on to the specimen. The primary electron beam acts as a point source and causes the sample to emit SE's, BSE's, and Auger electrons radially in all directions. Those emitted at the proper angle will enter the annular acceptance aperture on the way into the collector section of the spectrometer. The electrons are repelled by a negative potential set on the outer cylinder, which is labeled in light blue as Collector Volts C. The electrons then encounter an additional repulsion from a component labeled as Focus ring with a boundary condition of Focus Volts F. The focus ring directs the electrons through the CA1 circular aperture. The focus electrode was added to provide a shorter length spectrometer while still maintaining a large working distance. The electrons that pass through the circular aperture CA1 then travel through aperture A2, which separates the collector CMA section from the Analyzer section of the CMA. After emerging from aperture A2 the electrons pass through the circular aperture C2 where they encounter a negative potential from the outer cylinder of the electron analyzer section of the spectrometer. The analyzer is labeled as Analyzer Volts A. The inner cylinder of both sections of the spectrometer was set with a boundary condition of ground potential. The electron trajectory along this entire path is plotted in black in the COMSOL solution. The solution is shown in the lower right section of Figure 3-2. It is shown with a larger view in Figure 3-4.

The electrons in the above simulation were given an initial potential  $E$  of 1000 volts at 32.5 degrees from the horizontal. The boundary conditions and spectrometer voltages are shown in Table 3-1 along with the electron energy, and the velocity components, which are required inputs for the equation of motion.

Table 3-1: Constants and variables input into FEM for solution of the double pass CMA.

Name	Expression	Value	Description
E	1000	1000	Energy eV
C	-650	-650	Collector Volts
A	-750	-750	Analyzer Volts
F	-90	-90	Focus ring Volts
Vtot	$-(2 * E_j / 9.1095e-31)^{.5}$	-1.875525e7	Velocity m\s
Ej	$E * 1.60217653e-19$	1.602177e-16	Energy J
eVx	$V_{tot} * \cos(R)$	-1.581802e7	Velocity X
eVy	$V_{tot} * \sin(R)$	-1.007719e7	Velocity Y
R	$T * 2 * \pi / 360$	0.567232	Radians
T	32.5	32.5	Theta Degrees

Figure 3-4 provides the solution in detail. The electron trajectory is plotted with the electron potential, in volts, shown as both stream lines, and as a range of colors with 0 volts as dark red, and -750 volts as dark blue. The electron path is shown as a black line and the dimensions are in meters. The electrons leave the sample under analysis from the right. They travel from right to left through the spectrometer at approximately ½ of one percent of the speed of light. One hundred electrons were released along a line representing an electron beam spot the size of 100 microns in diameter.

The solution shows the designed geometry of the spectrometer. It also shows the set of boundary conditions required to successfully pass 1000 eV electrons through the spectrometer. These electrons are counted by an electron multiplier detector attached to the exit aperture labeled A3 in Figure 3-2. The output from the detector in this simulation, if it were plotted, would show a peak in the Auger spectrum at 1000 eV kinetic energy.

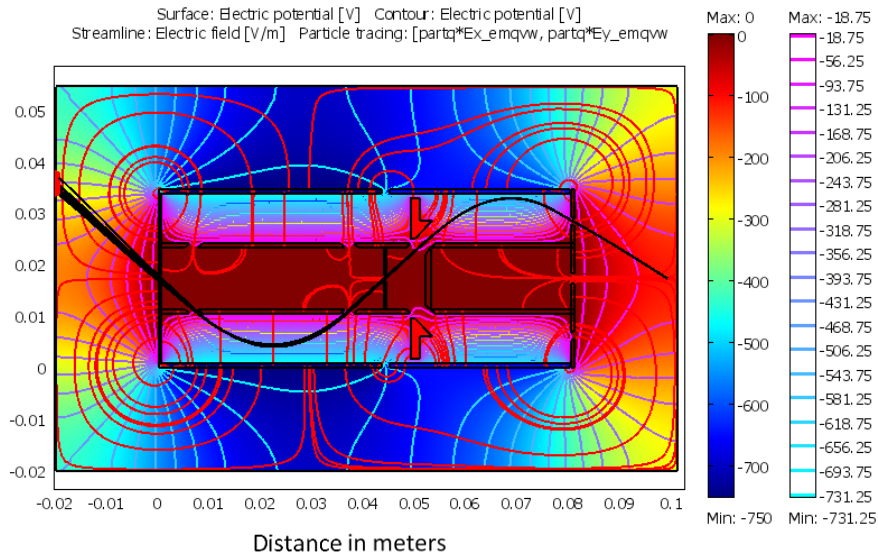


Figure 3-4: COMSOL CAD FEM solution for proposed double pass electron spectrometer.

### 3.3. FEM Model of Electron Source with Einzel Lens

Figure 3-5 shows the geometry and COMSOL FEM solution for the proposed thermionic electron source with Einzel lens, which is mounted inside the inner cylinder of the CMA. This electron source is used to focus a beam of electrons on the sample. This design consists of three metal washers, which are shown in a cross section view in Figure 3-5. The center washer is electrically insulated from the top and bottom washers, and is set at a potential of -100 volts. By varying the focus voltage on the center washer, the focus length or WD of the electron beam can be adjusted such that the beam is in focus on the surface of the sample to be analyzed. In this simulation, 100 electrons were released from a line above the washer on top in order to simulate the emission from the surface of a tungsten thermionic emission source. The electrons were released into the Einzel lens with an initial velocity equivalent to 3 KeV of energy. Figure 3-6 shows the Einzel lens solution in detail with the electric potential plotted as colored stream lines with red indicating 0 volts and blue indicating -100 volts. As shown in the solution plot, the lens acts to focus the electron beam to a point below the lens and the focal distance is adjusted by varying the voltage on the center washer. As the voltage is increased, the focal point will move closer to the lens. With a focus voltage of zero, the beam will go through the lens unchanged from its initial diameter.

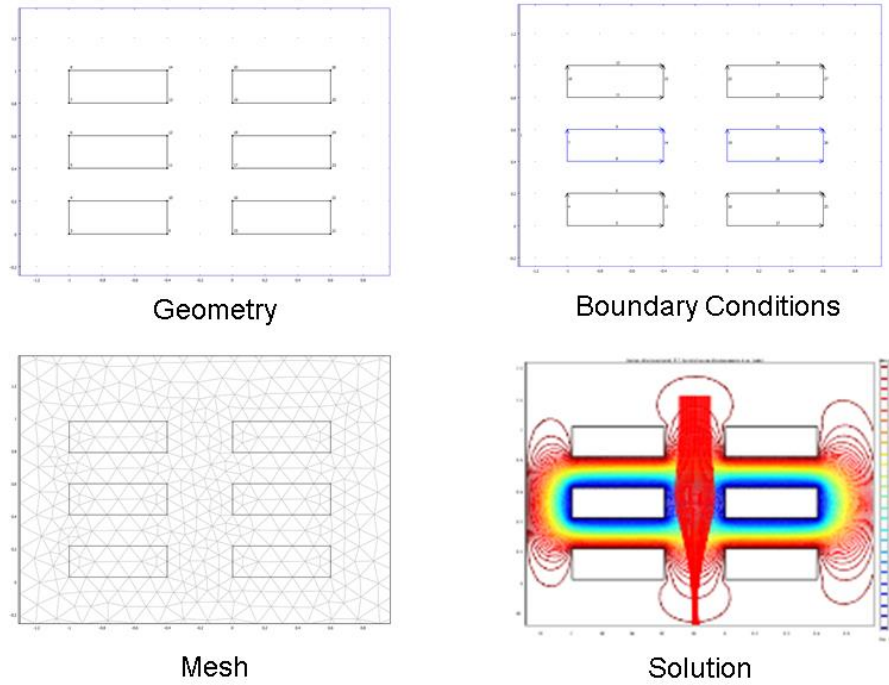


Figure 3-5: COMSOL CAD FEM solution example of electron source with Einzel lens. The Einzel lens geometry consists of a concentric arrangement of 3 metal washers. The center washer is the focusing element, which can be adjusted to focus a beam of electrons, which enter from the electron source. The focus voltage was set to -100 volts to focus a beam of 3 KeV electrons entering from the top as shown.

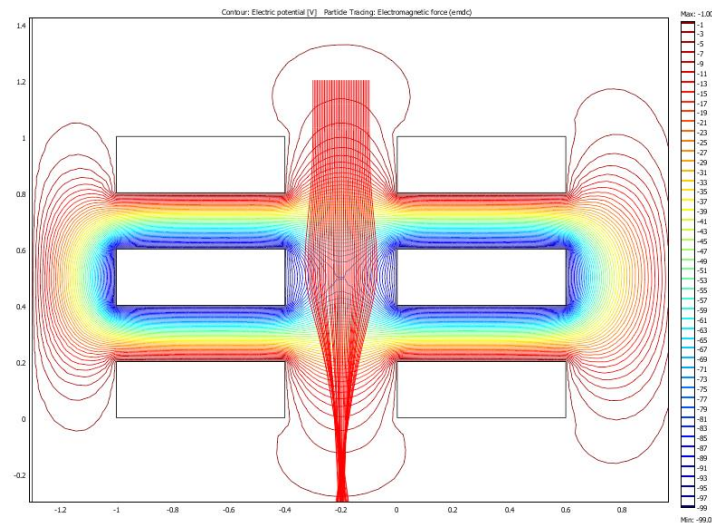


Figure 3-6: FEM solution for electron source with Einzel lens.

## CHAPTER 4: SUPPRESSION OF SECONDARY ELECTRONS IN CMA

### 4.1. Introduction

In any type of spectroscopy, noise in the spectrum diminishes the sensitivity of the spectrometer. This becomes a problem, particularly when high sensitivity is needed, such as when trying to identify elements at a trace level in the sample. Typical detection limits for Auger spectroscopy have an order of magnitude range from 0.1 to 1% for the elements in the periodic table. Silver being the most sensitive and yttrium the least. However, as shown in Figure 4-1, with large electron beam current, and large concomitant beam size, the sensitivity can be quite high, as high as 0.001 % of a monolayer. The sensitivity limit is set by the signal to noise ratio. A typical signal to noise ratio is 800:1 for the Cu LMM line. This ratio allows for a detection limit of about 1% of a monolayer at a special resolution of 0.1  $\mu\text{m}$  with fixed primary beam current of 10 nA [23].

The detection limit may also be set by the beam current available, which depends on the instrument settings and the type of electron source used. The sensitivity of the material under analysis to damage by the electron beam is also a limiting factor to the magnitude of the beam current density, which can be applied. Using an electron beam at just 3 kV energy, with a small current of 10 pA,  $10 \times 10^{-12}$  amperes, and a spot size of 1 nm diameter, the current density is 1000 A/cm<sup>2</sup>. Thus, power density levels can exceed several megawatts per cm<sup>2</sup>. To put this in perspective, the recommended current capacity of copper wire is a few hundred A/cm<sup>2</sup> depending on the insulation and the ambient conditions. The electro-migration in copper interconnects becomes a problem in the  $10^5$  to  $10^6$  A/cm<sup>2</sup> range in Very Large Scale Integrated Devices (VSLI) [24].

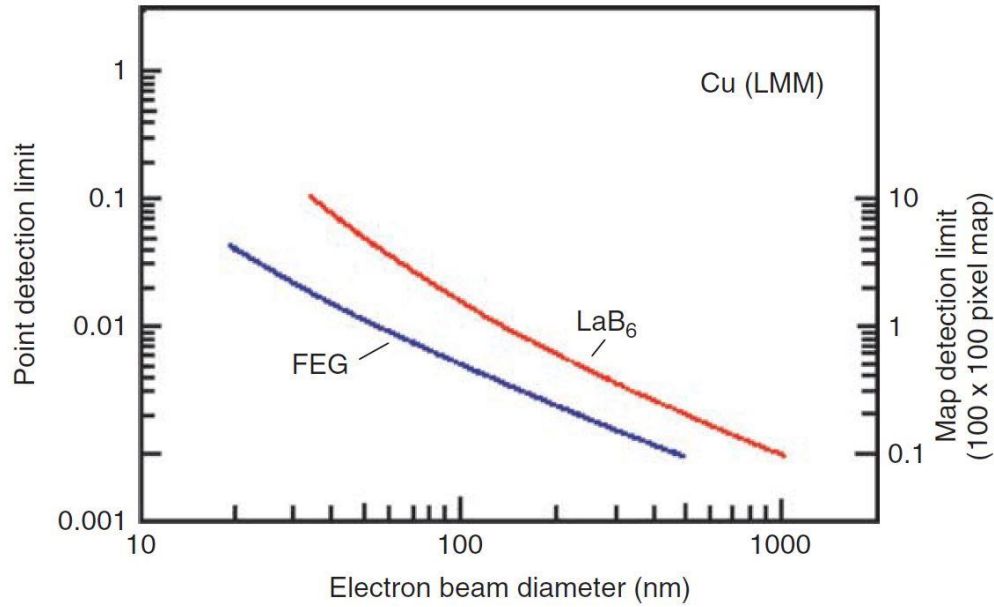


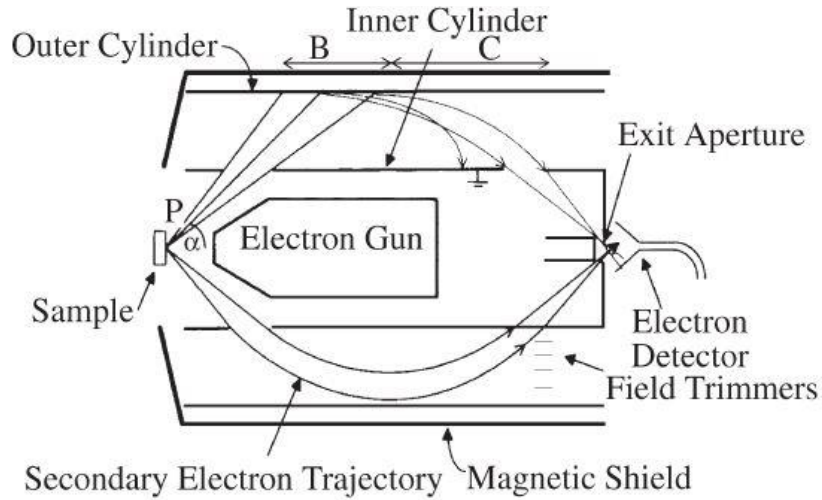
Figure 4-1: Detection limit of copper in a film one atom thick. The limit is a function of the electron beam size for two types of electron source. Lanthanum Hexaboride, ( $\text{LaB}_6$ ), is plotted in red and Field Emission Gun, (FEG), in blue [24].

#### 4.2. Electron Spectrometer Background Noise

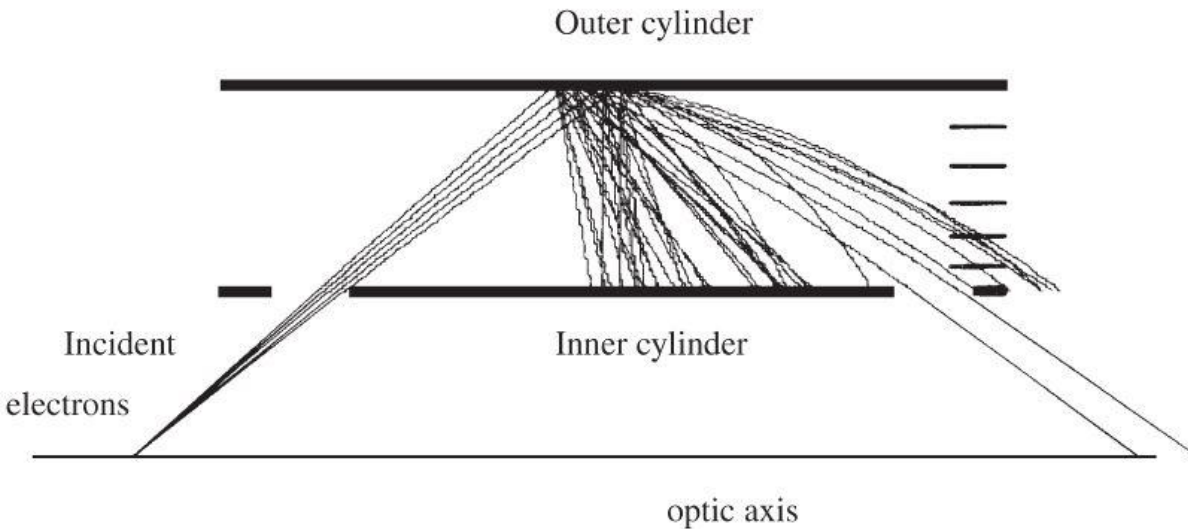
Sources of noise in the CMA spectrometer have been a concern since early designs [25]. One main source of noise is from scattering of electrons on the inside surfaces of the spectrometer. Figure 4-2 (a) shows a typical CMA experiment in which a focused beam of electrons from the electron gun excite emission of radiation from the sample [26]. As shown earlier, in Figure 2-9, many types of electrons and other forms of radiation are emitted from the sample due to the interaction of the primary beam with matter. The radiation scatters in all directions, but only radiation with a narrow solid angle can enter the inside of the spectrometer through the aperture opening in the inner cylinder without being physically blocked. Depending on the spectrometer design only those electrons, which subtend the angle  $\alpha$  of approximately six degrees can make it through to the inner cylinder. Considering the geometry in Figure 4-2 (a), it can be observed that electrons will land along some distance represented as length B, on the inside



surface of the outer cylinder. With the spectrometer tuned to a specific energy, only those electrons within a small pass energy,  $\Delta E$ , will reach the detector unimpeded.



(a)



(b)

Figure 4-2: Possible sources of secondary electron noise in the CMA [26] [27].

(a) When the spectrometer is tuned to pass low energy electrons, electrons from the sample with higher energies than this may strike the inner surfaces of the outer cylinder and generate secondary electrons. Some of these may have the right energies and angle of emission to reach the electron detector, as depicted. (b) Electron trajectory simulation of secondary electrons generated at the outer cylinder with random energies up to those used to generate them. The case depicted is for an incident beam of 1000 eV and pass energy of 500 eV. It is obvious that all secondary electrons are accelerated towards the inner cylinder, while for the backscattered electrons, the majority strikes the field trimmers, but some manage to exit from the inner cylinder aperture.

These electrons are labeled secondary electron trajectory in Figure 4-2: Possible sources of secondary electron noise in the CMA . Electrons with higher energy than the pass energy,  $\Delta E$ , will strike the outer cylinder generating SE's and BSE's, which can bounce in many random directions inside the spectrometer. Those electrons that are able to reach the detector create noise in the spectrum.

Figure 4-2 (b) shows an electron trajectory simulation of secondary electrons generated at the outer cylinder with random energies up to those used to generate them. In this simulation, the electron energy was set to 1000 eV, with the spectrometer set for a pass energy of 500 eV [26]. A large number of SE's and BSE's scattering from the outer cylinder may hit the inner cylinder. Then they may undergo multiple reflections inside hitting the outer cylinder once again, along the length of the outer cylinder represented as length C in Figure 4-2 (a). After multiple scattering events, the kinetic energy of these electrons will ultimately be converted to other forms of radiation. Additionally, many electrons will ultimately make their way out of the exit aperture of the inner cylinder, and contribute to the noise background in the spectrum.

In Figure 4-3 (a), Goldstein shows the complete spectrum of electrons emitted from a sample bombarded with a focused electron beam from an electron source [28]. Therefore, the electron spectrometer must contend with a large amount of electrons, which may enter over a broad energy range, labeled as region II in Figure 4-3. The width of the SE peak in region I is greatly exaggerated here just for illustration. If drawn to scale it would appear as a narrow line. The actual SE peak width is shown in Figure 4-3 (b) to be only ~5 eV FWHM, with a peak of around 2.5 eV. Figure 4-4 shows a more descriptive picture of the energy range along with the addition of a few Auger electron peaks, which are riding on top of the broad range of inelastic BSE's. These peaks are located between the SE peak and the low loss peak, which represent elastic BSE's [29].

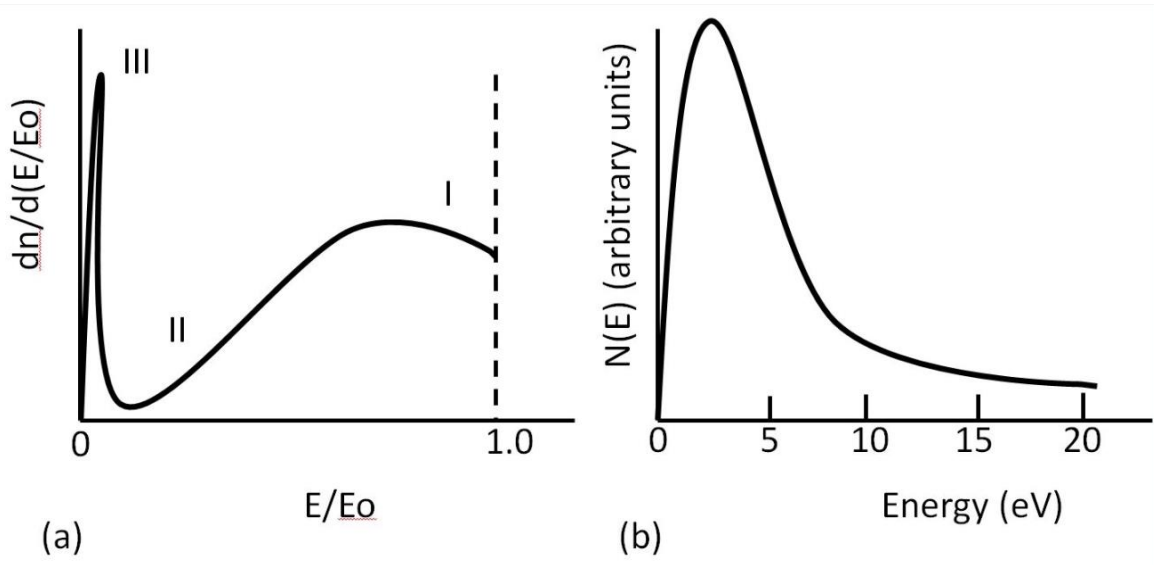


Figure 4-3: Complete normalized energy distribution of electrons emitted from a target. (a) Region I identifies elastically backscattered primary electrons of energy  $E_0$ . Region III are secondary electrons ejected from the sample by the primary electrons. The broad region II, between region I and III are backscattered electrons, which have undergone inelastic collisions in the sample. (b) If  $E_0$  is 1000 eV, the width of region III is very narrow, only 5 to 10 eV, as shown in a magnified view on the right [28].

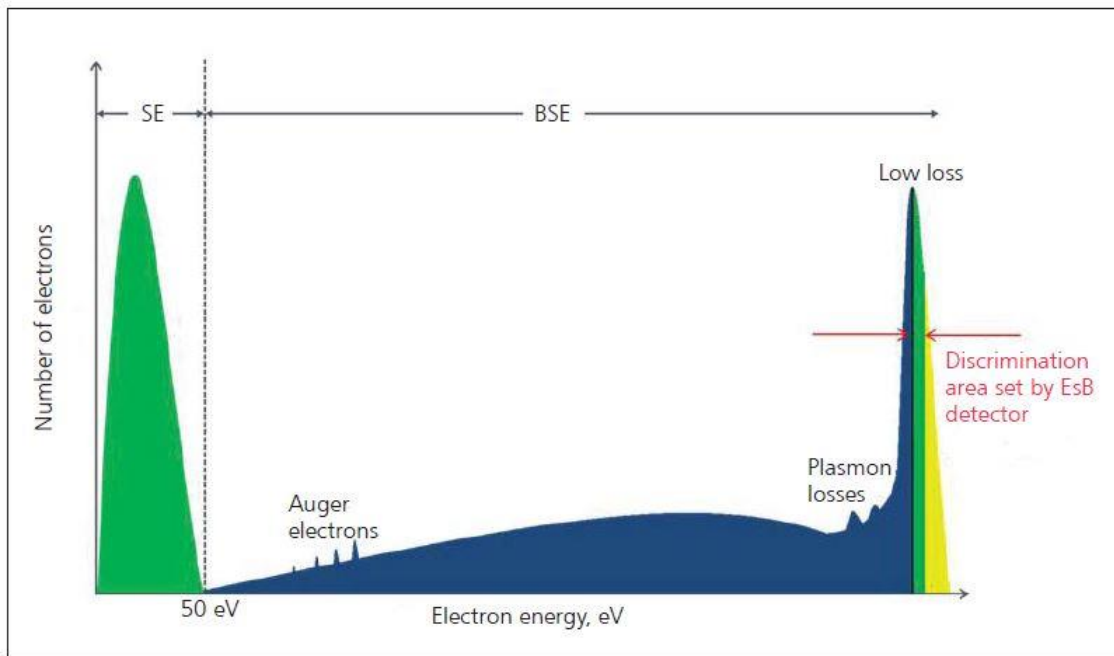


Figure 4-4: Energy distribution of electrons emitted from a target with Auger peaks. The two large peaks in the spectrum are secondary electrons SE, and Low loss BSE. The region between the SE and Low loss peaks show a wide background of inelastic BSE on top of which the Auger electron peaks are found. The low loss peak represents the energy of elastically scattered BSE at the energy of the primary beam focused on the sample.

### 4.3. Secondary Electron Suppression

In CMA design, attempts to suppress the SE noise in the Auger spectrum from the electron scatterings mechanisms, discussed in Section 4.2, have met with limited success. Experiments by Bakush and Gomati in which the outer cylinder was machined with 0.5 mm saw-tooth grooves showed almost no difference in signal to noise ratio in the Auger spectrum compared to a smooth unaltered cylinder [27]. Figure 4-5 shows the saw-tooth pattern, which was designed to block errant SE's, and reflect the electrons in a direction opposite to the detector.

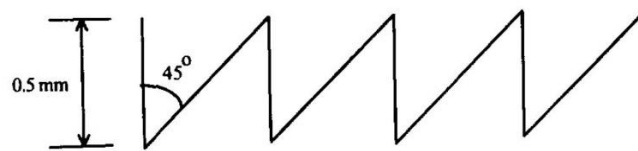


Figure 4-5: Mechanically machined saw-tooth grooves for SE suppression. Grooves in the shape of a saw-tooth were cut into the outer cylinder at an angle of 45 degrees, and a depth of 0.5 mm with a pitch of 32 teeth per inch [27].

In this experiment, the original smooth outer cylinder from a commercial CMA was replaced with a metal cylinder, the same in all respects, except for having the saw-tooth pattern machined on the inner surface of the outer cylinder. In addition, a primary beam voltage of 5 kV was used at a current of  $10^{-6}$  Amperes, which yielded a beam spot size of 0.5 microns. Auger spectra were collected on pure Au and Cu samples to determine the difference in signal to noise ratio between the original commercial smooth outer cylinder, and the saw-tooth machined cylinder. The results are presented in Table 4-1.

Table 4-1: Peak to background ratios measured from Auger spectra on Au and Cu. The ratios are nearly unchanged when comparing the smooth outer cylinder with saw-tooth cylinder designed to suppress SE's [27].

Type of Cylinder	(P/B) <sub>865,Cu</sub>	(P/B) <sub>325,Ag</sub>
Smooth Surface	0.017 +/- 1.0%	0.35 +/- 1.0%
Sawtooth Surface	0.016 +/- 1.0%	0.36 +/- 1.0%

#### 4.4. Electron Beam Deposition of Thin Films

Thin films of silicon were deposited by high power Electron Beam Physical Vapor Deposition, (EB-PVD), on OFHC substrates as a first attempt to improve the signal to noise ratio in the spectrometer. The process is depicted in Figure 4-6. EB-PVD is a very versatile tool for research in thin film devices. With available power levels of hundreds of kilowatts, nearly any substance can be vaporized or sublimated on to a substrate. Due to the high power density of a focused beam of electrons, very high deposition rates can be obtained.

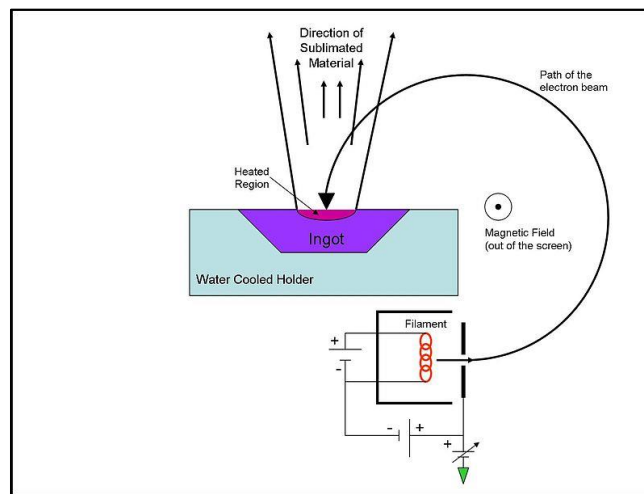


Figure 4-6: Geometry of 270 degree electron beam deposition source.

*The crucible of material to be evaporated is held at a positive potential relative to the filament. To avoid damage to the filament and contamination of the material, the filament is kept out of direct line of sight. A magnetic field acts using the Lorentz force to bend the electron beam through a 270 degree arc from its source to the crucible. An additional electromagnet is used to align the beam over the center of the crucible to prevent melting the entire apparatus.*

From gas kinetic theory, assuming a sticking coefficient of one, contaminant gases in a vacuum system, such as carbon monoxide, arrive at the surface of a substrate at a rate of one monolayer per second when the gas pressure on the substrate is one micro-Torr. The unit of gas dose a substrate receives is defined in units of Langmuir's. One Langmuir is the dose of gas a surface receives after being exposed to a pressure of 1 micro-Torr for one second [30].

The Langmuir is dimensionally non-homogeneous but is still of great use in estimating the rate of arrival of matter on a substrate to determine order of magnitude effects and reaction rates of gases on a

substrate in high vacuum systems. Experimental results showed that this approach was effective in suppressing SE emission. However, silicon films deposited by EB-PVD did not adhere well to the copper substrate.

#### 4.4.1. Laser Beam Machining

One proposed method for suppression of SE emission in the spectrometer is to machine structures into the surfaces of the inner and outer cylinders, which may be exposed to stray electrons that may scatter into the detector. Some previous work toward this was performed by Bakush and Gomati as discussed in Chapter 3 [27]. The method used by these authors was shown not to have any effect on reducing the secondary electron emission of the outer cylinder of a commercial CMA. In this research, Oxygen Free High-temperature Copper, (OFHC), of the same type as that used in a commercial CMA, was machined using a 30 megawatt peak power pulsed Neodymium Vanadate laser, (Nd-YVO<sub>4</sub>). The Lumera SUPER RAPID-HE Picosecond laser has a 5x lens with a spot size of 16 μm. The laser wavelength is in the infrared at 1064 nm, a pulse width of 15 picoseconds, and a pulse repetition rate up to 100 kHz. The average power can be adjusted as high as 10 watts. The laser system is a 3D machining and printing instrument which is described in [31] [32]. To machine the Faraday Cup, (FC), array, the laser was set to 3 watts with a linear scan speed of 50 mm per second, which was considered optimal from previous work [32]. OFHC is widely used in UHV vacuum system design such as in electron spectrometers, and X-ray sources. In addition, it is used for many structural components such as electrodes and gaskets to seal flanges in UHV systems. In this research, a standard 2 3/4 in diameter OFHC gasket was used as a substrate to simulate the outer cylinder material used in CMA design. As well as being the same material as the CMA cylinders, the thickness was also similar.

The laser system was used to machine an array of copper needles with deep pockets between them to act as Faraday Cups) in order to absorb SE electrons. To produce this array, the scanning stage of an nScript 3D laser printer was programmed to scan the OFHC substrate in a series of vertical and horizontal

lines with a spacing of 50 x 50 microns. Experiments were performed to determine the laser power needed to cut deep grooves in the substrate. A range of three laser powers, 0.5, 1.5, and 3 watts were used. It was determined that 3 watts was needed to cut grooves in the OFHC copper, which caused dark patches to appear in the copper. Figure 4-7 shows the LBM milled areas labeled, 3w1p, 3w3p, and 3w6p. All three areas were milled with 3 watts of power, and with 1, 3, and 6 repeated passes of the 50 x 50 cross hatch pattern. An accidental overlay of the two adjacent laser milled areas formed a dark line, which is labeled as dark patch in Figure 4-7. These results indicated that more laser power was needed to cut deep enough grooves in the copper to produce the SE absorbing structures. As shown here, and as would be expected, the 3w6p area also appeared darker due to the deep grooves formed.

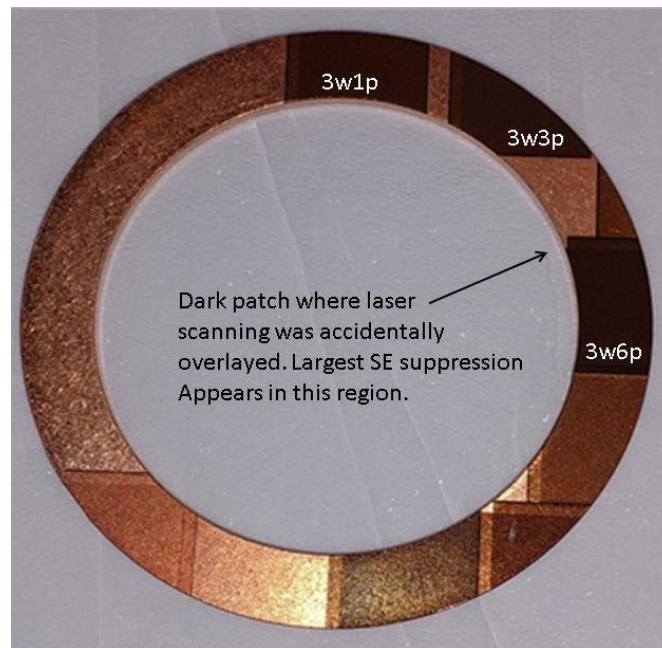


*Figure 4-7: Nd:Vanadate, (Nd:YVO<sub>4</sub>), Laser Beam Machining, (LBM), of Faraday Cup, (FC), array. LBM was performed on OFHC copper gasket with several power doses to mill an array FC's designed to act as a secondary election suppressor. Regions 3w1p, 3w3p, and 3w6p, received 3 watts with 1, 3, and 6 repeated passes with 50 x 50 micron cross hatch pattern.*

Figure 4-8 shows the SEM images of the dark patch illustrated in Figure 4-7 above. Figure 4-8 (b) shows the SE emission waveform, which shows a dramatic decrease of the SE emission in the dark patch region.

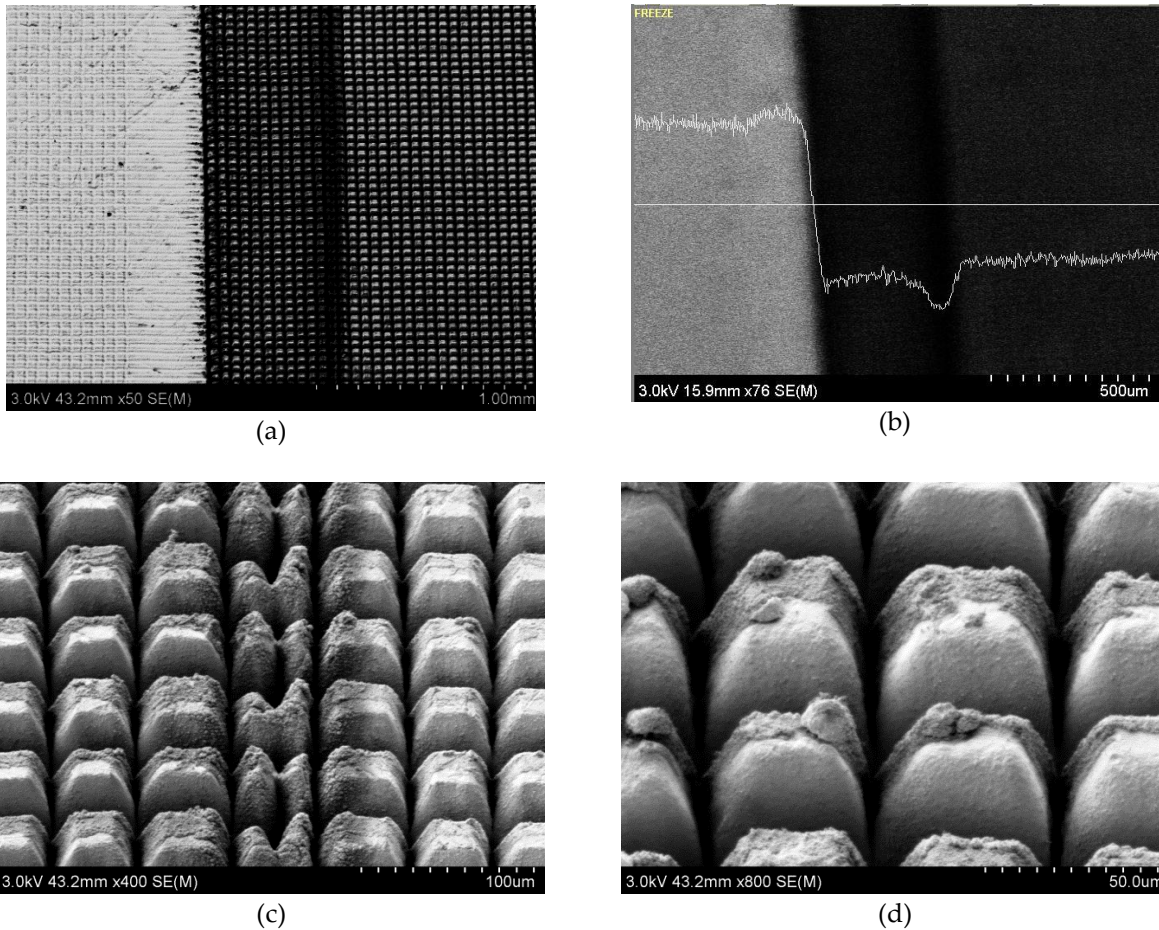


Figure 4-8: Was ist das für ein dunkler fleck? (What is that dark patch?).

Secondary electron image, and SE emission waveform overlay on laser milled OFHC. Laser machining was performed on OFHC copper gasket with 3 watts average power in a cross hatch pattern with a 50 x50 micron spacing. Images a –d are secondary electron images and SE emission waveform taken with a beam energy of 3 keV electrons. The solid white line shows the location of a line scan. The SE emission waveform in (b) shows a large decrease in SE emission where a large dose of laser energy was accidentally applied. The dip in emission corresponds with the dark patch shown in (a).

To cut deeper structures, the laser scan spacing was decreased to 25 x 25 microns with laser power of 3 watts and 6 repeated passes of the laser over a 10 x 10 mm area. Figure 4-9 depicts this as a dark rectangle one cm<sup>2</sup>, which can be observed at the 12 o'clock position on the gasket substrate. The 25 x 25 laser scan spacing produced a LBM structure composed of an array of FC's SE absorbing pillars with an area density of  $1.6 \times 10^5$  FC's per cm<sup>2</sup>. Electrons, which strike the array, have a low probability of escape and thus acts as an electron suppressor. In addition, it can be concluded that the rectangle appears dark



since it acts as a light absorber as well. Light which falls into the voids of the FC array undergoes multiple scattering.



*Figure 4-9: Nd:Vanadate, (Nd:YVO<sub>4</sub>), laser machining of Faraday Cup array. Laser machining was performed on OFHC copper gasket to mill an array of micro Faraday Cups to act as a secondary electron suppressor. The dark rectangle seen at the top of the gasket was milled in a cross hatch pattern with an average laser power of 3 watts.*

Figure 4-10 (a) shows a SEM image at 50x magnification of the edge inside edge of the OFHC gasket, which shows a substrate thickness of 1mm. At this location one corner of the 10 x 10 mm LBM milled area went over the inside edge of the substrate. The SEM image in Figure 4-8 (b) shows a magnified view of this area at 200x magnification where deep grooves, approximately 200  $\mu\text{m}$  deep, were formed at

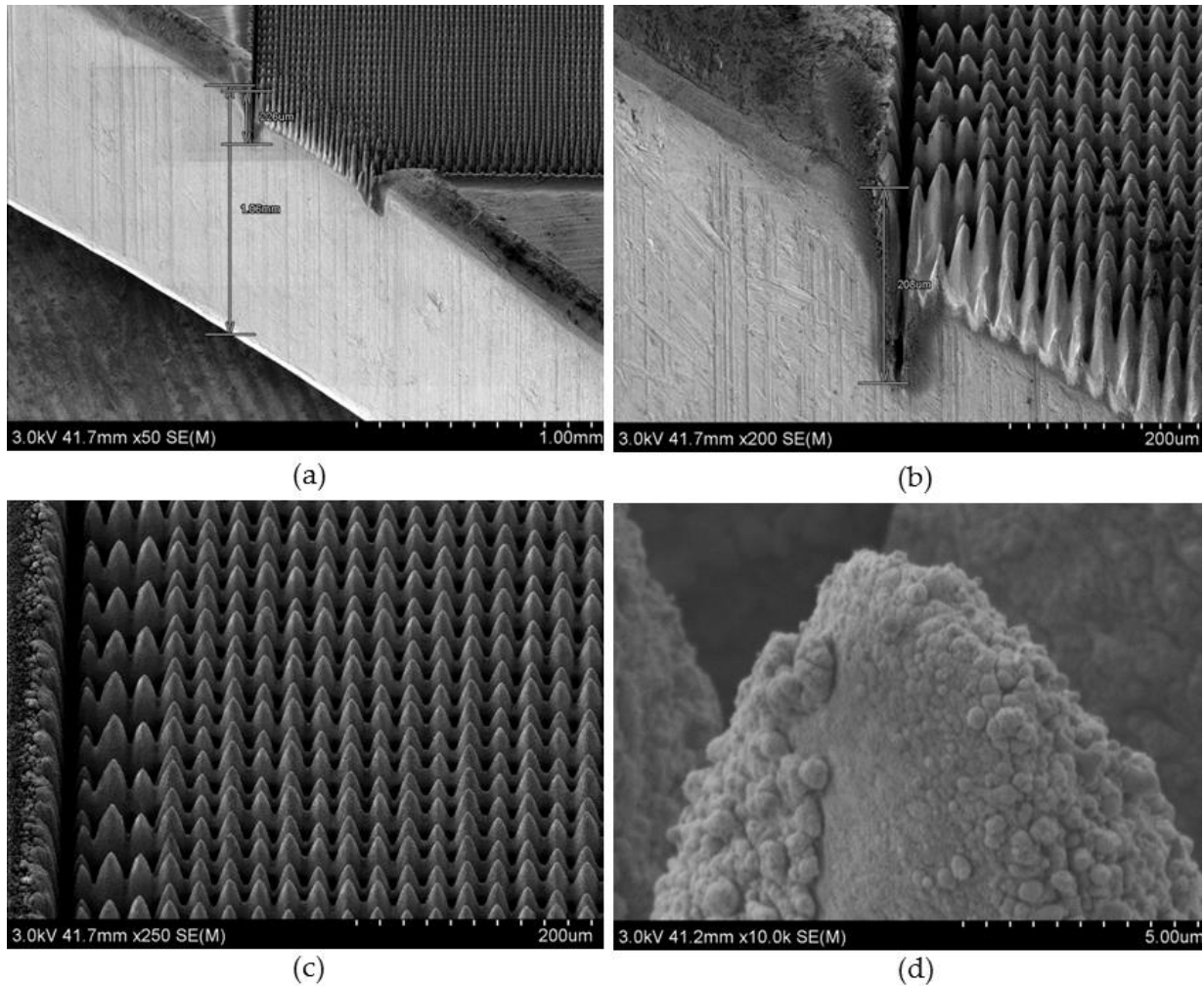


Figure 4-10: SEM image of laser machined Faraday Cup array.

In this SEM the depth of laser milling in (a) and (b) is shown to be about 0.2 mm deep or 200  $\mu\text{m}$  into the 1mm thick OFHC substrate. In the 10 x 10 mm laser machined rectangle, an array of cones are formed 100  $\mu\text{m}$  in height. Higher magnification images (c) and (d) show the FC array is formed of micron size cones covered with nano-spheres, which range in size from a few nanometers to 1 micron. The cones themselves range in size from a few microns to 25  $\mu\text{m}$  at the base.

The edge of the 10 x 10 mm milled area. This is due to the increased laser dose the substrate received since the laser changes must stop on the edge to change scan direction for each line scanned. The LBM machined pillars were formed in as an array with a 25 x 25 micron scan spacing as seen in Figure 4-10 (c). Figure 4-10 (d) taken at 10kx magnification, shows a high magnification of one pillar showing it is covered with a range of small Nano spheres.

Energy Dispersive Spectroscopy, (EDS), of the LBM area was performed in the center of the final 10 x 10 mm LBM FC structure as shown in Figures 4-10 (a) and (b). Table 4-2 shows a quantitative elemental EDS analysis, which shows the area to be 98% copper with 2% oxygen.

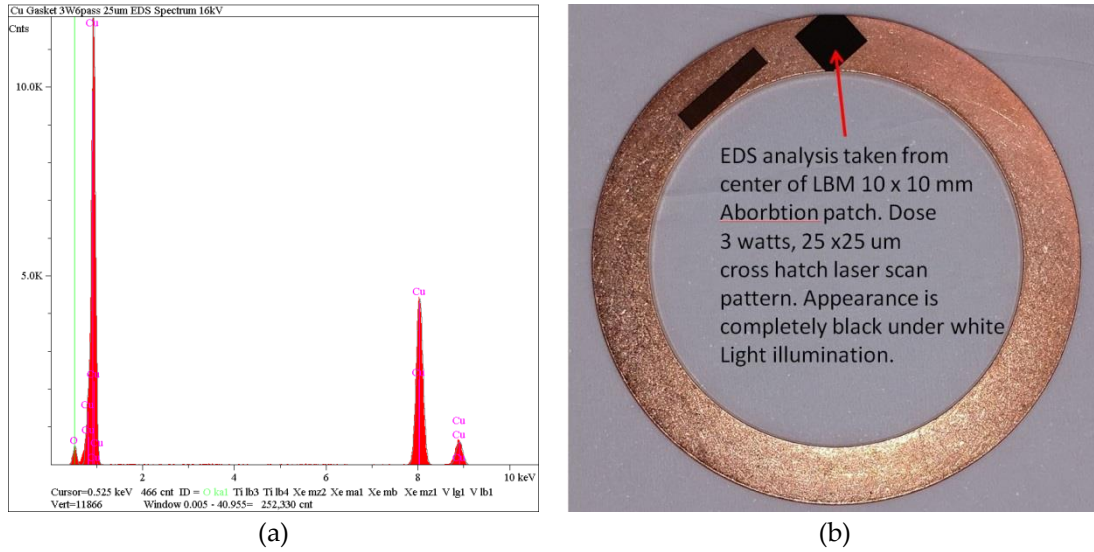


Figure 4-11: SEM EDS spectrum and analysis area of LBM FC array. (a) Energy Dispersive Spectroscopy, (EDS), spectrum performed on the FC array rectangle. (b) Quantitative analysis shows it to be nearly pure Cu 98% by weight with 2% oxygen. The heat from the laser may be oxidizing the copper to some extent.

Table 4-2: SEM EDS quantitative elemental analysis area of LBM FC array.

Element	Line	Intensity (c/s)	Error 2-sig	Low keV	High keV	Atomic %	Conc.	Units	
Oxygen	Kα	82.02	2.574	0.471	0.579	7.545	2.013	wt%	
Copper	Kα	1306.40	9613	7.949	8.147	92.455	97.987	wt%	
						100.000	100.000	wt%	Total
kV 16	Tilt 30°	TOA 60°	LT 60s						
							98%	Copper	Total

#### 4.5. Conclusion

High energy pulsed LBM was used to create an array of cones approximately 100 um in height. High magnification SEM images show the cones to have a base diameter of roughly 25 um, and a tip radius

of one to two microns. The cones are covered with nanospheres, which range in size from nanometers to 1  $\mu\text{m}$  in size. This creates an Extremely High Surface Area (ESHA) structure capable of absorption of charged particles and thus acts to suppress SE emission. The combination of high surface area combined with the cone structures covered in nanospheres may also explain why it appears black since it seems to be absorbing a range of Electro-Magnetic, (EM), radiation.

## CHAPTER 5: SEM MEASUREMENTS OF SE SUPPRESSION ON LBM OFHC FC ARRAY

### 5.1. Introduction

In using the Scanning Electron Microscope, (SEM), and when performing Electron Beam Lithography, (EBL), quantitative measurements of the beam current must be performed in order to know accurately the electron dose being applied to the specimen. A SEM sample holder with a built in Faraday cup was constructed as per previous work in EBL [21]. The design is presented in Figure 5-1. A small 2 mm hole was drilled into the aluminum and filled with a small amount of carbon paint. The carbon paint is a commercial product commonly used in SEM sample preparation to prevent charging. Over the top of this hole, a standard 3 mm TEM grid with an array of 40 micron squares was placed, and secured at the perimeter with a small amount of carbon paint around the edges as depicted in Figure 5-1. This fabrication process has been a standard method to create what is effectively a black hole from, which no electrons can escape. Since this process has worked so well in previous work [21], it was decided that a similar structured Faraday cup array would be an effective solution to act as an electron trap for the CMA. The goal was to come up with a way to create an array of Faraday cups inside the inner cylinder of the CMA, which would act as a very good SE absorber. That acts as a black hole, from which any electron that enters cannot escape.

The outer cylinders for a large commercial CMA are shown in Figure 5-2. The cylinder is made of pure Oxygen Free High temperature Copper, (OFH). This material has many desirable properties, in addition to being oxygen free to help prevent outgassing during high temperature operation. In addition, it is a good electrical and thermal conductor. One disadvantage of OFHC is that it emits a large amount of secondary electrons due to its relatively high atomic number, its high mass and its high electron density.

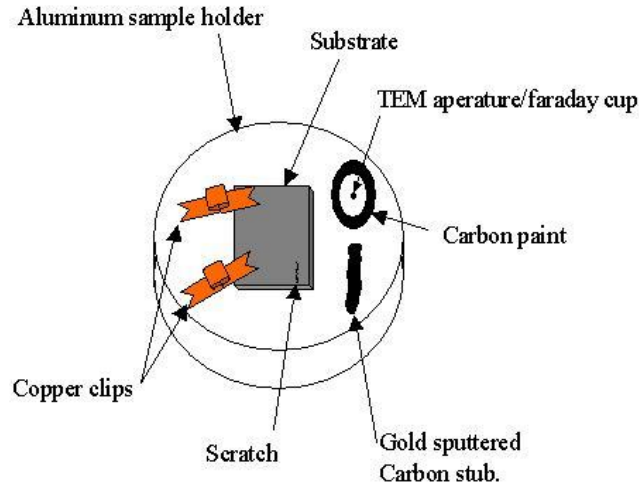


Figure 5-1: Sample holder with built in Faraday Cup for beam current measurements. The holder is a standard SEM aluminum sample mount modified to include a Faraday Cup to measure electron beam current.

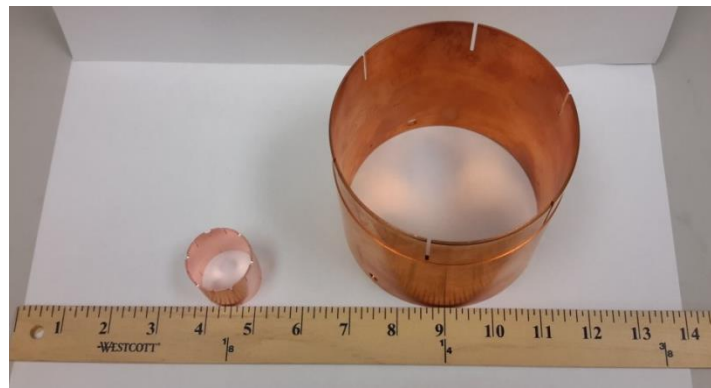


Figure 5-2: Photo comparison of outer cylinders from miniature and commercial CMA. The small cylinder on the left is the outer cylinder from the miniature CMA, with the large commercial outer cylinder shown on the right. Both cylinders are made from pure Oxygen Free High temperature Copper, (OFHC).

## 5.2. Scanning Electron Microscopy and SE Measurement on OFHC

### 5.2.1. Absorbed Current and Secondary Electron Detector

Absorbed current measurements were made with the Faraday Cup shown in Figure 5-1, [21], using a Keithly model 6485 pico-ammeter. The Keithly 6485 has a 15 femto-amp resolution and was connected in series with the sample stage of a model SU-70 High Resolution Scanning Electron Microscope, (HRSEM). The SU-70 Hitachi SEM beam conditions were: anode aperture four, objective aperture three, condenser

lens 16, and the Working Distance, (WD), was 7.2 mm. These settings resulted in a beam current of 21.3 pA at 3keV energy. In order to measure the relative SE emission, a SE output waveform method was adapted from a recent paper published by M. Postek at NIST [33]. The SEM was used to perform a line scan across the OFHC substrate, and across the edge of the un-milled and milled areas as depicted in Figure 5-3, which was laser machined to produce the FC array.

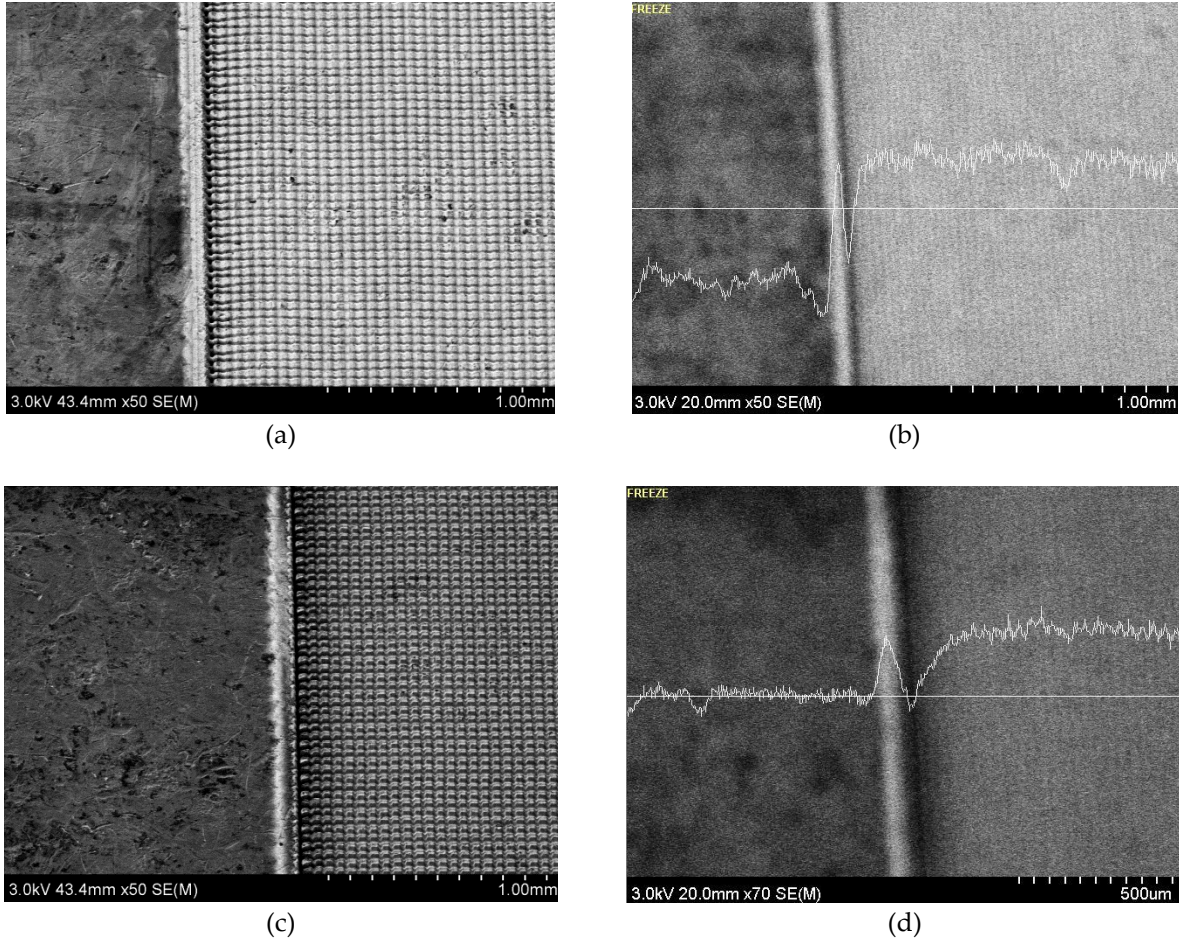
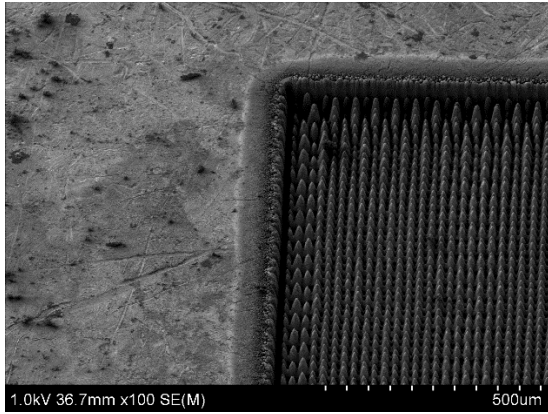


Figure 5-3: Secondary electron image and SE emission waveform overlay on laser milled OFHC. Laser machining was performed on OFHC copper gasket with 3 watts average power in a cross hatch pattern with a 50 x 50 micron spacing. Images (a)-(d) are secondary electron images and SE emission waveforms taken with a beam energy of 3 keV electrons. The solid white line shows the location of a line scan. The un-milled Cu is on the left. The SE output waveforms in (b) and (d) are 3 watts with 1 and 3 passes respectively, showing SE suppression.

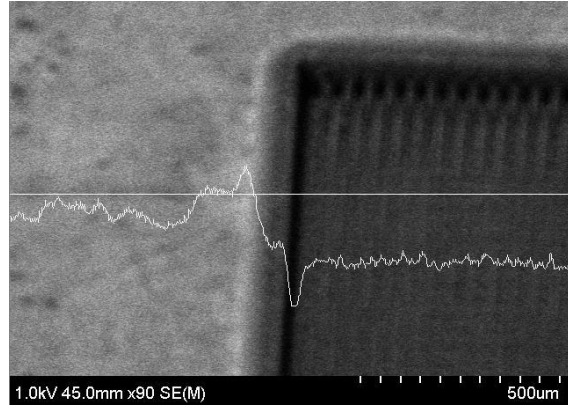
In order to simulate electrons striking the inside of the outer cylinder of the CMA, the OFHC substrate was mounted in the SEM tilted at 42.3 degrees to approximate the angle of attack of the electrons striking the inside of the outer cylinder. This is the angle as can be seen in the drawing of the CMA in

Figure 4-2 (a). A focused electron beam was first used to find the area of interest and collect an SEM image. Next, the beam was purposely defocused to simulate diffuse low current electrons as would be the case for electrons striking the outer cylinder. Figure 5-4 (a) shows a focused SEM image of a corner of the dark milled rectangle depicted in Figure 4-9. As can be observed, the laser milling produced a large number of needles in the Cu with deep void spaces between them, which act to absorb electrons. In Figure 5-4 (b), a second SEM picture was captured after the beam was defocused to the point where the LBM needles could no longer be resolved by the electron beam. This indicates that the beam diameter is larger than the needles and thus has the effect of lowering the electron current density impinging on the LBM structures. A line scan across the Cu and the FC array interface was performed and the SE output is displayed as a waveform superimposed on top of the image as shown in Figure 5-4. The beam was defocused in order to get a better average along the line scan of the SE emission. This was repeated at three commonly used beam energies used for Auger spectroscopy analysis in the CMA. Figure 5-4 (b), (c) and (d) show the SE emission waveforms for 1, 2, and 3 keV electrons respectively. As can be seen in these waveforms, the SE emission is significantly reduced when the electron beam enters the machined FC array. The SE suppression does not appear to depend on beam energy. For all 3 energies, the relative SE drop is approximately the same compared to the un-milled copper. The lowest SE emission, which produces brightness on these waveforms, occurs at the edge of the FC array. It is at the edge where the laser beam has the longest residence time as it performs the zig-zag vector scan. The laser scans a short distance to move to the next scan line and results in the edges receiving a larger laser residence time. This creates a deeper crevice, which is approximately 200 microns deep, as shown in Figure 4-10. Figure 4-10 shows a side view of the edge of the FC array rectangle. It appears from the results displayed in Figure 5-4 that at beam energies between 1 and 3 keV, which is the range used in the CMA, there is little change in the ability of the FC array to suppress SE emission.

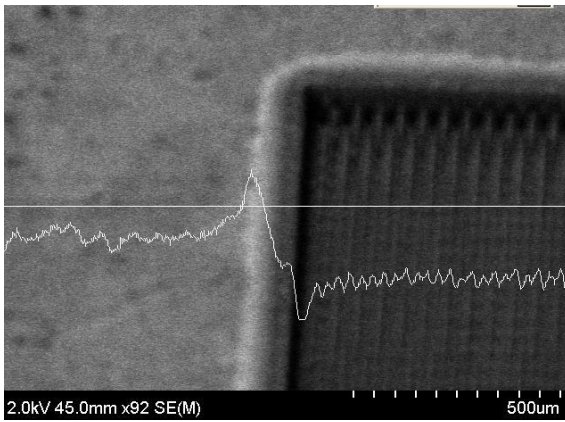




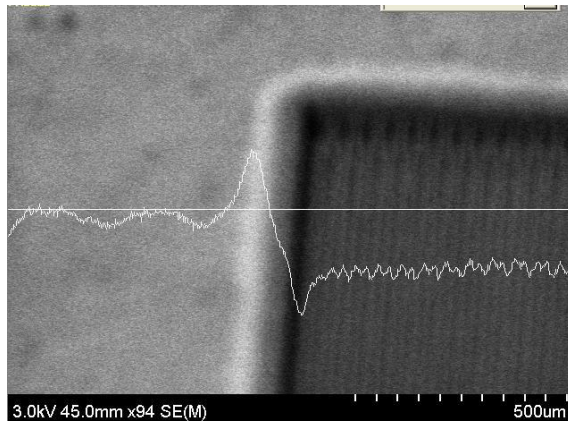
(a)



(b)



(c)



(d)

Figure 5-4: Secondary electron image and SE emission waveform overlay on laser milled OFHC. Laser machining was performed on OFHC copper gasket with 3 watts average power in a cross hatch pattern with a 25 x 25 micron spacing. Images (b)-(d) are secondary electron images taken with a beam energy of 1, 2, and 3 keV electrons. The solid white line shows the location of a line scan. The un-milled Cu is on the left. Showing the large decrease in SE emission in the laser milled region.

## CHAPTER 6: CONCLUSIONS, FUTURE WORK AND FINAL INSPIRATION

### 6.1. Conclusions

The background theory of AES has been presented. AES is a useful tool for metrology, and characterization of thin film and nanostructured devices. This research presents the design of a miniaturized CMA AES spectrometer, which was simulated using the FEM modeling and CAD design software COMSOL. The CMA design includes a miniature tungsten filament thermionic electron source, which is mounted in the center of the inner cylinder of the CMA. A focused beam of electrons, which originates from the center of the CMA electron source excite Auger electron emission from the surface of a sample of unknown elemental composition. These Auger electrons along with in-elastically scattered BSE are emitted from the sample surface in all directions. The CMA is placed close to the sample in order electrons to pass into an entrance aperture after that they undergo spectroscopic energy analysis.

After attaining the numerical solution for the electric potential from the COMSOL solution, the equation of motion for a charged particle, i.e.  $QE=ma$ , was used to successfully plot the electron trajectory of electrons emitted from a simulated target sample placed at the entrance aperture of the spectrometer. The numerical solution of the electron trajectory from COMSOL was compared to the analytical solution for a parallel plate capacitor with the same geometry, boundary conditions, and input electron velocity vector which showed good agreement.

Auger electrons with the correct pass energy encounter the negative electric potential placed on the outer cylinder of the spectrometer. These electrons are able to fly through the spectrometer to be counted as an electron with a unique signature energy, which can be used to determine the elemental composition of the sample. The scale of the analysis can be in the nanometer to sub-nanometer range

depending on the size, structure, and composition of the sample and the experimental conditions required to interrogate the sample.

Due to the large noise background in the Auger spectrum, several experimental methods were proposed, and used to attempt to lower the secondary electron noise. The secondary noise is generated in the CMA due to unwanted inelastic BSE electrons, which enter the spectrometer along with the signature Auger electrons. Both the inner and outer cylindrical electrodes were identified as the source of secondary electron noise in the spectrometer. The cylinders are made from pure Oxygen Free High Temperature Copper, (OFHC). Attempts to use low secondary emission coatings on the copper showed promise since they successfully lowered the SE emission. However, these films were prone to delamination and flaking of the films. Also, all materials and structures in the CMA must be able to withstand a bake up to 200 degrees Celsius in order to attain UHV in the spectrometer. This would likely be detrimental, and may cause the films to delaminate from the copper unless a better thin film deposition conditions and adhesion layers can be found, which would resist delamination upon baking. Laser machining of OFHC substrates was shown to be the best method to lower SE emission of the copper compared to untreated bare OFHC copper. Results from SE emission studies in the SEM show a marked decrease in laser machined OFHC copper substrates compared to untreated substrates. These SE emission experiments were performed on OFHC substrates using the same energy up to 3kV, and entrance angle of 42.3 degrees, since electrons would encounter as they enter the entrance aperture of the CMA. The laser machining in effect creates thousands of micron size Faraday Cups, which effectively absorb electrons. The next step is to program a laser milling process to mill Faraday Cup arrays on the inside of the CMA outer cylinder.

This design and spectrometer simulations performed in this research assisted in the development of a commercially available Auger spectrometer package. Figure 6-1 shows the miniature CMA built at RBD instruments Inc. in Bend Oregon, which is now commercial product, and sold under the microCMA trade name [2]. It operates with a power supply and USB interface and computer software with a graphical

user interface for data collection. The microCMA is a non-scanning, (imaging), cylindrical mirror analyzer designed for the many applications for AES that do not require scanning, (imaging), capability. The compact design allows the spectrometer to be mounted on a standard 2 ¾ inch UHV conflat flange.

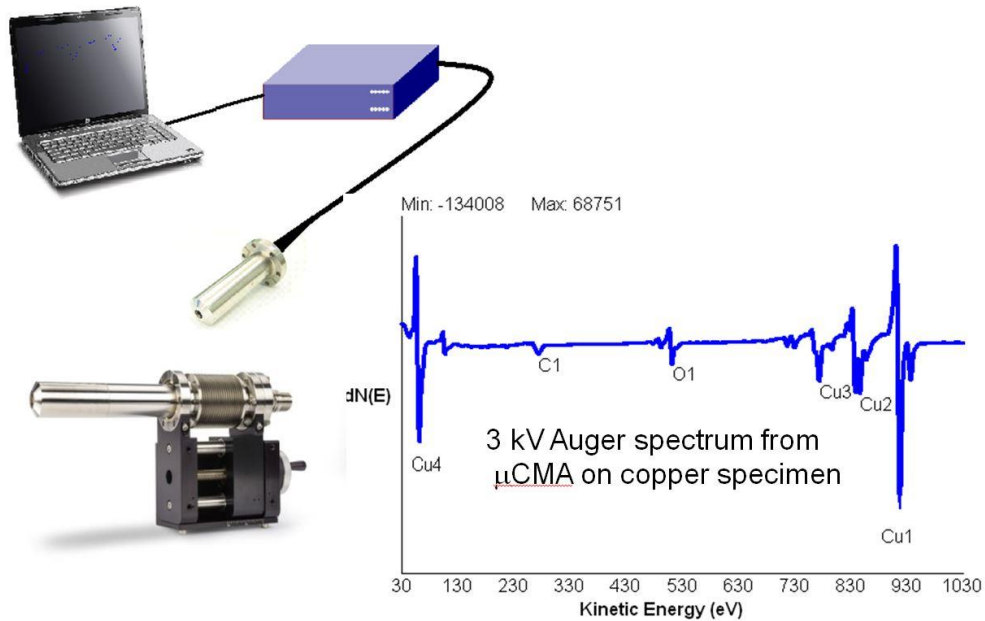


Figure 6-1: Commercial microCMA from RBD Instruments Inc.

The spectrometer mounts on a standard 2 ¾ inch UHV conflat flange and is available with a bellows for adjustable working distance. The data shown is an Auger spectrum from a copper specimen excited with a beam voltage of 3kV.

## 6.2. Future Work

- To optimize the electron suppression FC arrays on OFHC substrates.
- Develop a process to laser machine the FC suppressor array on the curved inner cylinder and outer cylinder of the CMA analyzer.
- Place the Laser machine cylinders in the manufactured CMA to test for spectrometer performance in terms of the reduction of signal to noise ratio in the Auger spectrometer spectra.

## 6.3. Final Inspiration

J.J. Thompson in his notes on Recent Researches in Electricity and Magnetism, in 1893, a full four years before his discovery of the electron 1897-1899, wrote: “The Phenomena attending the electric

discharge through gases are so beautiful and varied that they have attracted the attention of numerous observers. The attention given to these phenomena is not, however, due so much to the beauty of the experiments, as to the widespread conviction that there is perhaps no other branch of physics which affords us so promising an opportunity of penetrating the secret of electricity, for while the passage of this agent through a metal or an electrolyte is invisible, that through a gas is accompanied by the most brilliant luminous effects, which in many cases are so much influenced by changes in the conditions of the discharge as to give us many opportunities of testing any view we make take of the nature of electricity, of the electric discharge, and of the relation between electricity and matter" [34].

## REFERENCES

- [1] M. Hocella and A. H. Carim, "A Reassessment of Electron Escape Depths in Silicon and Thermally Grown Oxide Thin Films," *Surface Science*, vol. 197, pp. 260-268, 1988.
- [2] R. Dellwo, "microCMA Compact Auger Analyzer," RBD Instruments Incorporated, [Online]. Available: <https://rbdinstruments.com/products/micro-cma.html>. [Accessed 25 October 2017].
- [3] J. Bieber, "Nanostructured and Microstructured Extremely High Surface Area (EHSA) Materials for Absorption of Charged Particles and Electromagnetic Waves". USA Patent Provisional Patent 62/578881, 31 October 2017.
- [4] O. H. Duparc, "Pierre Auger – Lise Meitner: Comparative Contributions to the Auger Effect," *International Journal of Materials Research*, vol. 100, no. 9, pp. 1162-1166, 2009.
- [5] A. Carson, "Auger Electron Emission," 15 October 2007. [Online]. Available: [https://commons.wikimedia.org/wiki/File:Auger\\_Process.svg](https://commons.wikimedia.org/wiki/File:Auger_Process.svg). [Accessed 23 October 2017].
- [6] Toshiyouri, "Auger Electron Spectroscopy," 1 April 2015. [Online]. Available: [https://commons.wikimedia.org/wiki/File:Auger\\_xray\\_wiki\\_in\\_png\\_format.png](https://commons.wikimedia.org/wiki/File:Auger_xray_wiki_in_png_format.png). [Accessed 23 October 2017].
- [7] M. F. Hochella, D. W. Harris and A. M. Turner, "Scanning Auger Microscopy as a High-resolution Microprobe for Geologic Materials," *American Mineralogist*, vol. 71, pp. 1247-1257, 1986.
- [8] C. Evans, "AUGER TUTORIAL: THEORY," [Online]. Available: <https://www.eag.com/auger-tutorial-theory/>. [Accessed 23 October 2017].
- [9] A. Carson, "Auger Electron Spectroscopy," 16 October 2007. [Online]. Available: [https://commons.wikimedia.org/wiki/File:AES\\_Setup2.JPG](https://commons.wikimedia.org/wiki/File:AES_Setup2.JPG). [Accessed 23 October 2017].
- [10] D. Roy and D. Trembley, "Design of Electron Spectrometers," *Rep. Prog. Phys.*, vol. 53, pp. 1621-1674, 1990.
- [11] A. Savitzky and M.J.E. Golay, "Smoothing and Differentiation of Data by Simplified Least-squares Procedures,," *Anal. Chem.*, vol. 36, no. 8, pp. 1627-1639, 1964.
- [12] Physical Electronics, "Auger Electron Spectroscopy," [Online]. Available: <http://www.phis.com/surface-analysis-techniques/aes.html>. [Accessed 23 October 2017].
- [13] C. Evans, "Auger Electron Spectroscopy," Charles Evans & Associates, [Online]. Available: <https://www.eag.com/auger-electron-spectroscopy/>. [Accessed 24 October 2017].


- [14] J. Uritsky, "Tungsten Etch Back Process," *Vac. Sci. Tech.*, vol. 15, no. 3, pp. 1319-1327, 1997.
- [15] J. W. Nowok, J. P. Hurley and J. A. Bieber, "Temperature in Multicomponent Aluminosilicates Derived from Coal-ash Slags," *Journal of Materials Science*, vol. 30, pp. 361-364, 1995.
- [16] R. H. Fowler and L. W. Nordheim, "Electron Emission in Intense Electric Fields," *Proc. R. Soc., London A*, vol. 119, pp. 173-192, 1928.
- [17] J. Goldstein, D. Newbury, P. Echlin, D. Joy, et al., *Scanning Electron Microscopy and X-ray Microanalysis*, Springer, 1992.
- [18] M. McCord and M.J. Rooks, *Handbook of Microlithography, Micromachining and Microfabrication*, Bellingham: The International Society for Optical Engineering, 1997.
- [19] J. Bieber, J. Pulecio and W. Moreno, "Applications of Electron Beam Induced Deposition in Nanofabrication," in *IEEE 7th International Caribbean Conference on Devices, Circuits and Systems*, Cancun, 2008.
- [20] A. Broers and W. Molzen, "Electron-beam Formation of 80 Å Metal Structures," *Applied Physics Letters*, vol. 29, p. 596, 1976.
- [21] J. Bieber, S. Sadow and W. Moreno, "Synthesis of Nanoscale Structures in Single Crystal Silicon Carbide by Electron Beam Lithography," in *IEEE International Caracas Conference on Devices, Circuits and Systems*, 2004.
- [22] H. W. P. Koops, "Gas-assisted Focused Electron Beam and Ion Beam Processing and Fabrication," *J. Vac. Sci. Technol. B.*, vol. 6, p. 477, 1988.
- [23] J. C. Vickerman and I. Gilmore, *Surface Analysis: The Principal Techniques*, Wiley, 2009.
- [24] D. Save, A. F. Braud, J. Torres and et al., "Electromigration Resistance of Copper Interconnects," *Microelectronic Engineering*, vol. 33, pp. 75-84, 1997.
- [25] P. W. Palmberg, "A combined ESCA and Auger spectrometer," *J. Vac. Sci. Tech.*, vol. 12, pp. 379-384, 1975.
- [26] M. M. E. Gomati and T. A. E. Bakush, "Sources of Internal Scattering of Electrons in a Cylindrical Mirror Analyzer," *Surface and Interface Analysis*, vol. 24, pp. 152-162, 1996.
- [27] T. E. Bakush and M. E. Gomati, "Internal Scattering in a Single Pass Cylindrical Mirror Analyser," *Journal of Electron Spectroscopy and Related Phenomena*, vol. 74, pp. 109-120, 1995.
- [28] J. Goldstein, et al., *Scanning Electron Microscopy and X-ray Microanalysis*, New York: Plenum Press, 1981.
- [29] W. KUO, M. Briceno and D. OZKAYA, "Characterisation of Catalysts Using Secondary and Backscatter In Lens Detectors," *Platinum Metals Rev.*, vol. 58, no. 2, pp. 106-110, 2014.

- [30] I. Langmuir, "The Arrangement of Electrons in Atoms and Molecules," American Chemical Society, vol. 41, pp. 868-934, 1919.
- [31] D. Shin, S. Yoo, H. Song, H. Tak and D. Byun, "Electrostatic - Force - Assisted Dispensing Printing to Construct High - Aspect - Ratio of 0.79 Electrodes on a Textured Surface with Improved Adhesion and Contact Resistivity," Scientific Reports, vol. 5, p. 16704, 11/18/online 2015.
- [32] E. A. Rojas - Nastrucci, "High Performance Digitally Manufactured Microwave and Millimeter - Wave Circuits and Antennas," University of South Florida, Tampa, 2017.
- [33] T. Postek, A. E. Vladár, J. S. Villarrubia and A. Muto, "Comparison of Electron Imaging Modes for Dimensional Measurements in the Scanning Electron Microscope," Microscopy and Microanalysis, vol. 4, pp. 768-777, 2016.
- [34] J. J. Thomson, Notes on Recent Researches in Electricity and Magnetism, Oxford: Oxford, 1893.




## APPENDIX A: COPYRIGHT PERMISSIONS

Below is copyright permission for Figure 2-1.

<b>Description</b>	<p><b>Creator:</b> Briggs, C.A</p> <p><b>Subject:</b> Meitner, Lise 1878-1968 Catholic University of America</p> <p><b>Type:</b> Black-and-white photographs</p> <p><b>Date:</b> 1946</p> <p><b>Topic:</b> Physics Women scientists</p> <p><b>Local number:</b> SIA Acc. 90-105 [SIA2008-5996]</p> <p><b>Summary:</b> In 1938, Austrian-born physicist Lise Meitner (1878-1968) fled Germany and eventually became a Swedish citizen. After World War II, Meitner received many awards, including being named "Woman of the Year" at the National Press Club in 1946. She was a Visiting Professor of Physics at Catholic University during Spring 1946. In a press release associated with her arrival, Dr. Meitner emphasized that her goal was "wholly educational": "I have no intention to suggest how atomic energy should be controlled, beyond expressing my sincere hope that no occasion will again arise where it will be utilized in war. A lasting peace is more desirable than the creation of weapons which might lead to the extermination of mankind."</p> <p><b>Cite as:</b> Acc. 90-105 - Science Service, Records, 1920s-1970s, Smithsonian Institution Archives</p> <p><b>Persistent URL:</b> [1]</p> <p><b>Repository:</b> Smithsonian Institution Archives</p>
<b>Date</b>	1 March 2010, 11:58:20
<b>Source</b>	Flickr: Lise Meitner (1878-1968), lecturing at Catholic University, Washington, D.C., 1946
<b>Author</b>	Smithsonian Institution
<b>Permission (Reusing this file)</b>	 This image, which was originally posted to Flickr, was uploaded to Commons using Flickr upload bot on 04:36, 15 February 2012 (UTC) by <b>MaterialsScientist</b> . On that date it was tagged as <i>no known copyright restrictions</i> .

Below is copyright permission for Figure 2-2.

<b>Description</b>	This is a series of schematic drawings of the Auger effect. Panel (a) provides a sequential view of Auger transitions in terms of atomic orbital energy (increasing radially) while panel (b) provides the same information in condensed format using spectroscopic notation.
<b>Date</b>	15 October 2007
<b>Source</b>	Own work
<b>Author</b>	A. Carlson
<b>Permission (Reusing this file)</b>	 I, the copyright holder of this work, release this work into the <b>public domain</b> . This applies worldwide. In some countries this may not be legally possible; if so: <i>I grant anyone the right to use this work for any purpose, without any conditions, unless such conditions are required by law.</i>

Below is copyright permission for Figure 2-3.

This is a file from the Wikimedia Commons. Information from its [description page](#) there is shown below.  
Commons is a freely licensed media file repository. You can help.

**Summary** [\[edit\]](#)

<b>Description</b>	English: Fluorescence and Auger electron yields as a function of atomic number for K shell vacancies. Auger transitions (red curve) are more probable for lighter elements, while X-ray yield (dotted blue curve) becomes dominant at higher atomic numbers. Similar plots can be obtained for L and M shell transitions. Coster – Kronig (i.e. intra-shell) transitions are ignored in this analysis.
<b>Date</b>	1 April 2015
<b>Source</b>	Own work
<b>Author</b>	Toshiyouri

**Licensing** [\[edit\]](#)

I, the copyright holder of this work, hereby publish it under the following license:


This file is licensed under the Creative Commons Attribution-Share Alike 4.0 International license.

You are free:


- **to share** – to copy, distribute and transmit the work
- **to remix** – to adapt the work

Under the following conditions:

- **attribution** – You must attribute the work in the manner specified by the author or licensor (but not in any way that suggests that they endorse you or your use of the work).
- **share alike** – If you alter, transform, or build upon this work, you may distribute the resulting work only under the same or similar license to this one.



Below is copyright permission for Figure 2-4.



**MINERALOGICAL SOCIETY OF AMERICA**  
3635 Concorde Pkwy Ste 500 • Chantilly VA 20151-1110 • USA  
Tel: 1 (703) 652-9950 • Fax: 1 (703) 652-9951 • Internet: [www.minsocam.org](http://www.minsocam.org)

November 12, 2017

Mr. Jay A Bieber  
University of South Florida  
4202 E Fowler Ave  
Tampa Florida 33617  
United States

Email: [bieber@usf.edu](mailto:bieber@usf.edu)

Dear Mr. Bieber:

I received your e-mail message of 2017-11-12 requesting permission to reproduce the following figure in your thesis, *Design and Simulation of a Miniature Cylindrical Mirror Auger Electron Energy Analyzer with Secondary Electron Noise Suppression*, for the University of South Florida:

- Figure Number(s): 1 from Michael F. Hochella, David W. Harris, Arthur M. Turner (1986) Scanning Auger microscopy as a high-resolution microprobe for geologic materials, *American Mineralogist*, v. 71, i. 9-10, p. 1247-1257.

It is with pleasure that we grant you permission to reproduce this figure without cost in this and all subsequent editions of the work, its ancillaries, advertisements and promotional materials, and other derivative works, in any form or medium, whether now known or hereafter developed, in all languages, for distribution throughout the world on the conditions that reference is given to the original publication of the Mineralogical Society of America.

Sincerely,

*J. Alex Speer*

J. Alexander Speer  
Executive Director, MSA

Below is copyright permission for Figure 2-5.

**Fw: Jay Bieber**  
John Newman <JNewman@phi.com >  
Sent: Mon 11/13/2017 11:44  
To: Bieber, Jay

---

Hi Jay,

Please feel free to use the PHI diagrams in your dissertation. All we ask is that recognition be given to Physical Electronics for the graphs.

Best regards,

John

John Newman  
Director of Analytical Laboratory  
Physical Electronics, USA  
18725 Lake Drive East  
Chanhassen, MN 55317

952-828-6409  
[jnewman@phi.com](mailto:jnewman@phi.com)  
[www.phi.com](http://www.phi.com)

Below is copyright permission for Figure 2-6.

 This is a file from the Wikimedia Commons. Information from its [description page there](#) is shown below.  
Commons is a freely licensed media file repository. You can help.

Summary [\[edit\]](#)

Description	Auger electron spectroscopy experimental setup.
Date	16 October 2007
Source	Own work
Author	Acarfso3

Below is copyright permission for Figure 2-9.

**Fw: Jay Bieber**  
 John Newman <JNewman@phi.com>  
 Sent: Mon 11/13/2017 11:44  
 To: Bieber, Jay

---

Hi Jay,

Please feel free to use the PHI diagrams in your dissertation. All we ask is that recognition be given to Physical Electronics for the graphs.

Best regards,

John

John Newman  
 Director of Analytical Laboratory  
 Physical Electronics, USA  
 18725 Lake Drive East  
 Chanhassen, MN 55317

952-828-6409  
[jnewman@phi.com](mailto:jnewman@phi.com)  
[www.phi.com](http://www.phi.com)

Below is copyright permission for Figure 2-11.

<b>AIP PUBLISHING LLC LICENSE TERMS AND CONDITIONS</b>	
	Nov 13, 2017
<hr/>	
This Agreement between University of South Florida -- Jay Bieber ("You") and AIP Publishing LLC ("AIP Publishing LLC") consists of your license details and the terms and conditions provided by AIP Publishing LLC and Copyright Clearance Center.	
License Number	4226881156405
License date	Nov 13, 2017
Licensed Content Publisher	AIP Publishing LLC
Licensed Content Publication	Journal of Vacuum Science & Technology A
Licensed Content Title	Root cause determination of particle contamination in the tungsten etch back process
Licensed Content Author	Y. Uritsky, L. Chen, S. Zhang, et al
Licensed Content Date	May 1, 1997
Licensed Content Volume	15
Licensed Content Issue	3
Type of Use	Thesis/Dissertation
Requestor type	Student
Format	Electronic
Portion	Figure/Table
Number of figures/tables	2
Title of your thesis / dissertation	Design and Simulation of a Miniature Cylindrical Mirror Auger Electron Energy Analyzer with Secondary Electron Noise Suppression
Expected completion date	Dec 2017
Estimated size (number of pages)	100
Requestor Location	University of South Florida 4202 E Fowler Ave.  TAMPA, FL 33617 United States Attn: University of South Florida
Billing Type	Invoice
Billing Address	University of South Florida 4202 E Fowler Ave.  TAMPA, FL 33617 United States Attn: University of South Florida
Total	0.00 USD

Below is copyright permission for Figure 2-12.

<b>AIP PUBLISHING LLC LICENSE TERMS AND CONDITIONS</b>	
Nov 13, 2017	
<hr/> <p>This Agreement between University of South Florida -- Jay Bieber ("You") and AIP Publishing LLC ("AIP Publishing LLC") consists of your license details and the terms and conditions provided by AIP Publishing LLC and Copyright Clearance Center.</p>	
License Number	4226881156405
License date	Nov 13, 2017
Licensed Content Publisher	AIP Publishing LLC
Licensed Content Publication	Journal of Vacuum Science & Technology A
Licensed Content Title	Root cause determination of particle contamination in the tungsten etch back process
Licensed Content Author	Y. Uritsky, L. Chen, S. Zhang, et al
Licensed Content Date	May 1, 1997
Licensed Content Volume	15
Licensed Content Issue	3
Type of Use	Thesis/Dissertation
Requestor type	Student
Format	Electronic
Portion	Figure/Table
Number of figures/tables	2
Title of your thesis / dissertation	Design and Simulation of a Miniature Cylindrical Mirror Auger Electron Energy Analyzer with Secondary Electron Noise Suppression
Expected completion date	Dec 2017
Estimated size (number of pages)	100
Requestor Location	University of South Florida 4202 E Fowler Ave.  TAMPA, FL 33617 United States Attn: University of South Florida
Billing Type	Invoice
Billing Address	University of South Florida 4202 E Fowler Ave.  TAMPA, FL 33617 United States Attn: University of South Florida
Total	0.00 USD

Below is copyright permission for Figure 4-1.

<b>JOHN WILEY AND SONS LICENSE TERMS AND CONDITIONS</b>	
Nov 12, 2017	
<hr/> <p>This Agreement between University of South Florida -- Jay Bieber ("You") and John Wiley and Sons ("John Wiley and Sons") consists of your license details and the terms and conditions provided by John Wiley and Sons and Copyright Clearance Center.</p>	
License Number	4226761381295
License date	Nov 12, 2017
Licensed Content Publisher	John Wiley and Sons
Licensed Content Publication	Wiley oBooks
Licensed Content Title	Auger Electron Spectroscopy
Licensed Content Author	Hans Jörg Mathieu
Licensed Content Date	Mar 27, 2009
Licensed Content Pages	37
Type of use	Dissertation/Thesis
Requestor type	University/Academic
Format	Electronic
Portion	Figure/table
Number of figures/tables	1
Original Wiley figure/table number(s)	Figure 2.21
Will you be translating?	No
Title of your thesis / dissertation	Design and Simulation of a Miniature Cylindrical Mirror Auger Electron Energy Analyzer with Secondary Electron Noise Suppression
Expected completion date	Dec 2017
Expected size (number of pages)	100
Requestor Location	University of South Florida 4202 E Fowler Ave.  TAMPA, FL 33617 United States Attn: University of South Florida
Publisher Tax ID	EU826007151
Billing Type	Invoice
Billing Address	University of South Florida 4202 E Fowler Ave.  TAMPA, FL 33617 United States Attn: University of South Florida

Below is copyright permission for Figure 4-2 (a).

<b>ELSEVIER LICENSE TERMS AND CONDITIONS</b>		Nov 12, 2017
<hr/>		
<p>This Agreement between University of South Florida -- Jay Bieber ("You") and Elsevier ("Elsevier") consists of your license details and the terms and conditions provided by Elsevier and Copyright Clearance Center.</p>		
License Number	4226770953117	
License date	Nov 12, 2017	
Licensed Content Publisher	Elsevier	
Licensed Content Publication	Journal of Electron Spectroscopy and Related Phenomena	
Licensed Content Title	Internal scattering in a single pass cylindrical mirror analyses	
Licensed Content Author	T.A. El Bakush, M.M. El Gomati	
Licensed Content Date	Oct 31, 1995	
Licensed Content Volume	74	
Licensed Content Issue	2	
Licensed Content Pages	12	
Start Page	109	
End Page	120	
Type of Use	reuse in a thesis/dissertation	
Intended publisher of new work	other	
Portion	figures/tables/illustrations	
Number of figures/tables/illustrations	2	
Format	electronic	
Are you the author of this Elsevier article?	No	
Will you be translating?	No	
Original figure numbers	Figure 1 and Figure 2	
Title of your thesis/dissertation	Design and Simulation of a Miniature Cylindrical Mirror Auger Electron Energy Analyzer with Secondary Electron Noise Suppression	
Expected completion date	Dec 2017	
Estimated size (number of pages)	100	
Requestor Location	University of South Florida 4202 E Fowler Ave.  TAMPA, FL 33617 United States Attn: University of South Florida	
Publisher Tax ID	98-0397604	

Below is copyright permission for Figure 4-2 (b).


<b>JOHN WILEY AND SONS LICENSE TERMS AND CONDITIONS</b>	
Nov 12, 2017	
<hr/> <hr/>	
<p>This Agreement between University of South Florida -- Jay Bieber ("You") and John Wiley and Sons ("John Wiley and Sons") consists of your license details and the terms and conditions provided by John Wiley and Sons and Copyright Clearance Center.</p>	
License Number	4226781136264
License date	Nov 12, 2017
Licensed Content Publisher	John Wiley and Sons
Licensed Content Publication	Surface & Interface Analysis
Licensed Content Title	Sources of Internal Scattering of Electrons in a Cylindrical Mirror Analyser (CMA)
Licensed Content Author	M. M. El Gomati, T. A. El Bakush
Licensed Content Date	Mar 1, 1996
Licensed Content Pages	11
Type of use	Dissertation/Thesis
Requestor type	University/Academic
Format	Electronic
Portion	Figure/table
Number of figures/tables	2
Original Wiley figure/table number(s)	Figure 2 and Figure 4
Will you be translating?	No
Title of your thesis / dissertation	Design and Simulation of a Miniature Cylindrical Mirror Auger Electron Energy Analyzer with Secondary Electron Noise Suppression
Expected completion date	Dec 2017
Expected size (number of pages)	100
Requestor Location	University of South Florida 4202 E Fowler Ave.  TAMPA, FL 33617 United States Attn: University of South Florida
Publisher Tax ID	EU826007151
Billing Type	Invoice
Billing Address	University of South Florida 4202 E Fowler Ave.  TAMPA, FL 33617 United States Attn: University of South Florida



Below is copyright permission for Figure 4-4.

## Open Access Policy


The *Johnson Matthey Technology Review* is a **Platinum Open Access journal** and the content is licensed under **Creative Commons**. Find out more using the information and links below



Platinum Open Access

All content is freely available without charge to the user or his/her institution. Users are allowed to read, download, copy, distribute, print, search, or link to the full texts of the articles, or use them for any other lawful purpose, without asking prior permission from the publisher or the author. This is in accordance with the Budapest Open Access Initiative (BOAI) definition of Open Access.

### Creative Commons License



This work is licensed under a Creative Commons Attribution-NonCommercial-NoDerivatives 4.0 International License.

You may share, copy and redistribute the material in any medium or format for any lawful purpose. You must give appropriate credit to the author and publisher. You may not use the material for commercial purposes without prior permission. You may not distribute modified material without prior permission.

The rights of users under exceptions and limitations, such as fair use and fair dealing, are not affected by the CC licenses.

### Funding Statement

Publishing in *Johnson Matthey Technology Review* is free of charge. There are no author fees. All services including peer review, copyediting, typesetting, production of web pages and reproduction of colour images are included.

The journal is free of charge to access, read and download.

All costs associated with publishing and hosting this journal are funded by Johnson Matthey Plc as part of its investment in global research and development.

Below is copyright permission for Figure 4-5.

<b>ELSEVIER LICENSE TERMS AND CONDITIONS</b>	
Nov 12, 2017	
<hr/> <hr/>	
<b>This Agreement between University of South Florida -- Jay Bieber ("You") and Elsevier ("Elsevier") consists of your license details and the terms and conditions provided by Elsevier and Copyright Clearance Center.</b>	
License Number	4226770953117
License date	Nov 12, 2017
Licensed Content Publisher	Elsevier
Licensed Content Publication	Journal of Electron Spectroscopy and Related Phenomena
Licensed Content Title	Internal scattering in a single pass cylindrical mirror analyses
Licensed Content Author	T.A. El Bakush,M.M. El Gomati
Licensed Content Date	Oct 31, 1995
Licensed Content Volume	74
Licensed Content Issue	2
Licensed Content Pages	12
Start Page	109
End Page	120
Type of Use	reuse in a thesis/dissertation
Intended publisher of new work	other
Portion	figures/tables/illustrations
Number of figures/tables/illustrations	2
Format	electronic
Are you the author of this Elsevier article?	No
Will you be translating?	No
Original figure numbers	Figure 1 and Figure 2
Title of your thesis/dissertation	Design and Simulation of a Miniature Cylindrical Mirror Auger Electron Energy Analyzer with Secondary Electron Noise Suppression
Expected completion date	Dec 2017
Estimated size (number of pages)	100
Requestor Location	University of South Florida 4202 E Fowler Ave.  TAMPA, FL 33617 United States Attn: University of South Florida
Publisher Tax ID	98-0397604

Below is copyright permission for Table 4-5.

<b>ELSEVIER LICENSE TERMS AND CONDITIONS</b>	
	Nov 12, 2017
<hr/>	
<p>This Agreement between University of South Florida -- Jay Bieber ("You") and Elsevier ("Elsevier") consists of your license details and the terms and conditions provided by Elsevier and Copyright Clearance Center.</p>	
License Number	4226820466503
License date	Nov 12, 2017
Licensed Content Publisher	Elsevier
Licensed Content Publication	Journal of Electron Spectroscopy and Related Phenomena
Licensed Content Title	Internal scattering in a single pass cylindrical mirror analyses
Licensed Content Author	T.A. El Bakush, M.M. El Gomati
Licensed Content Date	Oct 31, 1995
Licensed Content Volume	74
Licensed Content Issue	2
Licensed Content Pages	12
Start Page	109
End Page	120
Type of Use	reuse in a thesis/dissertation
Portion	figures/tables/illustrations
Number of figures/tables/illustrations	1
Format	electronic
Are you the author of this Elsevier article?	No
Will you be translating?	No
Original figure numbers	Table 1
Title of your thesis/dissertation	Design and Simulation of a Miniature Cylindrical Mirror Auger Electron Energy Analyzer with Secondary Electron Noise Suppression
Expected completion date	Dec 2017
Estimated size (number of pages)	100
Requestor Location	University of South Florida 4202 E Fowler Ave.  TAMPA, FL 33617 United States Attn: University of South Florida
Publisher Tax ID	98-0397604


Below is copyright permission for Figure 4-6.

**Summary** [ edit ]

<b>Description:</b>	English: This image depicts an electron beam deposition scheme where there is no direct line of sight from the filament to the deposition material.
<b>Date:</b>	16 July 2012
<b>Source:</b>	Power Point
<b>Author:</b>	Jatossado

**Licensing** [ edit ]

I, the copyright holder of this work, hereby publish it under the following licenses:

 Permission is granted to copy, distribute and/or modify this document under the terms of the [GNU Free Documentation License](#), Version 1.2 or any later version published by the Free Software Foundation, with no Invariant Sections, no Front-Cover Texts, and no Back-Cover Texts. A copy of the license is included in the section entitled *GNU Free Documentation License*.

This file is licensed under the [Creative Commons Attribution-Share Alike 3.0 Unported](#) license.


You are free:

- **to share** – to copy, distribute and transmit the work
- **to remix** – to adapt the work

Under the following conditions:

- **attribution** – You must attribute the work in the manner specified by the author or licensor (but not in any way that suggests that they endorse you or your use of the work).
- **share alike** – If you alter, transform, or build upon this work, you may distribute the resulting work only under the same or similar license to this one.

*You may select the license of your choice.*




## Attribution-ShareAlike 3.0 Unported (CC BY-SA 3.0)

This is a human-readable summary of (and not a substitute for) the [license](#). [Disclaimer](#).



### You are free to:

- Share** — copy and redistribute the material in any medium or format
- Adapt** — remix, transform, and build upon the material for any purpose, even commercially.

The licensor cannot revoke these freedoms as long as you follow the license terms.



### Under the following terms:

-  **Attribution** — You must give [appropriate credit](#), provide a link to the license, and [indicate if changes were made](#). You may do so in any reasonable manner, but not in any way that suggests the licensor endorses you or your use.
-  **ShareAlike** — If you remix, transform, or build upon the material, you must distribute your contributions under the [same license](#) as the original.

**No additional restrictions** — You may not apply legal terms or [technological measures](#) that legally restrict others from doing anything the license permits.


### Notices:

You do not have to comply with the license forelements of the material in the public domain or where your use is permitted by an applicable [exception or limitation](#).

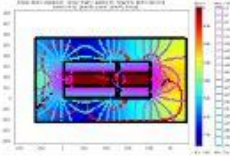
No warranties are given. The license may not give you all of the permissions necessary for your intended use. For example, other rights such as [publicity, privacy, or moral rights](#) may limit how you use the material.

## APPENDIX B: COMSOL SOLUTION HTML OUTPUT

### B.1. Double Pass CMA



COMSOL Model Report



**1. Table of Contents**

- Title - COMSOL Model Report
- Table of Contents
- Model Properties
- Constants
- Geometry
- Geom1
- Geom2
- Materials/Coefficients Library
- Solver Settings
- Postprocessing
- Variables

**2. Model Properties**

Property	Value
Model name	
Author	
Company	
Department	
Reference	
URL	
Saved date	Nov 25, 2008 12:08:19 PM
Creation date	Nov 12, 2008 3:56:51 PM
COMSOL version	COMSOL 3.3.0.511

File name: C:\COMSOL33a\From Rons 11 19 08 drawing with elements.mph

Application modes and modules used in this model:

- Geom1 (2D)
  - In-Plane Electric Currents (AC/DC Module)
- Geom2 (3D)

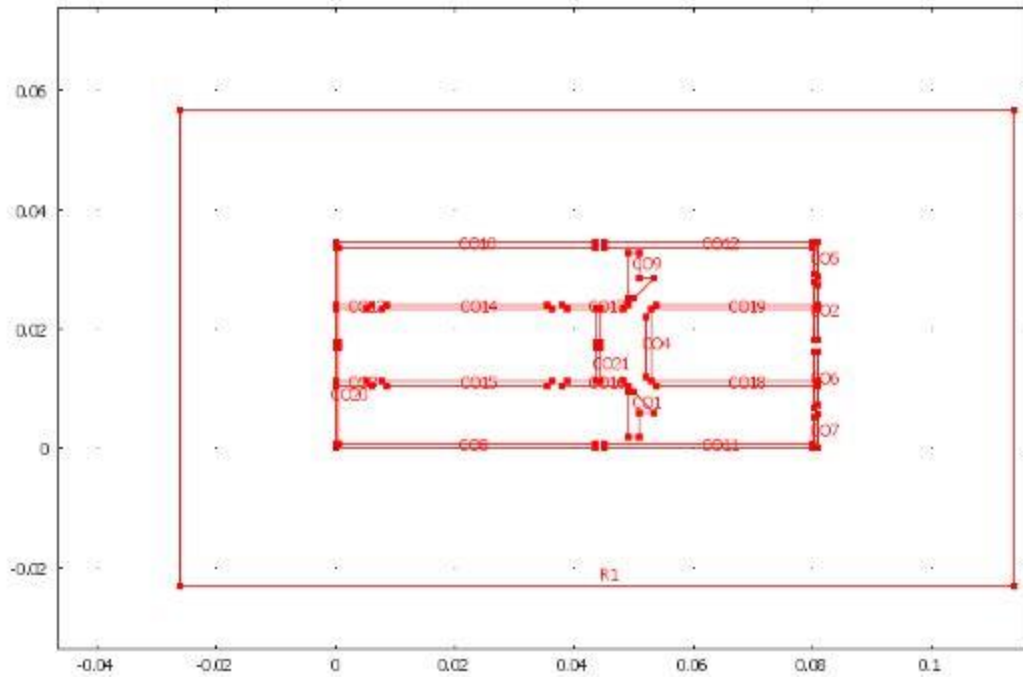
### 3. Constants

Name	Expression	Value	Description
E	1000		Energy eV
C	-480		Collector Volts
A	-760		Analyzer Volts
F	-560		Focus ring Volts
Vtot	$-(2 \cdot E_j / 9.1095e-31)^{.5}$		Velocity m/s
Ej	$E \cdot 1.60217653e-19$		Energy J
eVx	$V_{tot} \cdot \cos(R)$		Velocity X
eVy	$V_{tot} \cdot \sin(R)$		Velocity Y
R	$T \cdot 2 \cdot \pi / 360$		Radians
T	34		Theta Degrees

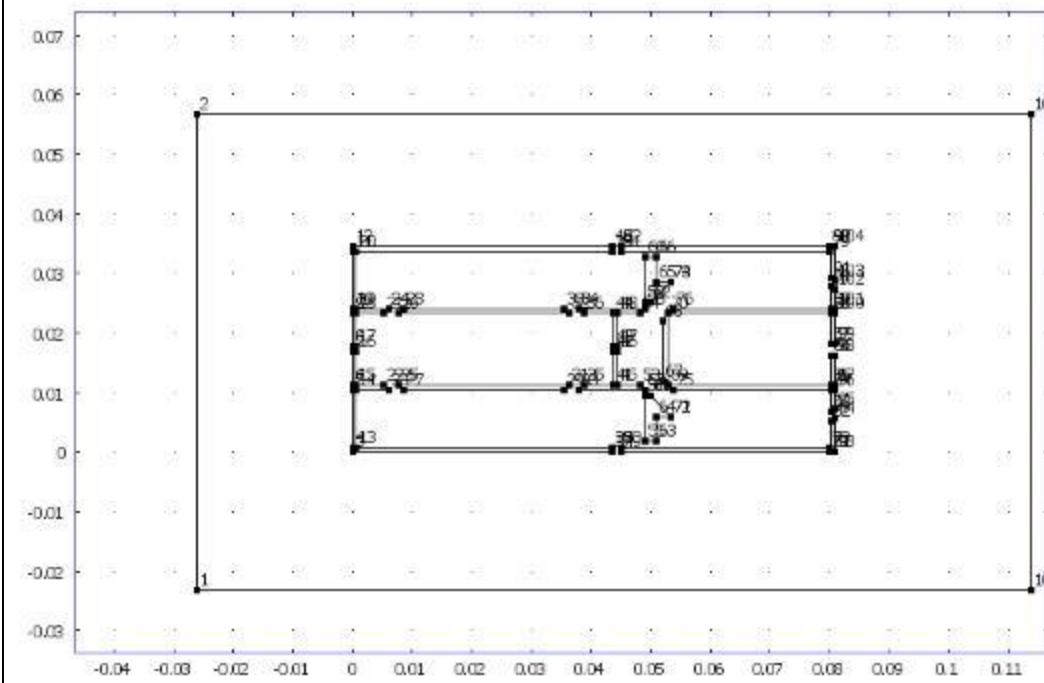
### 4. Geometry

Number of geometries: 2

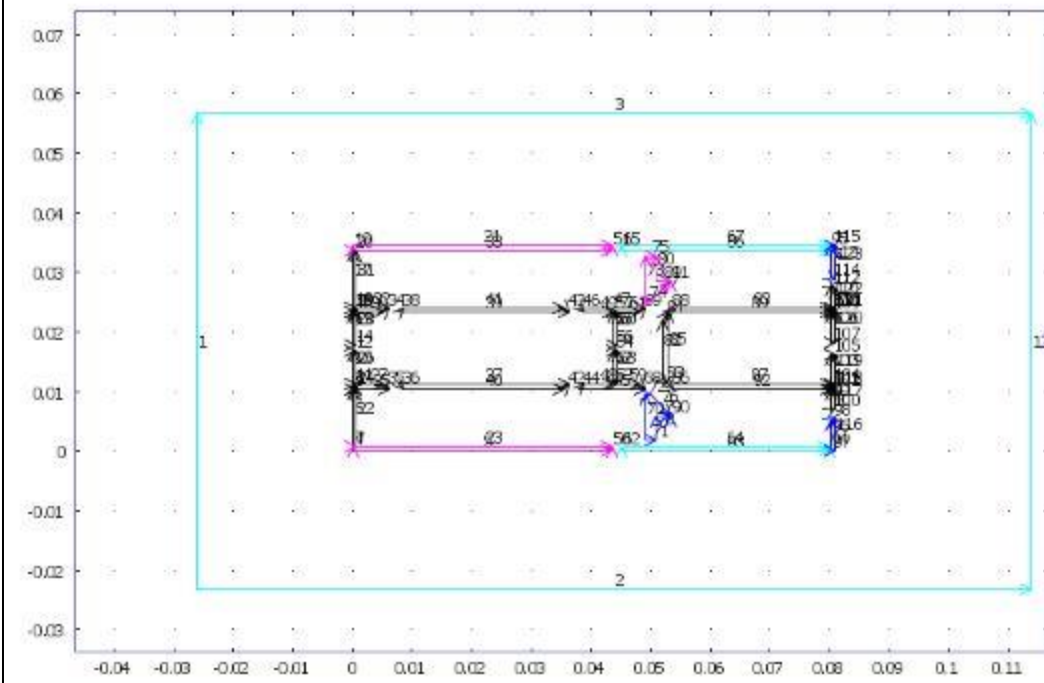
#### 4.1. Geom1



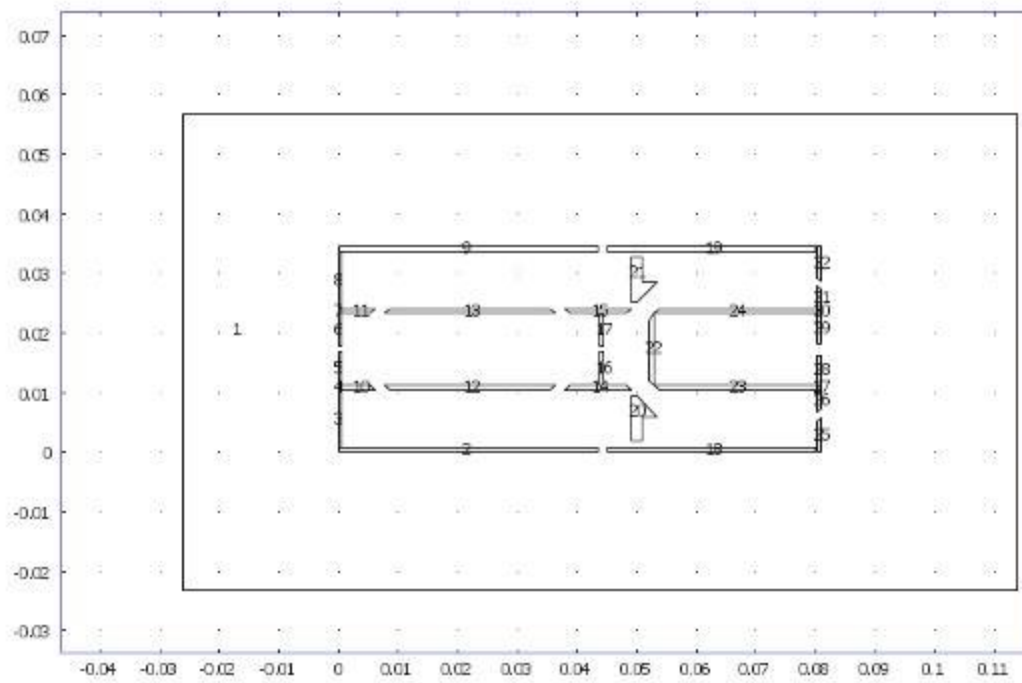
#### 4.1.1. Point mode



#### 4.1.2. Boundary mode



### 4.1.3. Subdomain mode



### 4.2. Geom2

#### 5. Geom1

Space dimensions: 2D

Independent variables: x, y, z

#### 5.1. Mesh

##### 5.1.1. Mesh Statistics

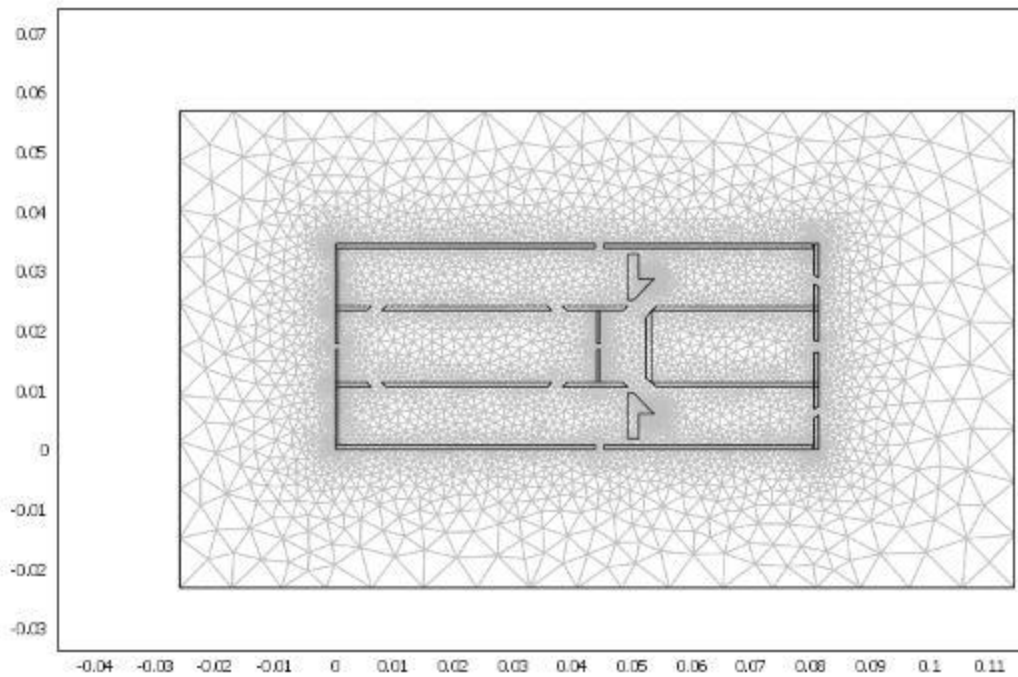
Number of degrees of freedom	23205
Number of mesh points	5815
Number of elements	11575
Triangular	11575
Quadrilateral	0
Number of boundary elements	1005
Number of vertex elements	106
Minimum element quality	0.651
Element area ratio	0



## 5.1. Mesh

### 5.1.1. Mesh Statistics

Number of degrees of freedom	23205
Number of mesh points	5815
Number of elements	11575
Triangular	11575
Quadrilateral	0
Number of boundary elements	1005
Number of vertex elements	106
Minimum element quality	0.651
Element area ratio	0



## 5.2. Application Mode: In-Plane Electric Currents (emqvw)

Application mode type: In-Plane Electric Currents (AC/DC Module)

Application mode name: emqvw

### 5.2.1. Scalar Variables

Name	Variable	Value	Description
epsilon0	epsilon0_emqvw	8.854187817e-12	Permittivity of vacuum
mu0	mu0_emqvw	4*pi*1e-7	Permeability of vacuum
nu	nu_emqvw	50	Frequency

## 5.2. Application Mode: In-Plane Electric Currents (emqvw)

Application mode type: In-Plane Electric Currents (AC/DC Module)

Application mode name: emqvw

### 5.2.1. Scalar Variables

Name	Variable	Value	Description
epsilon0	epsilon0_emqvw	8.854187817e-12	Permittivity of vacuum
mu0	mu0_emqvw	4*pi*1e-7	Permeability of vacuum
nu	nu_emqvw	50	Frequency

### 5.2.2. Application Mode Properties

Property	Value
Default element type	Lagrange - Quadratic
Analysis type	Time-harmonic, electric currents
Potentials	Electric and magnetic
Gauge fixing	Automatic
Input property	Forced voltage
Frame	Frame (ref)
Weak constraints	Off
Vector element constraint	Off

### 5.2.3. Variables

Dependent variables: V, Ax, Ay, psi

Shape functions: shlag(2,V)

Interior boundaries active

### 5.2.4. Boundary Settings

Boundary	1-3, 124, 4, 19
Electric potential (V0)	V0 <b>A</b>
etype	1 <b>nJ0 cont</b>
magtype	A0 A0

Boundary	5, 7, 20-21, 23, 33, 50-51	6, 10, 12-14, 17, 22, 24, 26, 28-29, 31, 52, 54-56, 58, 60, 82-85	8-9, 11, 15-16, 18, 25, 27, 30, 32, 34-49, 53, 57, 59, 61, 68-69, 86-89, 92-93, 102, 104-105, 107, 109, 111, 118, 121
Electric potential (V0)	<b>A</b>	0	0
etype	<b>V</b>	<b>cont</b>	V0
magtype	A0	<b>cont</b>	A0

Boundary	62-67, 94-95	70-72, 76, 78-79, 90	96-98, 113-116, 123
Electric potential (V0)	<b>C</b>	<b>F</b>	0
etype	<b>V</b>	<b>V</b>	<b>fp</b>
magtype	A0	A0	<b>cont</b>

Boundary	99-101, 103, 106, 108, 110, 112, 117, 119-120, 122	73-75, 77, 80-81, 91
Electric potential (V0)	0	<b>F</b>
etype	V0	<b>V</b>
magtype	<b>cont</b>	<b>cont</b>

### 5.2.5. Subdomain Settings

Subdomain	1-3, 5-6, 8-9, 16-22, 25-26, 28-29, 31-32	4, 7, 10-15, 23-24, 27, 30
Relative permeability (mur)	1	1 (Beryllium copper UNS C17200)
Electrical conductivity (sigma) S/m	0	1.163e7[S/m] (Beryllium copper UNS C17200)
Relative permittivity (epsilon_r)	1	1 (Beryllium copper UNS C17200)

### 6. Geom2

Space dimensions: 3D

Independent variables: x, y, z

### 7. Materials/Coefficients Library

#### 7.1. Beryllium copper UNS C17200

Parameter	Value
Heat capacity (C)	420[J/(kg*K)]
Young's modulus (E)	128e9[Pa]
Thermal expansion coeff. (alpha)	16.7e-6[1/K]
Relative permittivity (epsilon_r)	1
Thermal conductivity (k)	118[W/(m*K)]
Relative permeability (mur)	1
Poisson's ratio (nu)	0.3
Density (rho)	8250[kg/m^3]
Electrical conductivity (sigma)	1.163e7[S/m]

#### 7.2. Air, 1 atm

Parameter	Value
Heat capacity (C)	Cp(T[1.K])[J/(kg*K)]
Speed of sound (cs)	cs(T[1.K])[m/s]
Dynamic viscosity (eta)	eta(T[1.K])[Pa*s]
Thermal conductivity (k)	k(T[1.K])[W/(m*K)]
Kinematic viscosity (nu0)	nu0(T[1.K])[m^2/s]
Density (rho)	rho(p[1.Pa],T[1.K])[kg/m^3]

#### 7.2.1. Functions

Function	Expression	Derivatives	Complex output
cs(T)	$\sqrt{1.4 \cdot 287 \cdot T}$	$\text{diff}(\sqrt{1.4 \cdot 287 \cdot T}, T)$	false
nu0(T)	$(-7.887E-12 \cdot T^2 + 4.427E-08 \cdot T + 5.204E-06) / (1.013e5 \cdot 28.8e-3 / 8.314 / T)$	$\text{diff}((-7.887E-12 \cdot T^2 + 4.427E-08 \cdot T + 5.204E-06) / (1.013e5 \cdot 28.8e-3 / 8.314 / T), T)$	false
Cp(T)	$0.0769 \cdot T + 1076.9$	$\text{diff}(0.0769 \cdot T + 1076.9, T)$	false
rho(p,T)	$p \cdot 28.8e-3 / 8.314 / T$	$\text{diff}(p \cdot 28.8e-3 / 8.314 / T, p), \text{diff}(p \cdot 28.8e-3 / 8.314 / T, T)$	false
eta(T)	$-7.887E-12 \cdot T^2 + 4.427E-08 \cdot T + 5.204E-06$	$\text{diff}(-7.887E-12 \cdot T^2 + 4.427E-08 \cdot T + 5.204E-06, T)$	false
k(T)	$10 \cdot (0.8616 \cdot \log_{10}(\text{abs}(T)) - 3.7142)$	$\text{diff}(10 \cdot (0.8616 \cdot \log_{10}(\text{abs}(T)) - 3.7142), T)$	false

### 7.3. Graphite felt

Parameter	Value
Heat capacity (C)	200[J/(kg*K)]
Surface emissivity (epsilon)	1
Relative permittivity (epsilon <sub>r</sub> )	1
Thermal conductivity (k)	0.3[W/(m*K)]
Relative permeability (mu <sub>r</sub> )	1
Density (rho)	120[kg/m <sup>3</sup> ]
Electrical conductivity (sigma)	100[S/m]

### 7.4. Graphite felt

Parameter	Value
Heat capacity (C)	200[J/(kg*K)]
Surface emissivity (epsilon)	1
Relative permittivity (epsilon <sub>r</sub> )	1
Thermal conductivity (k)	0.3[W/(m*K)]
Relative permeability (mu <sub>r</sub> )	1
Density (rho)	120[kg/m <sup>3</sup> ]
Electrical conductivity (sigma)	100[S/m]

## 8. Solver Settings

Solve using a script: off

Analysis type	Time-harmonic_electric_currents
Auto select solver	On
Solver	Stationary
Solution form	Automatic
Symmetric	auto
Adaption	Off

### 8.1. Direct (UMFPACK)

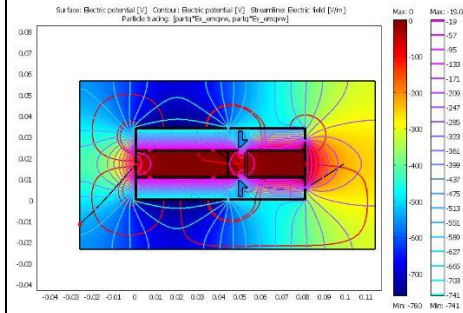
Solver type: Linear system solver

Parameter	Value
Pivot threshold	0.1
Memory allocation factor	0.7

### 8.2. Advanced

Parameter	Value
Constraint handling method	Elimination
Null-space function	Automatic
Assembly block size	5000
Use Hermitian transpose of constraint matrix and in symmetry detection	Off
Use complex functions with real input	Off
Stop if error due to undefined operation	On
Type of scaling	Automatic
Manual scaling	
Row equilibration	On
Manual control of reassembly	Off
Load constant	On
Constraint constant	On
Mass constant	On
Damping (mass) constant	On
Jacobian constant	On
Constraint Jacobian constant	On

## 9. Postprocessing



## 10. Variables

### 10.1. Boundary

Name	Description	Expression
dVobnd_emqvw	Volume integration contribution	d_emqvw
nJ_emqvw	Current density outflow	nx_emqvw * Jx_emqvw + ny_emqvw * Jy_emqvw
intExav_emqvw	Electric Maxwell surface stress tensor, time average, x component	real(-0.25 * (Ex_emqvw_up * conj(Dx_emqvw_up) + Ey_emqvw_up * conj(Dy_emqvw_up)) * dnx + 0.5 * (dnx * Ex_emqvw_up + dny * Ey_emqvw_up) * conj(Dx_emqvw_up))
intExav_emqvw	Electric Maxwell surface stress tensor, time average, x component	real(-0.25 * (Ex_emqvw_down * conj(Dx_emqvw_down) + Ey_emqvw_down * conj(Dy_emqvw_down)) * unx + 0.5 * (unx * Ex_emqvw_down + uny * Ey_emqvw_down) * conj(Dx_emqvw_down))
intEyav_emqvw	Electric Maxwell surface stress tensor, time average, y component	real(-0.25 * (Ex_emqvw_up * conj(Dx_emqvw_up) + Ey_emqvw_up * conj(Dy_emqvw_up)) * dny + 0.5 * (dnx * Ex_emqvw_up + dny * Ey_emqvw_up) * conj(Dy_emqvw_up))
intEyav_emqvw	Electric Maxwell surface stress tensor, time average, y component	real(-0.25 * (Ex_emqvw_down * conj(Dx_emqvw_down) + Ey_emqvw_down * conj(Dy_emqvw_down)) * uny + 0.5 * (unx * Ex_emqvw_down + uny * Ey_emqvw_down) * conj(Dy_emqvw_down))
nJs_emqvw	Source current density	unx * (Jx_emqvw_down - Jx_emqvw_up) + uny * (Jy_emqvw_down - Jy_emqvw_up)
tEx_emqvw	Tangential electric field, x component	-VtX
tDx_emqvw	Tangential electric displacement, x component	epsilon0_emqvw * epsilon0r_bnd_emqvw * tEx_emqvw
tEy_emqvw	Tangential electric field, y component	-VtY
tDy_emqvw	Tangential electric displacement, y component	epsilon0_emqvw * epsilon0r_bnd_emqvw * tEy_emqvw
normE_emqvw	Tangential electric field, norm	sqrt(abs(tEx_emqvw)^2 + abs(tEy_emqvw)^2)
normD_emqvw	Tangential electric displacement, norm	sqrt(abs(tDx_emqvw)^2 + abs(tDy_emqvw)^2)

## 10.2. Subdomain

### 10.2.1. Subdomain 1-3, 5-6, 8-9, 16-22, 25-26, 28-29, 31-32

Name	Description	Expression
dr_guess_emqvw	Width in radial direction default guess	0
RO_guess_emqvw	Inner radius default guess	0
SR_emqvw	Infinite element radial coordinate	x
SX_emqvw	Infinite element x coordinate	x
Sdx_guess_emqvw	Inner x coordinate default guess	0
Sdx_guess_emqvw	Width in x direction default guess	0
rCylx_emqvw	Infinite element r cylindrical vector, x component	0
srcptnx_guess_emqvw	Source point default guess, x component	0
Sy_emqvw	Infinite element y coordinate	y
Sdy_guess_emqvw	Inner y coordinate default guess	0
Sdy_guess_emqvw	Width in y direction default guess	0
rCylx_emqvw	Infinite element r cylindrical vector, y component	0
srcpty_guess_emqvw	Source point default guess, y component	0
detJ_emqvw	Infinite element transformation matrix determinant	1
Jxx_emqvw	Infinite element transformation matrix determinant, element xx	1
invJxx_emqvw	Infinite element inverse transformation matrix, element xx	1
Jxy_emqvw	Infinite element transformation matrix determinant, element xy	0
invJxy_emqvw	Infinite element inverse transformation matrix, element xy	0
Jyx_emqvw	Infinite element transformation matrix determinant, element yx	0
invJyx_emqvw	Infinite element inverse transformation matrix, element yx	0
Jyy_emqvw	Infinite element transformation matrix determinant, element yy	1
invJyy_emqvw	Infinite element inverse transformation matrix, element yy	1
delta_emqvw	Slit depth	1 / (omega_emqvw * sqrt(0.5 * mu0_emqvw * mur_emqvw * epsilon0_emqvw * epsilon0r_emqvw * (1 + sqrt(1 + (sigma_emqvw / (omega_emqvw * epsilon0r_emqvw * epsilon0r_emqvw))^2))))
dVd_emqvw	Volume integration contribution	detJ_emqvw * d_emqvw
Dx_emqvw	Electric displacement, x component	epsilon0r_emqvw * Ex_emqvw + epsilon0ny_emqvw * Ey_emqvw
Dy_emqvw	Electric displacement, y component	epsilon0ny_emqvw * Ex_emqvw + epsilon0rx_emqvw * Ey_emqvw
epsilon_emqvw	Permittivity	epsilon0_emqvw * epsilon0r_emqvw
epsilon0xx_emqvw	Permittivity, xx component	epsilon0_emqvw * epsilon0rxx_emqvw
epsilon0xy_emqvw	Permittivity, xy component	epsilon0_emqvw * epsilon0rxy_emqvw
epsilon0yx_emqvw	Permittivity, yx component	epsilon0_emqvw * epsilon0ryx_emqvw
epsilon0yy_emqvw	Permittivity, yy component	epsilon0_emqvw * epsilon0ryy_emqvw
Ex_emqvw	Electric field, x component	-Vx
Jdx_emqvw	Displacement current density, x component	j * omega_emqvw * Dx_emqvw
Jpx_emqvw	Potential current density, x component	0
Jx_emqvw	Total current density, x component	Jex_emqvw + Jdx_emqvw + Jpx_emqvw
Ey_emqvw	Electric field, y component	-Vy
Jdy_emqvw	Displacement current density, y component	j * omega_emqvw * Dy_emqvw
Jpy_emqvw	Potential current density, y component	0
Jy_emqvw	Total current density, y component	Jey_emqvw + Jdy_emqvw + Jpy_emqvw
normP_emqvw	Electric polarization, norm	sqrt(abs(Dx_emqvw)^2 + abs(Dy_emqvw)^2)
normDr_emqvw	Remanent displacement, norm	sqrt(abs(Drx_emqvw)^2 + abs(Dry_emqvw)^2)
normD_emqvw	Electric displacement, norm	sqrt(abs(Dx_emqvw)^2 + abs(Dy_emqvw)^2)
normE_emqvw	Electric field, norm	sqrt(abs(Ex_emqvw)^2 + abs(Ey_emqvw)^2)
normJp_emqvw	Potential current density, norm	sqrt(abs(Jpx_emqvw)^2 + abs(Jpy_emqvw)^2)
normJd_emqvw	Displacement current density, norm	sqrt(abs(Jdx_emqvw)^2 + abs(Jdy_emqvw)^2)
normJe_emqvw	External current density, norm	sqrt(abs(Jex_emqvw)^2 + abs(Jey_emqvw)^2)
normJ_emqvw	Total current density, norm	sqrt(abs(Jx_emqvw)^2 + abs(Jy_emqvw)^2)
Wseav_emqvw	Electric energy density, time average	0.25 * real(Dx_emqvw * conj(Ex_emqvw) + Dy_emqvw * conj(Ey_emqvw))
Wtav_emqvw	Total energy density, time average	Wseav_emqvw
Qav_emqvw	Resistive heating, time average	0.5 * real(Jx_emqvw * conj(Ex_emqvw) + Jy_emqvw * conj(Ey_emqvw))

10.2.2. Subdomain 4, 7, 10-15, 23-24, 27, 30

Name	Description	Expression
dr_guess_emqvw	Width in radial direction default guess	0
R0_guess_emqvw	Inner radius default guess	0
SR_emqvw	Infinite element radial coordinate	
Sx_emqvw	Infinite element x coordinate	x
S0x_guess_emqvw	Inner x coordinate default guess	0
Sdx_guess_emqvw	Width in x direction default guess	0
rCylc_emqvw	Infinite element r cylindrical vector, z component	
srcprntx_guess_emqvw	Source point default guess, x component	0
Sy_emqvw	Infinite element y coordinate	y
S0y_guess_emqvw	Inner y coordinate default guess	0
Sdy_guess_emqvw	Width in y direction default guess	0
rCylc_emqvw	Infinite element r cylindrical vector, y component	
srcprntz_guess_emqvw	Source point default guess, z component	0
detJ_emqvw	Infinite element transformation matrix determinant	1
Jxx_emqvw	Infinite element transformation matrix determinant, element xx	1
InvJxx_emqvw	Infinite element inverse transformation matrix, element xx	1
Jxy_emqvw	Infinite element transformation matrix determinant, element xy	0
InvJxy_emqvw	Infinite element inverse transformation matrix, element xy	0
Jyx_emqvw	Infinite element transformation matrix determinant, element yx	0
InvJyx_emqvw	Infinite element inverse transformation matrix, element yx	0
Jyy_emqvw	Infinite element transformation matrix determinant, element yy	1
InvJyy_emqvw	Infinite element inverse transformation matrix, element yy	1
delta_emqvw	Skin depth	$1/(\omega \epsilon_0 \mu_0 \epsilon_{emqvw} \sqrt{0.5 * \mu_0 \epsilon_{emqvw} * \mu_r \epsilon_{emqvw} * \epsilon_{emqvw} * \epsilon_{emqvw} * \epsilon_{emqvw} * \epsilon_{emqvw} * (1 + \sqrt{1 + (\sigma_{emqvw} / (\omega \epsilon_{emqvw} * \epsilon_{emqvw} * \epsilon_{emqvw} * \epsilon_{emqvw}))^2})})$
dVol_emqvw	Volume integration contribution	detJ_emqvw * d_emqvw
Dx_emqvw	Electric displacement, x component	$\epsilon_{emqvw} * E_x + \epsilon_{emqvw} * \epsilon_{emqvw} * E_y$
Dy_emqvw	Electric displacement, y component	$\epsilon_{emqvw} * E_y + \epsilon_{emqvw} * E_x$
epsilon_emqvw	Permittivity	$\epsilon_{emqvw} * \epsilon_{emqvw}$
epsilon0x_emqvw	Permittivity, xx component	$\epsilon_{emqvw} * \epsilon_{emqvw}$
epsilon0y_emqvw	Permittivity, yy component	$\epsilon_{emqvw} * \epsilon_{emqvw}$
epsilon0z_emqvw	Permittivity, zz component	$\epsilon_{emqvw} * \epsilon_{emqvw}$
epsilon0xy_emqvw	Permittivity, xy component	$\epsilon_{emqvw} * \epsilon_{emqvw}$
epsilon0yx_emqvw	Permittivity, yx component	$\epsilon_{emqvw} * \epsilon_{emqvw}$
Ex_emqvw	Electric field, x component	-Vx
Jdx_emqvw	Displacement current density, x component	$j * \omega \epsilon_{emqvw} * D_x$
Jpx_emqvw	Potential current density, x component	$-\sigma_{emqvw} * V_x$
Jx_emqvw	Total current density, x component	$J_x + J_{dx}$
Ey_emqvw	Electric field, y component	-Vy
Jdy_emqvw	Displacement current density, y component	$j * \omega \epsilon_{emqvw} * D_y$
Jpy_emqvw	Potential current density, y component	$-\sigma_{emqvw} * V_y$
Jy_emqvw	Total current density, y component	$J_y + J_{dy}$
normP_emqvw	Electric polarization, norm	$\sqrt{abs(P_x)^2 + abs(P_y)^2}$
normD_emqvw	Electric displacement, norm	$\sqrt{abs(D_x)^2 + abs(D_y)^2}$
normE_emqvw	Electric field, norm	$\sqrt{abs(E_x)^2 + abs(E_y)^2}$
normJp_emqvw	Potential current density, norm	$\sqrt{abs(J_{px})^2 + abs(J_{py})^2}$
normJd_emqvw	Displacement current density, norm	$\sqrt{abs(J_{dx})^2 + abs(J_{dy})^2}$
normJ_emqvw	Total current density, norm	$\sqrt{abs(J_x)^2 + abs(J_y)^2}$
normI_emqvw	Electric energy density, time average	$0.25 * real(D_x * E_x + D_y * E_y)$
Wav_emqvw	Total energy density, time average	$W_{av}$
Qav_emqvw	Resistive heating, time average	$0.5 * real(J_x * E_x + J_y * E_y)$

## ABOUT THE AUTHOR

Jay A. Bieber earned his B.S. in Physics from the University of North Dakota, Grand Forks, N.D. in 1993 with a Senior Project titled: “Homebuilt Nitrogen Laser Pumped Organic Dye Laser.” He earned his M.S. in Engineering Science from the University of South Florida in Tampa, FL in 2004 with a Thesis titled: “Synthesis of Nanoscale Structures in Single Crystal Silicon Carbide by Electron Beam Lithography”. Jay is currently a Research Engineer with the Nanotechnology Research and Education Center, (NREC), in the College of Engineering at the University of South Florida. He manages the materials characterization and instructional services for faculty, students, and industrial NREC users. Jay has over twenty seven years of experience in the use of Scanning Electron Microscopy, (SEM-EDS), physical vapor deposition, (PVD), Scanning Auger Microscopy, (SAM), X-ray Photoelectron Spectroscopy, (XPS), UHV vacuum technology and vacuum system maintenance. In addition to his professional duties, he enjoys mentoring and teaching students basic mathematics and physics principles, techniques in research methods, and fabrication & metrology of thin films and nanostructures. Jay also teaches a graduate course in Materials Characterization in the Materials Science Graduate program at USF.